

Bulgarian Academy of Sciences

Bulgarian
Geophysical
Journal

2014 Volume 40

BGJ

Bulgarian Geophysical Journal (BGJ) is an interdisciplinary journal containing original contributions on physics of the atmosphere and ionosphere, geomagnetism and gravimetry, seismology and physics of the Earth's interior, as well as those dealing with applied geophysics, instrumentation and observations in these scientific fields. BGJ is a joint publication of National Institute of Geophysics, Geodesy and Geography at the Bulgarian Academy of Sciences and the Bulgarian Geophysical Society. BGJ is now published in 1 issue per year.

Editor-in-Chief - Prof. Kostadin Ganev

Editors

Acad. L. Christoskov -	Seismology
Acad. G. Miloshev -	Atmospheric Physics
Corr.member D. Solakov -	Seismology
Prof. D.Jordanova -	Earth Magnetism

Address of the Editorial Board:

Bulgarian Geophysical Journal, NIGGG - BAS,

Acad. G. Bonchev Street, bl.3, Sofia 1113, Bulgaria

e-mail: bgj@geophys.bas.bg

Technical Editor: M. Palapeshkova, tel. /02/ 979 3330

© National Institute of Geophysics, Geodesy and Geography

2014

Bulgarian Academy of Sciences

© Printed in: "M.Drinov" Academic Publishing House, Sofia, Bulgaria

Bulgarian Geophysical Journal

2014, Vol. 40

Contents

V. Ivanov, S. Evtimov – Heat risks in Bulgaria during 2003-2012 period	3
H. Chervenkov – Simple postprocessing method for vertical correction based on stratified near-surface atmospheric parameters	14
A. Stoycheva, S. Evtimov – Studying the fogs in Sofia with Cherni vrah-Sofia stability index	23
A. Deleva – LIDAR registration of the vertical stratification of Saharan dust incursions over Sofia	33
D. Yu. Abramova, S.V. Filippov, L. M. Abramova, Iv. M. Varentsov – Lithospheric magnetic anomalies in the Balkan region	50
L. Abramova, Iv. Varensov, D. Abramova – The relationship between the electromagnetic parameters and tectonic structure of the territory of Bulgaria	65
M. Metodiev – Modelling of declination's secular variation for the purposes of regional topographic mapping	76
H. Chervenkov, I. Tsonevsky, K. Slavov – Possibility for drought assessment with gridded data-sets of the standardized precipitation index	85

***E.Botev, V.Protopopova, I.Aleksandrova, B.Babachkova, S.Velichkova,
I.Popova, P.Raykova, M.Popova*** – Data and analysis of the events
recorded by NOTSSI in 2014

98

HEAT RISKS IN BULGARIA DURING 2003-2012 PERIOD

V. Ivanov¹, S. Evtimov²

¹ National Institute Of Geophysics, Geodesy and Geography, ul.Acad.G.Bonchev, bl.3, Sofia 1113, Bulgaria, e-mail: vivanov@geophys.bas.bg

² Sofia Univecity “St. Climent Ohridski”, Faculty of Physics, Department of Meteorology and Geophysics, 1164 Sofia, Bulgaria, e^vtimov@phys.uni-sofia.bg

Abstract: A sample of twenty seven weather stations is used to estimate the heat stress risks in Bulgaria during the period 2003-2012. The values of Steadman’s heat index at primary or intermediate standard hours are used for this purpose. The range of the index is recoded into five levels of risk and the observations are cross-classified on stations and risk categories. Three frequency tables are produced and analyzed. The table for non-mountain stations and warm period May-October is biplotted and stations are clustered according to risks. Geographical distribution of the heat stress risks is established. The heat waves during the period under consideration are discussed.

Key words: biometeorology, Bulgaria, heat index, heat waves, correspondence analysis biplot

Introduction

A living body constantly produces heat. If the heat excess is not shed to the environment, the conditions for physiological heat stress arise. The heat stress is the disturbance of the human thermoregulatory system, which can cause a number of heat-related illnesses: heat fatigue, heat syncope, heat exhaustion and heat stroke (Starr and Mcmillan, 2008). A high level of the heat stress poses a health risk to anyone engaged in outdoor activity over a short period of time. A significant weather hazard to public health is the so-called heat waves. They are the prolonged episodes of excessive heat stress that occur in synoptic situations with pronounced slow development and movement of the hot air mass. There is ample evidence that the heat waves are associated either directly or indirectly with increases in morbidity and mortality (Robine et al., 2008).

At hot weather, the human body cools off through perspiration because heat loss by radiation and convection ceases and in practice only sweat evaporation takes away the

heat from the body. Slowing down the rate of the evaporation, a high humidity retards the loss of the surplus heat. This is why humid days feel hotter than the actual temperature. Steadman (1979) quantifies the combined effect of high temperature and humidity on the human body by the values of the apparent temperature commonly referred to as the heat index (HI). More precisely, the HI is ambient temperature adjusted for variations in vapor pressure above or below some base value (Steadman, 1979). Since 1984 United States National Weather Service of the National Oceanic and Atmospheric Administration (NWS) has routinely employed the HI in order to alert the public and relevant authorities to the hazards of heat waves (NWS, 1994).

The objective of this paper is an evaluation of the heat stress hazard in Bulgaria during the period 2003-2012. The reports of 27 weather stations are used to compute the daily summaries of extremes of the *HI* for each station. After NWS we categorize the *HI* in levels of risk, cross-classify the observations on the risk categories and the stations and build respective frequency tables. The stations index the rows of the tables and the categories of risk the columns. An entry of the table is the number of observations that share a station and a risk level. We use these tables to reveal the correspondences and structural relationships between different stations and categories of risk. The statistical method of correspondence analysis biplot (Gabriel and Odoroff, 1990; Greenacre, 1993) is applied for this purpose. Providing a joint display of the stations and risk categories as points on the plane, this technique visualizes the major features of the underlying correspondences between the stations and risks.

Section 2 gives general information for *HI* and heat waves. Section 3 presents the data and their preprocessing and preliminary analysis. In Sec. 4 we biplot the frequency table for station and risk categories and reveal the inherent statistical correspondences between stations and risks during warm period May-October as well as the geographical distributions of the heat hazard. The heat waves during the period under consideration are discussed in Sec. 5. Section 6 summarizes the results.

Heat Index and heat waves.

Heat Index is an index that combines the thermal and humidity effects on the body and represents them in one value. The index is developed by R. G. Steadman (1979) who terms it apparent temperature. Steadman uses the achievements of human physiology and clothing science and models the human sensation of the heat by a complex collection of equations. To simplify the computations he fixes a number of parameters to their typical values. Here we quote only some base atmospheric and human parameters. The model accepts an atmospheric vapor pressure of 1600 Pa, a barometric pressure of 1013 hPa, a wind speed of 2.5 m s^{-1} and a zero extra radiation. The base human parameters are as follows: height - 1.7 m, weight - 67 kg, clothing cover - long trousers and short-sleeved shirt or blouse at 84% coverage and activity - a person walking outdoors at a speed of 1.4 m s^{-1} (180 W m^{-2}).

Steadman summarizes his results as a table that gives the *HI* as discrete function on the air temperature and the humidity. For operational purposes Rothfus (1990), approximates Steadman's table by 9-term and later NWS (<http://i4weather.net/hiwc.html>)

by 16-term polynomial multiple regression equations. Schoen (2005) offers an exponential fit which more closely approximates the Steadman's table and has only 3 fitting parameters. The corresponding computational formula is:

$$HI = t - 1.0799 e^{0.03755 t} [1 - e^{0.0801(t_d - 14)}], \quad (1)$$

where HI is the heat index, t is ambient dry bulb temperature, t_d is dew point temperature, all in degree Celsius. Note that the values of HI are computed for shady and light wind conditions. Exposure to full sunshine can increase HI by up to 8.4 °C. A strong hot and dry wind is extremely hazardous since it adds the extra heat to the body. Old people and children are more vulnerable to high HI .

The World Meteorological Organization has not yet defined the term heat wave (Koppe et al., 2004). Generally, a heat wave is a period of excessive heat and high humidity relative to location and time of year. In Europe, the definitions of heat wave are operational and they are based on absolute or relative thresholds for air temperature, air temperature and minimum duration, or indices that are combination of both air temperature and humidity (Koppe et al., 2004). Robinson (2001) adopts that there is a heat wave if the conditions of the NWS for excessive heat alert present for a minimum duration. The NWS issues excessive heat alert when the daytime HI reaches 40.6 °C and the nighttime HI stays above 26.7 °C for two consecutive days (NWS, 1994)). This base definition is for entire United States but regionally the thresholds and the duration can vary considerably.

Data, preprocessing and preliminary analysis

We analyze the heat stress risks at 27 meteorological stations in Bulgaria for the period 2003/01/01-2012/12/31. Figure 1 displays the spatial distribution of the stations. The transliteration of station names is after recommendation of the Council of Science of the Institute at the Bulgarian Academy of Science. The five stations Botev Vrah (2376 m), Cherni Vrah (2290 m), Murgash (1687 m), Musala (2925 m) and Rozhen (1723 m), henceforth called "mountain", are at the peaks. The numbers in the parentheses are the elevations above sea level. In determining a HI , the simultaneous air temperature and humidity are required. We extract the station records for air temperature and dew point temperature from respective station reports. These reports are downloaded from database of the National Climatic Data Center of United States of America (<http://cdo.ncdc.noaa.gov/CDO/cdo>). The observations are at primary or intermediate standard hours 00:00, 03:00, 06:00, 09:00, 12:00, 15:00, 18:00, and 21:00 Greenwich Mean Time.

The raw data have undergone automated quality control and erroneous or suspect values are flagged. The original data coverage is at least 96% with exception of station Rozhen where coverage falls to 90%. As a rule the gaps in the records are short and disconnected. We fill in the gaps or replace the incorrect data by the linear interpolations of adjacent correct values in respective records.

We compute the values of HI by means of the exponential fit (1). To obtain serially complete records, air temperature alone is used when the air temperature is below

23.9°C, when *HI* is undefined. Next we extract the daily summaries of maximum *HI*, minimum *HI* and respective air and dew point temperatures. The result is the 27 multivariate series of length 3653 days.

The *HI* is a continuous variable but after NWS we recode it into 5 distinct ranges. Each range corresponds to a level of the physiological risk of heat stress. The categories of heat hazard are: “Caution”, “Extreme caution”, “Danger” and “Extreme danger”. The NWS advises Caution when *HI* is 26.7-32.2 °C. In this case, the fatigue is

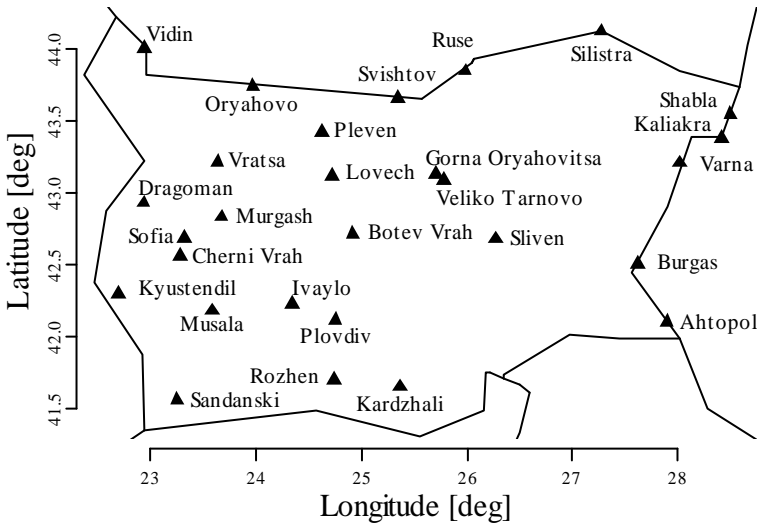


Fig. 1. Locations of the Bulgarian weather stations under consideration.

possible with prolonged exposure and physical activity. The category *Extreme caution* corresponds to an *HI* of 32.2-40.6 °C. Then sunstroke, muscle cramps, and/or heat exhaustion are possible. NWS issues *Danger* warning when *HI* is 40.6-54.4 °C. The sunstroke and the heat exhaustion are likely and the heat stroke is possible in this case. The category is *Extreme danger* when *HI* climbs to 54.4 °C and over. Then heat strokes and the sunstrokes become imminent. We set up also a fifth category “*No stress*” for *HI* below 26.7 °C.

So, we categorize *HI* in 5 levels of hazard. A second categorical variable is the place of the observations. Its 27 levels are the different weather stations. We crosstabulate on these two variables and build 3 frequency tables of size 27×5. The stations index the rows and the categories of heat risk index the columns. A shell contains the number of observations that share a station and a level of hazard. First two tables are for daily maximum *HI* and daily minimum *HI* and all calendar days in the year. Third table is for daytime maximum *HI* but for warm period May-October only.

A survey of our frequency tables leads to following general conclusions. There is not any day of category *Extreme danger* in the data. The mountain stations Musala, Botev Vrah and Cherni Vrah come totally under category *No stress*. As for two other peak

stations, there are only 5 days at Murgash and only 9 days at Rojen when the *HI* reaches the category *Caution*. The total count of stressed nights vary from zero for the most of the stations to 12 for Ahtopol, 14 for Burgas and 37 for Kaliakra, 4.4 nights on average. Finally, in practice there is not heat stress during the cold season November-April. The few stressed days in this period fall all into category *Caution* and their count vary from zero for Varna and Shabla to 6 days for Ruse and 8 days for Gorna Oriahovitsa, 2.3 days on average.

Summing up, the heat hazard is dominant in the daytime during the warm period May-October and at non-mountain stations of our sample. For that reason we focus only on the frequency table for the observations at the non-mountain stations during the warm period May-October.

Biplot

So, we have a frequency table of size 22×4 . The non-mountain stations index the rows and four categories of heat hazard *No stress*, *Caution*, *Extreme caution* and *Danger* index the columns. Our goal is to reveal the structural dissimilarities and similarities between different station profiles. A station profile is defined as the frequencies in corresponding row of the table divided by its row sum. Instead of working directly by the frequency table we visualize it by the statistical technique of the correspondence analysis biplot. The mathematical basis of this method can be found for example in the article of Greenacre (1993). Here we use a variant of the bipoting of Gabriel and Odoroff (1990). In the case the method optimally displays the stations as points and the categories of hazard as arrows on a two-dimension plot such that the scalar product between a point vector and an arrow approximates the corresponding entry of the matrix of deviations from average profile. The average station profile is defined as the vector of column sums divided by the grand total of the table.

Figure 2 displays the correspondence analysis biplot of the frequency table of the non-mountain stations for period May-October. The points correspond to the stations and the arrows to categories of risk. The points of the stations Pleven, Veliko Tarnovo and Silistra are close to the origin of the plot but they are not labeled in order not to clutter the display. The category *Danger* arises very rarely, from zero for Sofia, Gorna Oriahivitsa and Ahtopol to 8 cases for Sandanski and 10 for Ruse, or 3.1 on average. For that reason we merge *Danger* with the *Extreme caution* in a single category *Extreme caution + Danger*. The biopot representation is perfect because the risk categories are only 3.

As mentioned, the projections of a station point onto a category arrow multiplied by the arrow length, i.e. the scalar product between these two vectors equals to corresponding entry of the matrix of deviation from average profile. The average station profile is 57.3%, 30.0% and 12.7% on the categories *No stress*, *Caution* and *Extreme caution + Danger* respectively. We see that nearly half of the days during the period May-October are stressed by heat. Looking at Fig. 2 we see that projections of the stations in the left half-plane are in direction of the arrow *No stress* and oppose in direction the arrows *Caution* and *Extreme caution + Danger*. Thus these stations have positive deviations from average on category *No stress* and negative deviations on *Caution* and *Extreme caution +*

Danger. Conversely, the projections of the station in the right half-plane are in direction of

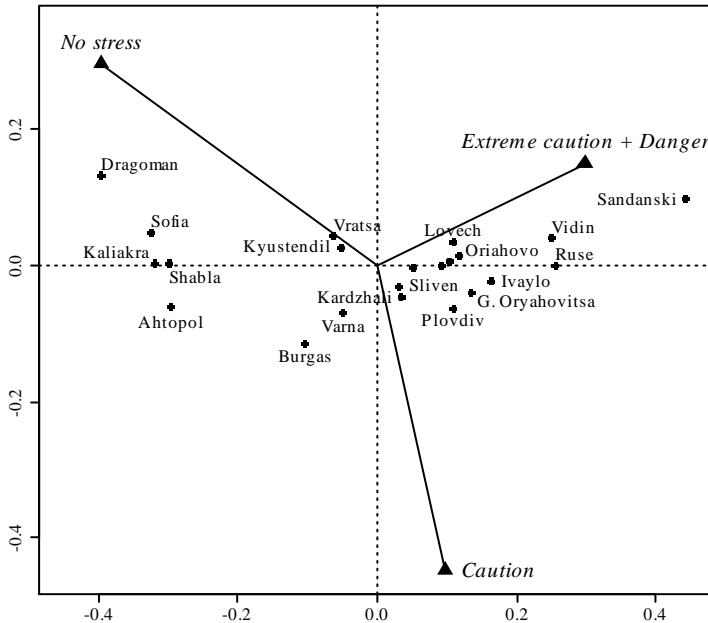


Fig. 2. Correspondence analysis biplot of the non-mountain stations with daytime risk categories during the warm period May-October.

the arrows *Caution* and *Extreme caution + Danger* and oppose in direction the arrow *No stress*. All these stations have negative deviations from average on category *No stress* and positive deviations on *Caution* and *Extreme caution + Danger*. The exceptions of this classification are only Varna with its -0.1%.

Summing up, the biplot clearly splits our sample of stations into two groups. The stations in the left half-plane of the display have positive deviations from average on category *No stress* and negative deviations on *Caution* and *Extreme caution + Danger*. Conversely, the stations in the right half-plane have negative deviations from average on category *No stress* and positive deviations on *Caution* and *Extreme caution + Danger*.

Has our biplot classification some geographical meaning? Figure 3 displays the locations of the stations on the map of Bulgaria together with some of the biplot information. The empty markers represent the stations with higher percentage on category *No stress* and lower percentage on categories *Caution* and *Extreme caution + Danger*. The deviations of these stations from average *No stress* range from 2.9% for Kyustendil to 14.2% for Sofia and 19.6% for Dragoman. We see that lowest hazardous stations are close to west and east borders of Bulgaria. The filled triangles mark stations with higher percentage on categories *Caution* and *Extreme caution + Danger* and lower percentage on category *No stress*. The grey-scale filling of the triangles is according the magnitude of the deviation from the average percentage of category *Extreme caution + Danger*. The darker the filling the larger the deviation. As seen, stations with higher percentages on categories

Caution and Extreme caution + Danger and lower percentage on No stress are at Danube and in central belt between western and eastern Bulgaria. With exception of Sandanski we

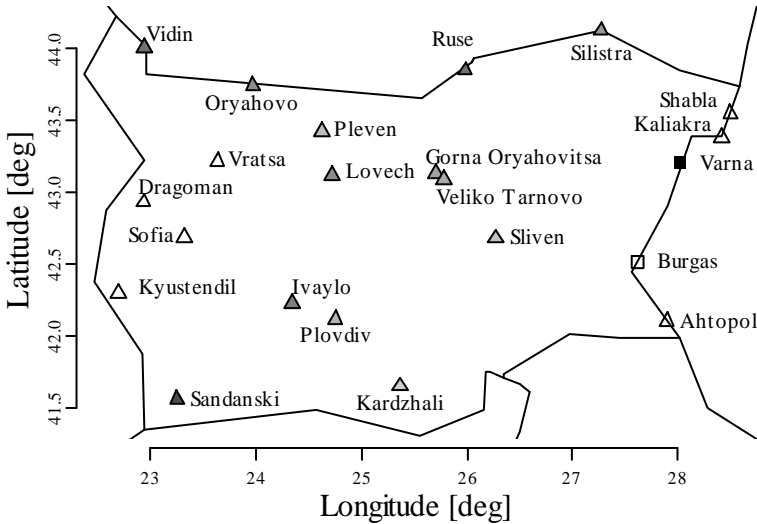


Fig. 3. Geographical partition of Bulgarian non-mountain stations via categories of daytime heat hazard during the warm period May-October.

see also an increasing hazard of category *Extreme caution + Danger* in direction south-north. The deviations from average *Extreme caution + Danger* of these stations vary from 0.3% from Kardzhali to 8.9% and 14.6% for Vidin and Sandanski respectively, 4.3% on average. The stations Varna and Burgas are intentionally marked by squares since they infringe to a certain extent our classification. While the deviations of Varna are -0.1%, on category *No stress*, 2.5% on *Caution* and -2.5 on *Extreme caution + Danger* the deviations of Burgas on the same categories are 0.6%, 4.1% and -4.8%.

Summarizing, the stations with lower than average heat hazard are close to west and east borders of Bulgaria. The more hazardous stations are at Danube and in central belt between western and eastern Bulgaria. Their hazard of category *Extreme caution + Danger* generally increases in direction south-north.

Heat waves

In this section we deal with the heat waves in Bulgaria during the period 2003-2012. To define a heat wave we use the criteria based on the excessive heat alert of National Weather Service, Chicado, IL (<http://www.crh.noaa.gov/lot/?n=wwadef>). Namely, we recognize a heat wave if the maximum *HI* reaches 37.8-40.6 °C and the minimum *HI* stays above 23.9 °C for three consecutive days, or the maximum *HI* reaches 40.6-43.3°C for two consecutive days, or the maximum *HI* climbs to 43.3 °C and over for one day. If

there is a heat wave we define its duration as the maximum number of successive days that satisfy some of above mentioned criteria.

Generally the heat waves are comparatively rare events. The heat wave during the period 22-25 Jul 2007 is with broadest coverage and intensity. It is depicted on Figure 4. The bold face numbers give the duration of the heat wave at respective stations. The plain

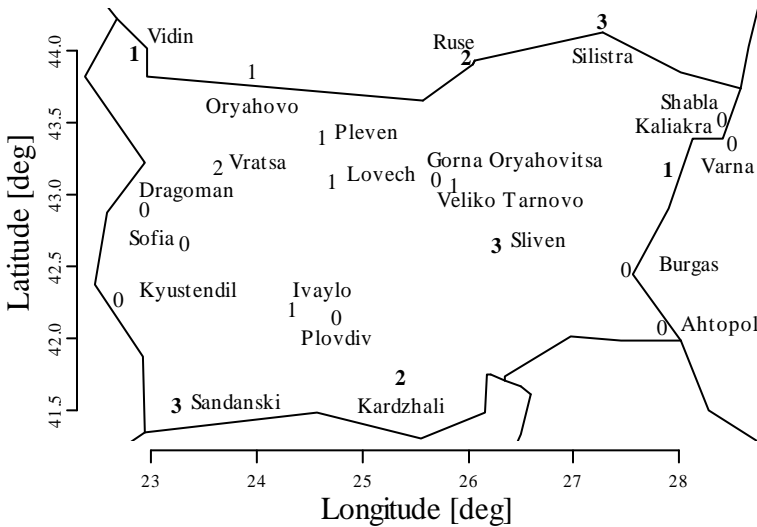


Fig. 4. Coverage and duration of the heat wave 22-25 Jul 2007.

text indicates a lack of heat wave but presence of the days that share some of our formal criteria for a heat wave. As seen, at stations Silistra, Sliven and Sandanski the duration of the wave is 3 days, at stations Ruse and Kardzhali is 2 days and at Vidin and Varna only one day. The conditions are most severe at Sandanski where daytime *HI* reaches 42.2 °C although the humidity is low. At Silistra the maximum daytime *HI* falls to 39.6 °C but the nighttime *HI* stays above 27 °C for three consecutive days. At Ruse and Kardzhali the maximum *HI* vary from 40.8 °C to 42.0 °C and 41.8 °C respectively. At Varna and Vidin the heat waves are only one-day but with highest *HI* of 44.0 °C and 43.3 °C correspondingly. Formally, at Vratsa, Oryahovo, Pleven, Lovech, Veliko Tarnovo and Ivaylo there are not heat waves in view of short duration. At Vratsa the maximum *HI* is 38.6 °C and 39.5 °C and above 24.8 °C and 25.5 °C in the night for 2 consecutive days. The daytime *HI* climbs to 42.9 °C at Oryahovo, 41.0 °C at Pleven, 41.2 °C at Lovech and 40.9 °C at both Veliko Tarnovo and Ivaylo. There are neither days nor nights with accordance of our criteria at Kyustendil, Sofia, Dragoman, Plovdiv and Gorna Oryahovitsa. While in Burgas and Ahtopol we have only one night with *HI* above 23.9 °C, at Shabla the hot nights are 3 and at Kaliakra 4.

The year 2012 is also with heat waves. The wave 23-25 August covers Ruse, Vratsa and Veliko Tarnovo. Its duration at Ruse is 3 days where maximum *HI* reaches 41.3 °C on August 25. At Vratsa we have two consecutive days with maximum *HI* of 40.6 °C.

At Veliko Tarnovo the duration of the wave is only one day but the *HI* climbs to 49.3 °C due to very high humidity. The July of 2012 is also very hot, but in our sample we find only one heat wave. It is during 15-16 July at Kardzhali with maximum *HI* 42.9-41.5 °C.

The mid-August of 2010 is hazardous at the area of Varna. During 11-14 August we have 4 days with maximum *HI* of 38.0-39.3 °C and minimum *HI* of 26.0-27.7 °C. At Kaliakra there is not formal heat wave, but the nights are very hot. During 11-20 August the night-time *HI* is above 25.4 °C on August 19 and 30.9 °C on August 14.

Summarizing, the heat waves in our sample of stations are throughout the second half of our ten-year period and they are mainly in the North and South Bulgaria. Note, that in contrast to the prolonged and intense heat wave in western and southern Europe we do not find any heat waves in our data during Jun-August 2003.

Summary and conclusion

The objective of this paper was an estimation of the heat stress risks at 27 Bulgarian weather stations during 2003-2012 period. The *HI* was used for this purpose. We categorize the *HI* into 5 levels of risk, cross-classify its daily extremes on the stations and the risk categories and build 3 frequency tables.

The analysis of the frequency tables for daily maximum *HI* and daily minimum *HI* shows that there is not any day of category *Extreme danger* in the data, the mountain stations Musala, Botev Vrah and Cherni Vrah come totally under category *No stress* and there are only isolated cases of category *Caution* at stations Murgash and Rojen. The survey of the tables shows also that the stressed nights are only 4.4 on average and in practice there is not some heat stress during the cold season November-April. With a high level of certainty we can conclude that the potential risks of heat stress in Bulgaria are only at the non-mountain stations and only during the days of the warm period May-October.

The frequency table for the non-mountain stations and the warm period May-October shows that average station profile on the risk categories *No stress*, *Caution* and *Extreme caution + Danger* is 57.3%, 30.0% and 12.7% respectively. So, during the warm period nearly half of the days are stressed by heat but the cases of category *Caution* exceed more than two times that of the category *Extreme caution + Danger*. In the context of hazard this means that the chance for a fatigue with prolonged exposure and physical activity is at least two times more than a possible sunstroke, a muscle cramp or a heat exhaustion. As for the days of category *Danger* when sunstrokes and the heat exhaustions become likely and the heat stroke possible, they are very rare, only 3.1 days on average for the whole period under consideration. So, we can conclude that despite of the fact that during the warm period May-October nearly half of the days at non-mountain Bulgaria are on average stressed by heat, the days with higher levels of hazard are very rare events.

The biplot for the warm period May-October clearly splits the non-mountain stations into two groups. While the stations in first group have positive deviations of their profiles from average on category *No stress* and negative deviations on *Caution* and *Extreme caution + Danger*, the stations in the second group have negative deviations on category *No stress* and positive on *Caution* and *Extreme caution + Danger*. This means that the stations in the second group are more hazardous than the stations in the first one. In

geographical context the stations with lower than average heat hazard are close to west and east borders of Bulgaria. The more hazardous stations are at Danube and in central belt between western and eastern Bulgaria. More careful inspection shows that generally the hazard of higher risk category *Extreme caution* + *Danger* increases in direction south-north

The analysis of the heat waves shows that they are comparatively rare events in Bulgaria. We detect only 4 heat waves that meet the requirements of our definition of a heat wave. The heat wave during the period 22-25 Jul 2007 has the broadest coverage and intensity. The wave 23-25 August 2012 is next as coverage. Two other registered heat waves are during 11-14 August 2010 but only at area of Varna and 15-16 July 2012 at Kardzhali. We do not find any signs of prolonged and intense heat wave in western and southern Europe during Jun-August 2003. Note that the heat waves in our sample of stations are only throughout the second half of the ten-year period under consideration

References

- Greenacre, M.J., 1993. Biplots in correspondence analysis, *Journal of Applied Statistics*, 20, 251-269.
- Gabriel, K.R. and Odoroff, C., 1990. Biplots in biomedical research, *Statistics in Medicine*, 9, 469-485.
- Koppe C., Kovats S., Jendritzky, G., Menne B.; Baumüller, J., Bitan, A., Jiménez, J.D., Ebi, K.L., Havenith, G., Santiago, C.L., Michelozzi, P., Nicol, F., Matzarakis, A., McGregor, G., Nogueira, P.J., Sheridan, S. and Wolf, T. 2004. Heat-waves: risk and response, *World Health Organization Environmental Change SERIES*, No.2, Regional office for Europe.
- NWS (National Weather Service), 1994. Excessive heat watch, warning and advisory heat index criteria. *Regional Operations Manual*. Letter E-5-94, Eastern Region, NWS, Bohemia, NY.
- Robine, J.M., Cheung, S.L.K., Le Roy, S., Van Oyen, H., Griffiths, C., Michel, J.P. and Herrmann F.R. 2008. Death toll exceeded 70,000 in Europe during the summer of 2003. *Comptes Rendus Biologies*, 331, 171-178.
- Robinson, P.J., 2001. On the definition of a Heat Wave. *Journal of Applied Meteorology*, 40, 762-775.
- Rothfus, L.P., 1990. The heat index "equation" (or, more than you ever wanted to know about heat index). *NWS Tech. Attachment*, SR 90-23, 2.
- Shoen, C., 2005. A New Empirical Model of the Temperature-Humidity Index, *Journal of Applied Meteorology*, 44, 1413-1420.
- Starr C. and Mcmillan, B., 2008. *Human Biology*. 8th ed., Belmont: Brooks/Cole.
- Steadman, R.G., 1979. The assessment of sultriness. Part I: A temperature-humidity index based on human physiology and clothing science. *Journal of Applied Meteorology*, 18, 861-87

Рисковете от горещините в България през периода 2003-2012

В. Иванов, С. Евтимов

Резюме: За оценка на рисковете от топлинен стрес в България през периода 2003-2012 години, е използван е набор от 27 метеорологични станции. За тази цел, са използвани стойностите на heat index на Steadman в основните и междинните синоптични срокове. Интервалът от стойности на heat index е рекодиран в пет нива на риск, и наблюденията са класифицирани по станции и категории на риска. Три честотни таблици са създадени и анализирани. Направен е биплот на таблицата на непланинските станции по време на топлият период Май-Октомври, и станциите са клъстеризирани според рисковете. Установено е географското разпределение на рисковете от топлинен стрес. Дискутирани са топлинните вълни по време на разглежданият период.

SIMPLE POSTPROCESSING METHOD FOR VERTICAL CORRECTION BASED ON STRATIFIED NEAR-SURFACE ATMOSPHERIC PARAMETERS

H. Chervenkov

National Institute of Meteorology and Hydrology, blvd Tsarigradsko Shose 66, Sofia 1784, Bulgaria,
e-mail: hristo.tchervenkov@meteo.bg

Abstract. The paper presents shortly a relatively simply and transparent, but meteorologically consistent method for physical interpolation with vertical correction to arbitrary points of interest, based on the distributed three dimensionally and stratified near-surface atmospheric parameters. Such procedure is needed relatively often in various environmental studies, when the output of some meteorological model has to be adjusted more precisely to location with known elevation, using one or other postprocessing technique. The original authors' proposal is described and demonstrated briefly using as test dataset the output of regional climate model RegCM4 for the monthly mean temperature for the year 2000 over Bulgaria and records from the station observations in the NIMH-BAS network.

Key words: Postprocessing, Physical interpolation, Vertical correction, RegCM4, Near-surface atmospheric stratification

Introduction

Practically all spatially distributed hydrological and ecological models need certain meteorological information, most frequently formatted as initial dataset, containing the values of some input parameters. Thus, for instance, they use air temperature to drive processes such as evapotranspiration, snowmelt, soil decomposition, and plant productivity. Since most near-surface air-temperature data are collected at irregularly spaced point locations (for example the network of the measurement stations) rather than over continuous surfaces, the point-based temperatures must be accurately distributed over the landscape in order to be useful in spatially distributed modelling. On other hand the output of various atmospheric circulation models (ACM), either for numerical weather prediction,

or for simulation of the global and regional climate, is presented most often with finite resolution, i.e. as distribution of the values in the gridpoints or gridcells of fixed mesh. Depending on the model and its concrete implementation, the spatial (horizontal and vertical) step is changed up to two orders, but typical values for the horizontal one of the contemporary hydrostatic numerical weather prediction and regional climate models is 8-10 km. The computational process of the ACM uses model representation of the topography, which more or less differs from the real one. Thus, generally speaking, due to the vertical displacement, even the perfect model can produce different outcome from the unbiased measurement (the objective “truth”) in horizontally collocated point. Key point in the model verification studies is to distinguish the differences, caused by such reasons, from those by the model physics weaknesses. Further, from practical point of view, in many local environmental studies, where the typical resolution is 1-2 km, to use directly meteorological input with (significantly) coarser resolution can lead to serious biases in the results. A pragmatic way to overcome this problem in the case when high-resolution data are not available, is to use different subgridding techniques, either incorporated in the model system as in Giorgi et al., 2003 and in Im et al., 2010 or in external form, as post processing procedures. Due mainly to the enormous complexity of the modern ACM, the second approach is much more easily feasible for the end-user, which in the common case utilizes this model as encapsulated meteorological driver for his specific tasks. Several methods exist for spatial interpolation of point-based data, including inverse-distance weighting (IDW), kriging, 2-dimensional splines, and trend-surface regression (Myers, 1994). They can be purely mathematical as the listed above, or combined - mathematical based on physical assumptions. As stated in Dodson and Marks, 1997, these methods often work well over relatively flat, homogeneous terrain. In mountainous terrain, however, the strong relationship between vertically stratified meteoroparameters and elevation precludes a simple interpolation of point-based observations. Unless the effect of elevation on, for example, the temperature is explicitly accounted for, an interpolation can produce grossly inaccurate results. For example, in the case where a set of temperature observations or the model gridpoints are located around the base of a mountain, an interpolation which ignores elevation would seriously overestimate the temperature at the mountain top, as it would not account for the fact that temperature generally decreases with increasing elevation.

The presented work describes one proposed by the author physically based interpolation technique, which can be easily implemented in various applications. The scheme is very simple and transparent and can be used for any vertically stratified parameters (temperature, humidity characteristics).

The rest of the paper is organized as follows: The proposed innovative approach is described and briefly commented in Section 2. A numerical experiment, demonstrating the possibilities of the scheme, is described in Section 3. The last section contains discussion and concluding remarks.

Methodology

To test the capabilities of the novel scheme, it is forced to reproduce the value of some stratified meteoroparameter in selected reference point, from some discrete 3D

distribution of the same. A meteorological station is located in this point and the measurements there are accepted as objective truth. Thus, the closeness of the reproduced value to the measured one is treated as estimation of the methods quality.

The most widely used approach for assessing the departure of the model output to the measurements in the numerical simulation studies is to compare them with the obtained results in the nearest gridpoint. As stated above however, for many problems, like model performance evaluation and local high-resolution issues, to rely only on this approach is not sufficient. Obviously many other techniques based either on purely mathematical or mathematical and physical assumptions can be applied, but the testing of sophisticated schemes is out of the scope of our work. Instead, along with the “nearest gridpoint” approach, we will present one innovative technique. Basic fact in meteorology is that the heterogeneity of the atmosphere in vertical direction is significantly stronger than in horizontal one. That’s why it is essential to account this effect, especially over a complex terrain, for the stratified variables like, for example, the temperature. The scheme on figure 1 illustrates, for simplicity in one dimension, the original authors’ idea.

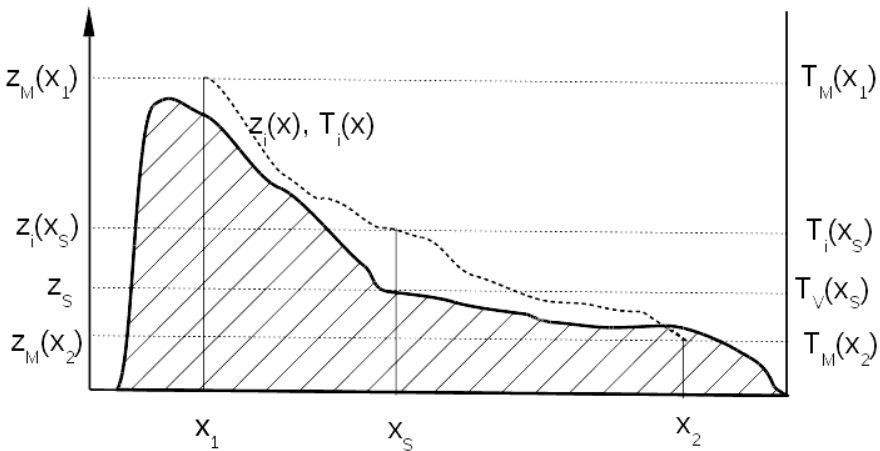


Fig. 1. Explanatory illustration of the proposed method

Let the dashed area sketches the terrain cross-section along the line between the gridpoints x_1 and x_2 , which surrounds the point of interest with coordinate x_s . It is always possible to construct local continuous (with IDW or any other interpolation method) function $z_i(x)$ describing the dependence of the elevation from the horizontal coordinate, as depicted with dotted line on figure 1. The defined in equation (1) IDW is deterministic interpolator, where β is a positive real number, called the power parameter. The smoothness (if $\beta > 1$) and computational feasibility makes the IDW preferable in many applications, as the presented here.

$$P_i(\beta) := \frac{\sum_{j=1}^n \frac{P_j}{r_j^\beta}}{\sum_{j=1}^n \frac{1}{r_j^\beta}} \quad (1)$$

In this implementation P is the surface temperature T , $n=4$ and, correspondingly, T_1, T_2, T_3, T_4 , are the values in the nearest four (i.e. the surrounding) gridnodes, r_1, r_2, r_3, r_4 , are the distances between them and the station location, and traditionally β is set to two. Thus, equation (1) can be rewritten as:

$$T_i = \frac{\sum_{j=1}^4 \frac{T_j}{r_j^2}}{\sum_{j=1}^4 \frac{1}{r_j^2}} \quad (2)$$

To find the IDW-value T_i , is necessary to locate the station in the grid first and, second, to find the distances. The first task is solved with efficient binary search, and the second – with procedure based on the haversine formula, keeping in mind that the geographical coordinates of the station and the gridpoints are known. The haversine formula gives the great-circle distance d between two points on a sphere (i.e. Earth) with radius R from their longitudes λ_1, λ_2 and latitudes φ_1, φ_2 :

$$d = 2R \arcsin \left(\sqrt{\sin^2 \left(\frac{\varphi_2 - \varphi_1}{2} \right) + \cos(\varphi_1) \cos(\varphi_2) \sin^2 \left(\frac{\lambda_2 - \lambda_1}{2} \right)} \right) \quad (3)$$

Similarly, knowing the values of the considered variable T , say for definiteness the temperature, in the gridpoints x_1 and x_2 , namely $T_M(x_1)$ and $T_M(x_2)$, we can obtain also the temperature interpolation function $T_i(x)$. In the common case, however, the interpolated elevation at point x_S $z_i(x_S)$ differs from the actual z_S , which, as x_S , is a priori known. Assuming, that the atmosphere in this layer is polytropic, i.e. linearly stratified and according the definition for the vertical gradient (lapse rate), we can compute it as follows:

$$\gamma = -\frac{\partial T}{\partial z} \approx -\frac{\Delta T}{\Delta z} = -\frac{T(z_2) - T(z_1)}{z_2 - z_1}, \quad z_2 \neq z_1 \quad (4)$$

Equation (4) can be generalized, where ϵ is small positive number:

$$\gamma = \begin{cases} -\frac{T(z_2) - T(z_1)}{z_2 - z_1}, & z_2 - z_1 > \varepsilon \\ 0, & z_2 - z_1 \leq \varepsilon \end{cases} \quad (5)$$

or for the used in figure 1 notation

$$\gamma_M = \begin{cases} -\frac{T_M(x_1) - T_M(x_2)}{z_M(x_1) - z_M(x_2)}, & z_M(x_1) - z_M(x_2) > \varepsilon \\ 0, & z_M(x_1) - z_M(x_2) \leq \varepsilon \end{cases} \quad (6)$$

Such generalization is needed obviously to avoid the division by zero when the gridpoints are with equal altitudes. The threshold ε can be set, for instance, to 0.1 m as in our implementation.

The basic idea of the proposed approach is to interpolate the altitude z and the temperature T to the coordinate x_s yielding $z_i(x_s)$ and $T_i(x_s)$ correspondingly. Then, using the calculated with equation (3) lapse rate, we can adjust $T_i(x_s)$ to the real elevation adding vertical correction factor, proportional to the difference between the interpolated $z_i(x_s)$ and the real altitude z_s , in the following manner:

$$T_v(x_s) = T_i(x_s) - \gamma_M (z_i(x_s) - z_s) \quad (7)$$

In the case of the two-dimensional generalization, six different gradients can be defined between the values of the searched variable, with respect to the elevations of the four surrounding gridpoints. Intending to bound possibly thicker (and thus more representative) layer, the gradient between the lowest and highest gridpoint is taken under consideration in the current implementation.

The obvious merits of the proposed scheme are its clear physical sense and computational simplicity. The method is based on the linear stratification assumption, which, on one hand, is significantly smaller constrain than some in other techniques (for comprehensive review see – Dodson and Marks, 1997), where the gradient is prescribed to a constant over the whole domain. On the other hand, this stratification is confirmed by many experimental studies of lower-level atmosphere. Another strong point of the method is its locality – the gradient is calculated separately for every gridcell, which is more close to the physical reality, where the vertical distribution of the atmospheric parameters can vary greatly from point to point. As a drawback of the method could be pointed the fact, that in some cases the station can be not situated between the gridpoints in vertical direction. So, for instance, if the station is on the top/bottom of a convex/concave terrain segment and the gridpoints on its periphery, the method cannot retrieve the actual gradient at the altitude of the point of interest.

Numerical experiment

To demonstrate the possibilities of the proposed approach, the obtained results during sensitivity study of the regional climate model RegCM version 4 (for description see Pal et al., 2007 and references therein) over the territory of Bulgaria are used. The considered part of the model output consist of data for the monthly mean surface temperature in grid with 10×10 km resolution which are compared with the averages from the measurements in 30 stations of the network of NIMH-BAS. The model outcomes are compared with the observations using three methods: observation – nearest gridpoint (noted further as “mode 1”), observation – IDW value (“mode 2”) and observation – vertically corrected value with the above described procedure (“mode 3”). According equation (7) the magnitude of the vertical correction is proportional to the vertical displacement between the interpolated and real altitude, which, itself, depends from the mesh properties, but generally decreases by higher resolutions. Thus, to emphasize the impact of this correction, two stations, Kyustendil and Kasanlak, with significant displacement from the mesh are used in the performed tests. In most practical tasks however, such postprocessing procedures are applied on the whole dataset in the domain, rather than on selected stations. Further, such test can be treated as much more consistent way for overall method performance evaluation. Table 1 shows the positional parameters for the selected two stations – the distance to the nearest gridpoint r_{min} , the real altitude z_s , the altitudes of the four surrounding gridpoints $z_M(x_1)$, $z_M(x_2)$, $z_M(x_3)$, and $z_M(x_4)$.

Station	r_{min} , km	z_s , m	$z_M(x_1)$, $z_M(x_2)$, $z_M(x_3)$, $z_M(x_4)$, m	$z_i(x_s)$, m	$z_s - z_i(x_s)$, m
Kyustendil	1.699	520.0	1017.4, 919.2, 814.5, 859.1	862.8	-342.8
Kasanlak	5.350	392.0	561.6, 677.3, 662.3, 520.7	623.8	-231.8

Table 1. Positional parameters of the selected stations, identified with their World Meteorological Organisation (WMO) code.

Results and comments

The (calculated from the) observed values of the monthly mean temperature for the year 2000 are compared with the model output using the three commented above methods.

Common approach to assess the degree of agreement of the observed (measured) values O_i and their modelled correspondents M_i (in the presented study in the three modes) is to calculate certain statistical measures, among which most widely used are the root mean square error (*RMSE*), the correlation coefficient (also termed the Pearson correlation coefficient, *R*), the index of agreement (*IA*) and the mean bias (*BIAS*). Explicit formulas for the first two will not be given due to their popularity, and the last two are equal accordingly to:

$$IA = 1 - \frac{\sum_{i=1}^N (O_i - M_i)^2}{\sum_{i=1}^N \left(|M_i - \overline{O}| + |O_i - \overline{O}| \right)^2} \tag{8}$$

$$BIAS = \frac{1}{N} \sum_{i=1}^N (O_i - M_i) \tag{9}$$

The summation is along the number of comparisons N and the overlines notes averaging. The (dimensionless) index of agreement condenses the differences between observed and modeled values into one statistical quantity. It provides a measure of the match between the departure of each prediction from the observed mean and the departure of each observation from the observed mean. The index of agreement has a theoretical range of 0 to 1, with a value of 1 suggesting “perfect” agreement. The mean bias is simply the average bias between the observed and modeled values.

The calculated statistical quantities are summarized in Table 2.

	RMSE, °C	R	IA	BIAS, °C
Mode 1	1.112	0.992	0.995	0.197
Mode 2	1.144	0.991	0.995	0.225
Mode 3	0.923	0.995	0.997	-0.224

Table 2. Main features of the selected cyclones according column caption

Similar statistical treatment for the selected two stations is hampered by the insufficient length of the time series – only 12 values are available. That’s why the results for this comparison are presented only graphically, as shown on figure 2.

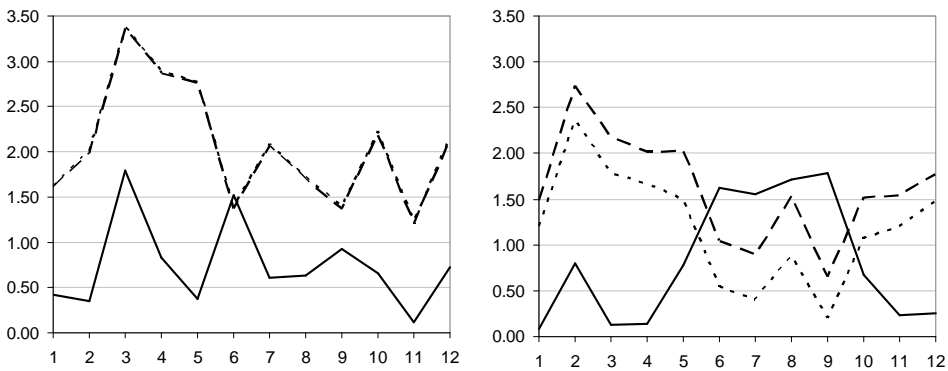


Fig. 2 Absolute biases (i.e. |obs-mode n|) of mode 1 (dashed line), mode 2 (dotted line) and mode 3 (normal line) for station Kyustendil (Left) and Kasanlak (Right).

According the listed in table 2 values of the statistical quantities can be stated, that the overall (i.e. for the whole dataset of stations) performance in the three modes is practically equal. Probably the influence of the good behavior for some stations is masked by the bad one for others. The interpretation of figure 2 leads to the same conclusion. For the selected

stations, however, the influence of the proposed method for vertical correction is discernible and significant. In all months, except one for the first station and except four for the second one, the vertically corrected values are apparently closer to the measurements. Reason for the opposite situation during the summer months can be weaknesses in the planetary boundary layer (PBL) parameterization in hot days with prevailing unstable stratification. In this case the correction adds biases to the modelled value. The differences between mode 1 and mode 2 are smaller, in case of the first station practically indiscernible, due most probably to the relatively high horizontal resolution. Deeper conclusions with significant confidence, however, can be obtained after further statistical treatment of relevantly longer time series.

Conclusion

The presented short study can be observed as concise demonstration of the proposed by the author postprocessing method for vertical correction to the point of interest of model output containing values of stratified parameters, in particular the temperature. The method is very simple, and, utilizing explicitly the three-dimensional structure of the model output, physically consistent and transparent. Keeping in mind that almost all ACMs uses terrain-following coordinate systems, such 3D-distribution is the common case. The presence of data for the considered variable at different altitude practically in all gridcells allows the calculation of the local lapse rate and as consequence the vertical correction. The discussed examples for two stations shows, that in the most cases this method produces noticeable closer to the measurements results, even when the point of interest is outside the layer, in which the lapse rate is calculated. In other cases, however, the results are worse, and thus the method has to be applied carefully, preferably point-by-point of interest. Statistical processing of longer datasets and records can be performed aiming to reveal a priori criterion when the method is applicable or not. Nevertheless the proposed technique illustrates a possible pragmatic way to adapt the available model output physical consistently to the specific needs of the end-user who looks for concrete value in the arbitrary point of interest.

References

- Giorgi, F., Francisco, R., Pal, J., 2003 Effects of a subgrid-scale topography and land use scheme on the simulation of surface climate and hydrology. Part I: Effects of temperature and water vapor disaggregation. *J. Hydrometeor.*, 4(2): 317-333.
- Dodson, R., Marks, D., 1997 Daily air temperature interpolated at high spatial resolution over a large mountainous region *Clim Res Vol. 8*: 1-20.
- Im, E.-S., Coppola, Giorgi, F., Bi, X. 2010 High Resolution Regional Climate Model for the Alpine Region and Effects of a Subgrid-Scale Topography and Land Use Representation, *J. Climate vol. 23* 1854-1873.
- Myers DE 1994 Spatial interpolation. An overview. *Geoderma* 62(1):17-28
- Pal JS, Giorgi F, Bi X, Elguindi N and others 2007 Regional climate modelling for the developing world: The ICTP RegCM3 and RegCNET. *Bull Am Meteorol Soc* 88: 1395-1409

Прост постпроцесорен метод за вертикална корекция основан на тримерно разпределени и стратифицирани атмосферни параметри в близост до подложната повърхност

Хр. Червенков

Резюме: Статията представя накратко един сравнително прост и обозрим, но метеорологически съдържателен метод за физическа интерполация с вертикална корекция към конкретна точка на интерес, основана на тримерно разпределени и стратифицирани атмосферни параметри в близост до подложната повърхност. Подобна процедура е необходима сравнително често в различни изследвания на околната среда, в които изходните данни от числен атмосферен модел трябва да се сведат по-прецизно до определено място с известна надморска височина, посредством една или друга постпроцесорна схема. Оригиналното авторско предложение е описано и демонстрирано в синтезиран вид, използвайки за тестов набор данни изхода на регионалния климатичен модел RegCM4 за средномесечната температура за 2000 година и записи от станционните наблюдения на НИМХ-БАН

Ключови думи: Постпроцесорна процедура, Физическа интерполация, Вертикална корекция, RegCM4, Атмосферна стратификация в близост до подложната повърхност

STUDYING THE FOGS IN SOFIA WITH CHERNI VRAH-SOFIA STABILITY INDEX

A. Stoycheva^{1,2}, S. Evtimov²

¹National Institute of Meteorology and Hydrology, Bulgarian Academy of Science, Forecasts Department, 66 Tsarigradsko shose Blvd., Forecasts Department, 1784 Sofia, Bulgaria, e-mail: anastassia.stoycheva@meteo.bg

²Sofia University St. Kliment Ohridski, Faculty of Physics, Meteorology and Geophysics Department, 5 James Bourchier Blvd., 1164 Sofia, Bulgaria, e-mail: evtimov@phys.uni-sofia.bg

Abstract. A study of the fogs at Sofia, Bulgaria is carried out by the means of proposed Cherni vrah-Sofia Stability Index. By measuring the strength of static stability of the atmospheric layer over Sofia, this index depends only on the surface air temperatures at stations Sofia, Mladost and Cherni vrah and hence it is potentially useful in operational practice. By using the standard weather observations during 01/01/1992-17/12/2014 period, a simple statistical relationship between our index and horizontal visibility in Sofia is established. It is statistically correctly found that while the fogs in Sofia correspond to higher values of the index, the absence of fog favours the lower index values. This general conclusion is supported by a case study investigation of the typical for Sofia fog episode.

Keywords: fog, Sofia, Cherni vrah, index of static stability

Introduction

The considerable development of numerical models in recent decades has not yet led to significant progress in fog forecasting. The still not enough adequate model parameterisation of specific processes leading to the formation, development and dissipation of fog in the boundary layer is one of the main sources for this situation. Considered as a passive phenomenon, because the formation and the dissipation processes are usually generated by a multitude combination of general and local factors, fog is difficult to be studied in scales larger than those occurring locally (Pinheiro et al., 2006).

Holtslag et al. (2010) examine whether empirical methods like those developed in the 60s and 70s are reasonable alternative forecast tools. It appears that the so called Fog Stability Index, solely based on routine radio sounding observations, has reasonable skills. This index has been optimised for 12 stations in the Netherlands, after which it reached a

high forecast skills. It appears that the Fog Stability Index scores better than direct model output, and performs reasonably once optimised for site specific conditions.

Dejmal and Novotny (2011) test the applicability of the Fog Stability Index for the prognosis of low visibility cases at 5 stations in the Czech Republic. Four different criteria are used for assessment of forecasts. Based on the large number of cases dealt with, these authors found that during the winter the accumulation of cold air near the ground happens mainly in the valleys and river basins.

Haines (1988) developed the Lower Atmosphere Stability Index to indicate the potential for wildfire growth where the ground wind is not the dominant factor. The stratification of the lower atmosphere is estimated by combining the temperature difference between two atmospheric layers, and the moisture determined by the temperature and dew point difference.

Entirely statistical methods for fog analysis and forecast are also widely used. Robasky and Wilson (2006) seek to apply statistical forecast approaches using routinely available weather observations, such as standard hourly surface observations and twice-daily upper air balloon soundings. Maier et al. (2013) divided into stages the lifecycle of three episodes with fog during autumn 2011 in central Germany with objective statistical methods. Croitoru et al. (2011) conducted a study on the spatial variability of fog in the northwestern part of Romania by various multivariate statistical techniques. The time series of the average annual, seasonal and monthly number of days with fog are used for this purpose.

In present paper we use the standard SYNOP data at meteorological stations Sofia, Mladost and Cherni vrah for studying fogs at Sofia during 01/01/1992-01/12/2014 period. The base toll, we offer is a specific index, which we name Cherni vrah-Sofia Stability Index. Based on conception of Brunt-Väisälä's frequency, our index estimates the strength of the static stability of the atmosphere layer over Sofia. The index can simply be calculated by surface air temperature at stations Sofia and Cherni vrah. It should be noted that Godev and Takev (1968) point out the temperature difference between Sofia and the Cherni vrah as one of the factors for early spring night temperature decreases at Sofia in anticyclone weather. There is also a purely ordinary reason to offer our index. As it is well known, the fogs in Sofia generally are attended by strong temperature inversions. Zverev (1957) points out that among many others, the formation of temperature inversion layer in altitude is one of the main symptoms for predicting fog trough sounding data. Unfortunately the soundings in Sofia, Mladost are made only once in 24 hours, at 12 GMT. On the other hand, the duration of the fogs at Sofia usually continues several synoptic periods. The idea is that the regular synoptic observations at the proximity stations Sofia (595 m) and Cherni vrah (2292 m) to be considered as repeated 3 hours soundings of the atmosphere and this additional information to be used to refine the short range forecast of the fog. In this context, the proposed index realises our idea.

Data and pre-processing

The data we use is from regular observations at the Bulgarian meteorological stations Sofia, Mladost (42°41'N, 23°19'E; 595 m) and Cherni vrah (42° 35' N, 23° 16' E;

2292 m) during the 01/01/1992-17/12/2014 period. Actually, these are decoded SYNOP reports of National Institute of Meteorology and Hydrology, Bulgarian Academy of Science for observations in primary and intermediate synoptic hours 00, 03, 06, 09, 12, 15, 18 and 21 CMT. For station Sofia, Mladost we extract the time series of surface air temperature, horizontal visibility and the present and past weather group. For station Cherni vrah we use only time series of surface air temperature. The length of each record is 66486 points at sampling interval of 3 hour.

We define and compute our index of stability which we term Cherni vrah-Sofia Stability Index (CSSI) by the following formula:

$$\text{CSSI} = \sqrt{(1 + \Delta t / 17) / (1 + t_{\text{Cherni vrah}} / 273.15)},$$

where Δt is the temperature difference between Cherni vrah and Sofia, Mladost and $t_{\text{Cherni vrah}}$ is surface air temperature at station Cherni vrah in degrees Celsius. What is the physical base of CSSI? As known the so called Brunt-Väisälä's frequency $N^2 = g T^{-1} (\gamma_a + dT/dz)$, where g is acceleration due to gravity, T is absolute temperature, $\gamma_a \approx 1 \text{ K}/100 \text{ m}$ is adiabatic lapse rate, and z is altitude, measures the local strength of the static stability of the dry atmosphere (Belinskii, 1948; Holton, 1972). The higher values of this frequency appropriate the higher degree of the layer stability. However, the extremes of Brunt-Väisälä's frequency are within the temperature inversion layers. Scaling down N by $\sqrt{g \gamma_a / T_0}$, where T_0 is the absolute temperature of ice melting and putting the vertical temperature gradient to be Δt divided by Cherni vrah-Sofia, altitude difference which is almost 1700 m, we get $\sqrt{(1 + \Delta t / 17) / (1 + t / 273.15)}$. Finally, we substitute t by $t_{\text{Cherni vrah}}$ and obtain just our CSSI.

Extracting the observations with CSSI higher than 0.5, we build a second data set. We also attach to this set a factor "Phenomenon" with two levels "Fog" and "No fog". While the level *Fog* corresponds to fogs and mists with horizontal visibility less or equal to 1000 m, the level *No fog* groups all other cases. We identify the cases of fogs or mists by means of the present and past weather group. The respective codes are as follows: 05.. - dry fog (haze); 10.. - mist; 11.. - patches of shallow fog; 12.. - continuous shallow fog; 28.. - fog (within past hour but not at observation time); 40.. - fog at a distance; 41.. - patches of fog; 42.. - fog, sky visible, thinning; 43.. - fog, sky not visible, thinning; 44.. - fog, sky visible, no change; 45.. - fog, sky not visible, no change; 46.. - fog, sky visible, becoming thicker; 47.. - fog, sky not visible, becoming thicker; 48.. - fog, depositing rime, sky visible; 49.. - fog, depositing rime, sky not visible.

Preliminary analysis

Figure 1 shows the parallel box plots of the CSSI for recoded into seven intervals horizontal visibility. The values of the CSSI are on vertical axis and the categorised visibility is on horizontal axis. The two bases of a box indicate the so called “hinges” (in practice first and third quartile) and thus the box height represents the interquartile range. The width of a box is proportional to the square roots of the number of observations. The medians are in the boxes. The vertical lines (“whiskers”) show the largest or smallest observation that falls within a distance of 1.5 times the interquartile range from the nearest hinge.

An inspection of Figure 1 shows that the largest number of observations falls within the intervals 5-10 km horizontal visibility. The intervals 40-50 km, 1-5 km and 10-20 km are subsequent. The cases of visibilities less or equal to 1000 m are comparative not numerous but they are more than that within intervals 20-30 km and 30-40 km.

Looking at Figure 1 we see also that there is a stable downward tendency of the CSSI up to horizontal visibilities of 20-30 km and next the CSSI climbs.

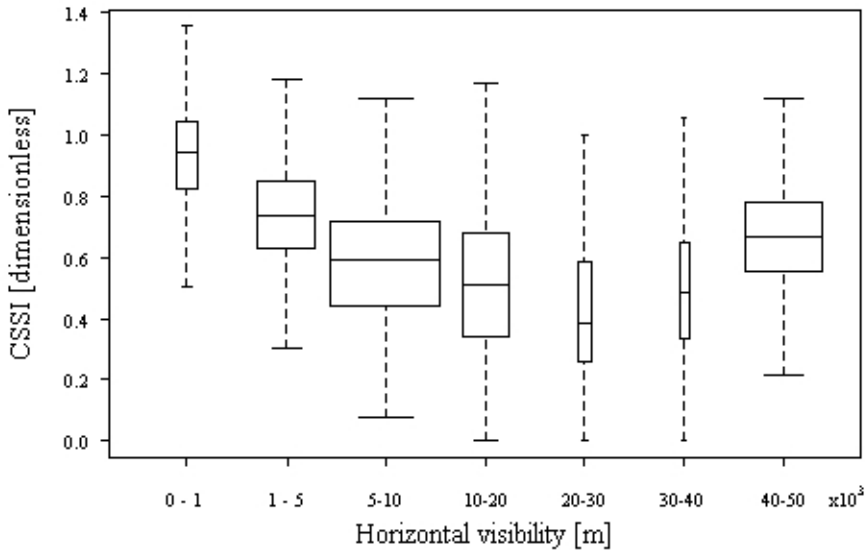


Fig. 1. Parallel box plots of the CSSI for recoded into seven intervals horizontal visibility

Testing procedures

Figure 2 shows the parallel box plots of the CSSI for two levels *Fog* and *No fog* of the factor *Phenomenon*. The figure building blocks are the same as on Figure 1 with exception of the so called “notches”, the two symmetric concavities on the vertical box walls.

As seen, the cases of fogs or mists with horizontal visibility of 1000 m are considerably less than the other cases. Indeed, while the observations in category *No fog* are 44 555, the observations in category *Fog* are only 979. When the notches of two boxes on Figure 2 do not overlap this should be interpreted as a “strong evidence” that the two medians differ. As seen, this is exactly our case and we can conclude that the medians of two groups *Fog* and *No fog* differ.

So, there is a reason to assert that the fogs or mists with horizontal visibility of 1000 m take place predominantly at higher levels of the CSSI. Further we test statistically this hypothesis. The two sample t-tests are commonly performed in such cases (Wilks, 2006). It is well known this test requires the normal distributions of the samples. In our case the samples are the groups *Fog* and *No fog* and the variable under interest is CSSI. On the Figure 2 the medians seem to be in the middles of the boxes. This should be hinted as normal distributions.

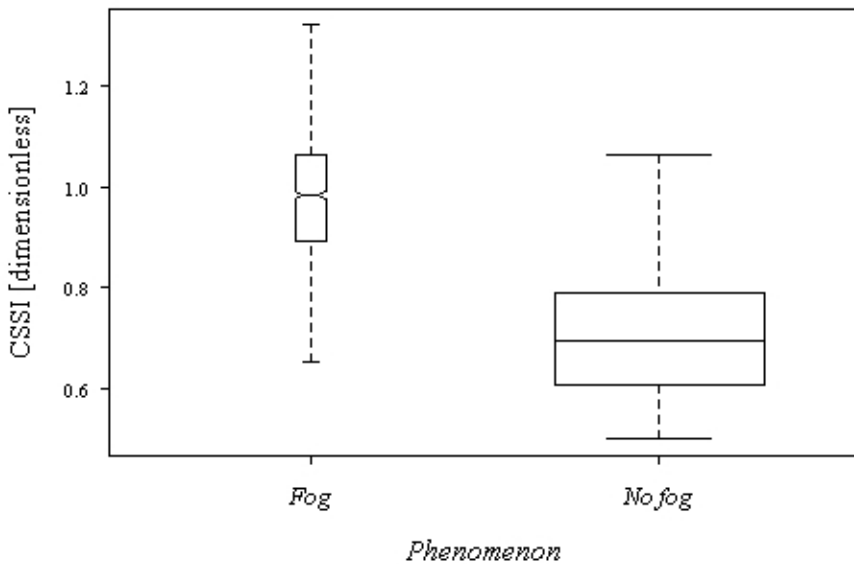


Fig. 2. Parallel box plots of the CSSI for two levels *Fog* and *No fog* of the factor *Phenomenon*

Figure 3 represents the normal quantile-quantile plots for the groups *Fog* and *No fog* of the factor *Phenomenon*. The theoretical quantiles are on the horizontal axes and sample quantiles are on vertical axes. The group *Fog* is on the left and on the right is the group *No fog*. The first and third quartiles define the straight line drawn.

As seen the left plot produces points close to the straight line and there is not a cause for concern about departures from normality for the group *Fog*. We also see that the outer parts of the experimental curve for group *No fog* are steeper than the middle part which indicates that by having heavy tails the distribution deviates from normality.

We test statistically these observations. One sample Jarque-Bera test for normality is used for this purpose. For the sample *Fog* the test statistic is 5.7087 and the p-value 0.05759. For sample *No fog* the test statistic is 3616.6571 and the corresponding p-value

2.2×10^{-16} . We are able to reject the null hypothesis of normality for the group *No fog*. So, there is not normal distribution. It is advisable in this case to use the non-parametric analogues of the t-tests. We perform the two-sample Wilcoxon Man-Whitney rang sum test. The null hypothesis is that the two populations being compared have identical distributions. The alternative hypothesis is that the population distributions differ in location, i.e. the median. In our case the W test statistic has a value of 40355923 and corresponding p-value is 2.2×10^{-16} . We are able to reject the null hypothesis of identical distributions. Sample medians are 0.9834 and 0.6943 for groups *Fog* and *No fog* respectively. Summing up, the performed statistical analysis gives strong evidence that the fogs or mists with horizontal visibility of 1000 m correspond to higher values of CSSI in comparison with cases without fog.

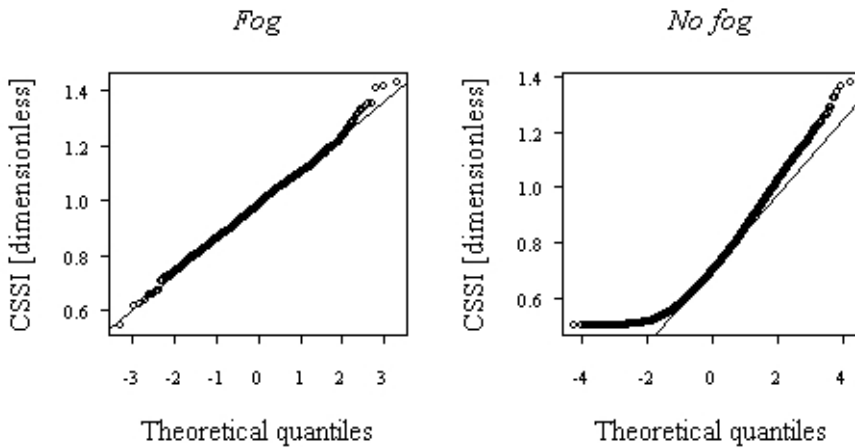


Fig. 3. Normal probability plots of CSSI for two groups *Fog* and *No fog*

A typical example

Here, we illustrate our main results by a detailed analysis of a particular situation with fog in Sofia. The analysed period is 12 00-16 12/21/2014. Figure 4 represents absolute topography maps of the 500 hPa level and the sea level pressure on 15 12/12/2014 GMT. During this period under consideration the visibility in Sofia is at its lowest on 15/12/2014, when the Balkan Peninsula is influenced by the upper ridge at the 500 hPa (Figure 4, left). During the period 13-15/12 in Sofia a high sea level pressure of 1027-1030 hPa dominates. On 15 12/12/2014 the anticyclone extends all over South-East Europe and a very deep and quite large cyclone determines the dynamic weather over North-West Europe (Figure 4, right). At this time over Balkan Peninsula the warm air mass transfers and observed temperatures at 850 hPa over Bulgaria are 6-8°C (Figure 5).

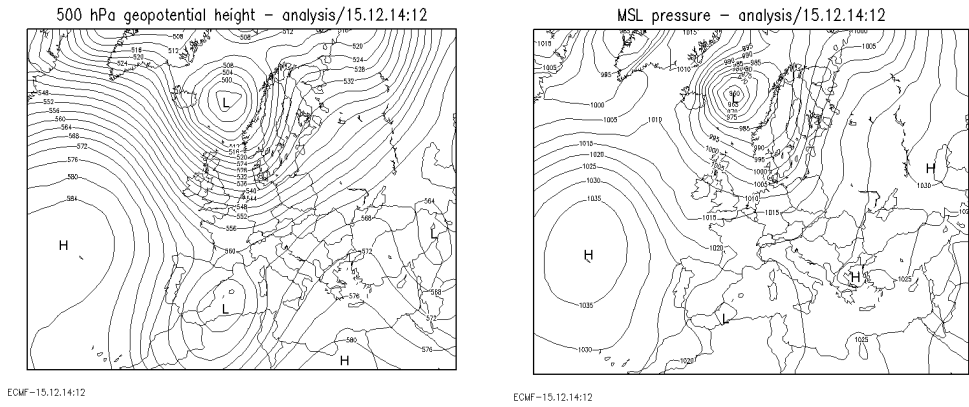


Fig. 4. Geopotential at 500 hPa (left) and sea level pressure (right); ECMWF analysis 15 12/12/2014 GMT

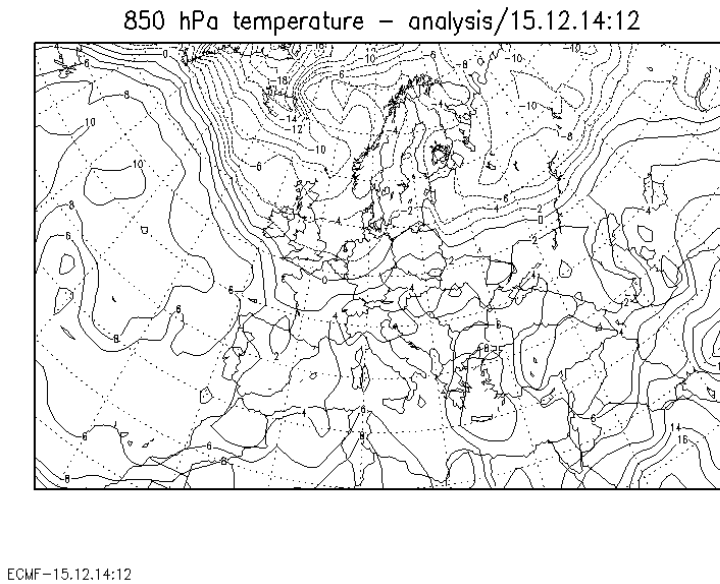


Fig. 5. Temperature at 850 hPa, ECMWF analysis on 15 12/12/2014, GMT

During the cold season, both a clear sky and a light wind in anticyclonic conditions lead to strong night radiation cooling of the earth's surface, which creates ground inversions. This is a typical scenario that produces fog. The combination between a warm spell on 850 hPa and the ground inversion leads to intensification of fog, especially in high valley field.

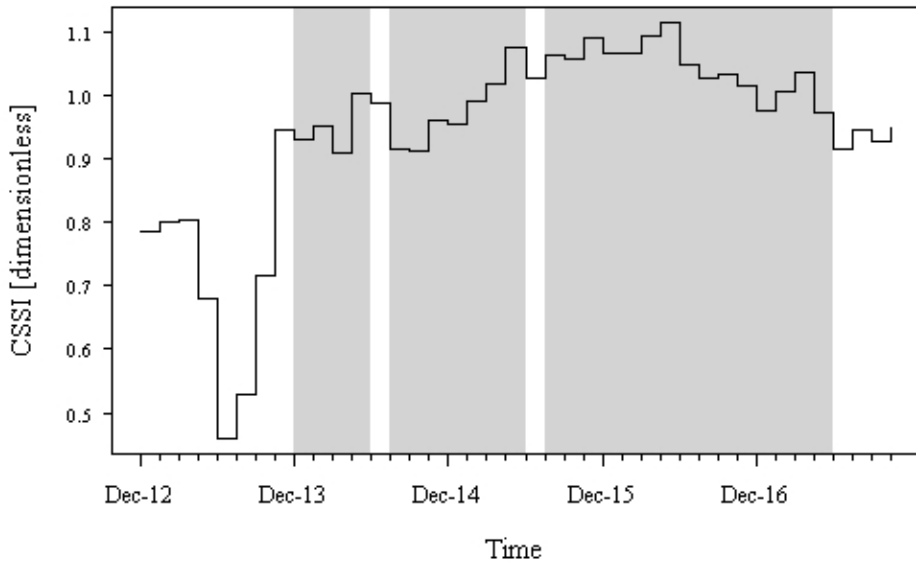


Fig. 6. Time series of CSSI in Sofia for period 12 00-16 21/12/2014 GMT

Figure 6 presents the time series of CSSI for the period 12 00-16 12/12/2014. Foggy periods are in grey. As seen, the episode with fog starts on 13 00/12/1014 and ends on 16 21/12/2014. During this episode horizontal visibility ranges from 100 m to 900 m. The two 3-hour interruptions are at 13 12/12/2014 and at 14 12/12/2014 when the visibility raises to 2000 m and 1500 m respectively.

Figure 6 clearly shows that CSSI sharply increases with the beginning of the fog and it keeps up these high values during the entire episode. As seen, in both interruptions the CSSI decreases but only locally. When the foggy episode ends our index drops. The observed course of CSSI is completely in accordance with our finding that fogs require as a whole higher values of our stability index.

Summary

The objective of our paper was to study the fogs in Sofia, Bulgaria by means of a specific index of stability which we offer. The standard synoptic observations from meteorological stations Sofia, Mladost and Cherni vrah for the period 01/01/1992-01/12/2014 are used for this purpose. Based on the conception of Brunt-Väisälä's frequency, our stability index CSSI measures the strength of the static stability of the atmosphere layer over Sofia. The index depends only on the surface air temperatures in Sofia and Cherni vrah.

We establish a downward trend of CSSI up to 20-30 km horizontal visibilities. The statistical tests we perform clearly show that the fogs and mists with visibility up to 1000 m require as a whole higher values of CSSI compared to cases without fog. Sample medians

for the groups of fogs or mists with visibility up to 1000 m and all other cases without fog are 0.9834 and 0.6943 respectively. Additionally, we verify our general conclusion by analysing a typical for Sofia fog episode in more detail.

What is the potential prognostic significance of CSSI? If the forecast presumes an occurrence or retention of already formed fog one can calculate CSSI by means of forecasted temperature at Sofia and Cherni vrah. A trend to higher values of CSSI additionally favours the fog occurrence or continuation. In contrast, a trend towards lower CSSI reduces the chance of the fog.

References

- Belinskii, B.A., 1948. Dynamic Meteorology, OGIZ, Gostehizdat, Moscow, St. Petersburg (in Russian).
- Croitoru, A.-E., Holobacă, I.-H., Rus, I., Mureşan, T., 2011. Multivariate statistical analysis of fog phenomenon in Northwestern Romania, *Geographia Technica*, No. 1, pp. 9-19.
- Dejmal K., and Novotny, J., 2011. Application of Fog Stability Index for significantly reduced visibility forecasting in the Czech Republic, *Recent Advances in Fluid Mechanics and Heat & Mass Transfer*, ISBN: 978-1-61804-026-8.
- Haines, D.A., 1988. A lower atmospheric severity index for wildland fire, *National Weather Digest*, Vol 13, No. 2:23-27.
- Holtslag, M.C., G.J. Steeneveld G. J., Holtslag A. A. M., 2010. Fog forecasting: “old fashioned” semi-empirical methods from radio sounding observations versus “modern” numerical models, In: *Proceedings of the 5th International Conference on Fog, Fog Collection and Dew, 5th International Conference on Fog, Fog Collection and Dew, 25-30 July 2010, Münster, Germany, 2010-07-25/ 2010-07-30*.
- Godev, N. and K. Takev, 1968. Forecasting the night decrease of temperature in Sofia plain in an anticyclonic condition, *Hydrology and Meteorology*, XVII, 1, pp. 15-24 (in Bulgarian).
- Holton, J.R. *An Introduction to Dynamic Meteorology*, Academic Press, New York, 1972, pp. 319.
- Maier, F., Bendix, J., and Thies, B., 2013. Development and application of a method for the objective differentiation of fog life cycle phases. *Tellus B: Chemical and Physical Meteorology*, 65, 19971, <http://dx.doi.org/10.3402/tellusb.v65i0.19971>.
- Pinheiro F.R., Peterson R.G., De Farias W.C.M., 2006. Numerical study of fog events along Rio De Janeiro Coast, Using The Mm5 Model Coupled With The Unidimensional Model Cobel, *Proceedings of 8 ICSHMO, Foz do Iguaçu, Brazil, April 24-28, INPE*, pp. 1935-1944.
- Robasky, F.M., and F.W. Wilson, 2006. Statistical forecasting of northeast ceiling and visibility using standard weather observations, *12th Conference on Aviation, Range, and Aerospace Meteorology*, Atlanta, GA.
- Wilks, D.S., 2006. *Statistical methods in the atmospheric sciences*, Dep. Earth and Atmos. Sci., Cornell University, United States.
- Zverev, A.C., 1957. *Synoptic Meteorology*, Hydrometeoizdat, St. Petersburg (in Russian).

Изучаване на мъглата в София чрез индекс на устойчивост Черни връх-София

А. Стойчева, С. Евтимов

Резюме: В настоящата работа е проведено изучаване на мъглата в София чрез предложен от авторите индекс на устойчивост Черни връх-София. Отчитайки степента на статична устойчивост на атмосферния слой над София, този индекс зависи само от две температури – приземната температура в синоптична станция София, Младост и температурата във високопланинската обсерватория Черни връх, което го прави полезен за оперативната практика. Чрез използване на данните от стандартните синоптични наблюдения в посочените метеорологични станции за периода 01/01/1992-01/12/2014, е установена статистическа връзка между стойностите на индекса и хоризонталната видимост в София. Статистически достоверно е намерено, че мъглите в София се реализират при по-високите стойности на Индекса, докато добрата видимост съответства на по-ниските такива. Тази връзка е проверена и при една типична за възникване на мъгла в София синоптична обстановка.

LIDAR REGISTRATION OF THE VERTICAL STRATIFICATION OF SAHARAN DUST INCURSIONS OVER SOFIA

A. Deleva

Institute of Electronics, 72 Tsarigradsko Chaussee Blvd., 1784 Sofia, Bulgaria, e-mail:
adeleva@ie.bas.bg

Abstract. Atmospheric particles (aerosols) and mainly mineral dust particles affect life on Earth in several ways. Key parameters for determining the impacts of aerosols to climate forcing and the ecological state of the environment are their optical parameters (backscatter and extinction coefficients), as well as their spatial distribution. In this study, the results are analyzed of the vertical remote sounding of several Saharan dust outbreaks above Sofia. The investigations were carried out by a aerosol LIDAR (*L*ight *D*etection *A*nd *R*anging) based on a Nd:YAG laser. The examples presented illustrate that the detected aerosol/dust layers differ in their altitude, density, thickness and height stratification. Some of the results show that aerosols can reach up to and persist in the unusual 14 km altitude region in the troposphere. Experimental data are presented in terms of atmospheric backscatter coefficient profiles and 2D-color maps of the aerosol stratification time evolution. The DREAM (*D*ust *R*EGional Atmospheric Model) forecasts and HYSPLIT (*H*ybrid *S*ingle-Particle *L*agrangian *I*ntegrated *T*rajectory) backward trajectories for the days of measurements were employed to draw conclusions about the atmospheric aerosol's origin.

Key words: lidar, atmospheric aerosols, Saharan dust, troposphere.

Introduction

Dust plumes, both of natural and anthropogenic origin, frequently cover huge areas of the Earth and represent one of the most prominent and commonly visible features in satellite imagery (Yoram J. Kaufman et al., 2002). Dust (mineral aerosols) is one of the major components of the atmospheric aerosol loading (Duce, R., 1995; Maria Raffaella Vuolo et al., 2009; Ina Tegen, 2003). The main sources of dust are the large arid areas of the world. Dust is transported in suspension at a wide range of heights above the surface and can rapidly cover considerable distances. Like all aerosol types, dust particles can alter

the Earth radiation budget directly by scattering and absorption or indirectly by modifying the formation and properties of clouds (J. E. Penner et al., 2001; Natalie M. Mahowald et al., 2003; U. Pöschl, 2005; R. L. Miller and I. Tegen, 1998). Also, they affect the air quality, reduce visibility, and pose risks to human health (Perez L. et al., 2008; U. Pöschl, 2005). These effects of dust/aerosols on the environment strongly depend on their optical properties, altitude of location in the atmosphere and the vertical repartition of the particles (E. Hamonou et al., 1999; P. Kishcha, 2005; F. Immler and O. Schrems, 2003; Gian Paolo Gobbi et al. 2000; De Tomasi F. et al., 2003). The latter is transport dependent. Indeed, during the transport the vertical structure may be modified by mechanisms such as convective erosion of the dust layer and gravitational setting of particles.

North Africa, especially Sahara desert, is the largest source of dust of natural origin (Prospero M. Joseph, 1999; Vukmirović Z. M. et al., 2004). The desert aerosols captured by the wind at the surface are raised to considerable altitudes by the strong convective processes that develop over the desert and, under certain weather conditions, they can reach the European, Asian and American continents (Albert Ansmann et al., 2003; Albert Ansmann et al., 2009; Joseph M. Prospero, 1999; A.S. Goudie, 2001; Alpert P., 1993; Yoram J. Kaufman, 2005; J. Barkan, 2008; Chiapello J., 1997). The Mediterranean region, and particularly the Balkan Peninsula, have been under the influence of Saharan dust transport and deposition over millennia. Every year huge amounts [200-500 million tons (De Tomasi F. et al., 2003; Mitsakou C., 2008)] of Saharan dust are transported over the Mediterranean Sea to most of Europe.

In recent years, a number of studies have been focused on understanding the different phases of the Saharan dust process (mobilization, transport, deposition and climate interactions) over Europe based on lidar monitoring, in situ measurements, satellite imaging; these have often been organized as observational networks (L. Mona, 2012; I. Mattis, 2008).

The lidar techniques for atmospheric studies are recognized as the most powerful tools for investigating the vertical structure of the atmosphere through its major advantage of real-time observation with high resolution both in time and space. Lidars have attained a high degree of reliability and have been used by regional networks to produce long-term and well-calibrated measurements of aerosol properties. These include the European Aerosol Research Lidar Network (EARLINET), a federation of 27 European lidar research groups (<http://www.earlinet.org>). The aim of EARLINET is to establish a quantitative data base of both horizontal and vertical distributions of aerosols on a continental scale. Systematic observations of Saharan dust transport events over Europe began in May 2000 by EARLINET (A. Papayanis, 2005; A. Papayanis, 2009; Papayannis A., 2008).

The only lidar station in Bulgaria is located in the Laser Radar Laboratory of the Institute of Electronics of the Bulgarian Academy of Sciences. Since March 2003, it has been involved in systematic measurements on a regular basis – three times per week according to the schedule of the EARLINET. When Saharan dust presence is forecast, more observations are conducted in view of obtaining as full as possible an image of the Saharan dust transport event.

Lidar measurements described below are obtained within the frame of the EARLINET. A large database is created accumulating the aerosol backscatter profiles which are uploaded on the common EARLINET-server in Germany.

In this study we present some results selected from the regular lidar investigations of the atmosphere. The backscatter profiles and height-time color maps included illustrate laser remote observations on the vertical mass distribution of relatively stable aerosol layers situated at different altitudes. The lidar measurements were conducted on Saharan-dust-affected days; we therefore infer that desert dust loadings in the air above Sofia were detected.

Equipment and data processing

The results presented in this paper are based on measurements by an aerosol elastic backscatter lidar located in the Laser Radar Laboratory, IE-BAS (A. Deleva, 2010; Atanaska D. Deleva, 2008). It is configured in a mono-static biaxial alignment pointing at a maximum slope angle of 32° with respect to the horizon, as determined by its position in the lab. Thus, despite that signals from as far as a 30-km distance are recorded, the maximum sounding height is limited to 16.4 km.

The lidar transmitter is based on a high-power Nd:YAG laser providing output pulse energy of up to 600 mJ at 1064 nm and 80 mJ at 532 nm, with a pulse duration of 15 ns FWHM at a repetition rate of 2 Hz. The laser beam divergence is 2.2 mrad. The receiver's optical part consists of a Cassegrain-type telescope (aperture 35 cm; focal distance 200 cm) and a spectrum-analyzer based on narrowband interference filters (1-3 nm FWHM). The electronic part of the lidar receiving system is formed by compact photo-electronic modules, each comprising a photo-detector, a 10-MHz 14-bit analog-to-digital converter (ADC), a high-voltage power supply, and controlling electronics. The receiving modules are connected to a PC via high-speed USB ports. The received signals are digitized every 100 ns by an ADC, resulting in a 15-m range resolution (about a 7.5-m altitude resolution). Thus, the lidar measures the temporal evolution of the atmospheric aerosol backscatter with high time and range resolutions. The acquisition system is equipped with specialized software for accumulation, storage, and processing of lidar data. The vertical atmospheric backscatter coefficient profiles are retrieved using the Klett-Fernald inversion algorithm (J. D. Klett, 1981; F. G. Fernald, 1984). Since the magnitude of the backscatter coefficient value is proportional to the aerosol density, the changes in the calculated lidar profiles in time and space illustrate the temporal evolution and the stratification of the aerosol field observed. Usually, each lidar measurement lasts for 1-3 hours. The lidar signal is accumulated for 5-10 min (corresponding to data accumulation of 600-1200 different raw profiles received at each laser pulse). The parameters of the laser, telescope, photo-receiving modules and software make it possible for the lidar to be utilized for carrying out fast remote measurements of the atmosphere from 130 m above ground level (AGL) (approximately 700 m above sea level, ASL) to the tropopause.

To draw conclusions about the type and origin of the aerosol layers detected by the lidar, we use additional information provided by DREAM-forecast maps of dust load and concentration in the atmosphere for the Euro-Mediterranean zone. Such maps are prepared by the Forecast system of Barcelona Supercomputing Center, Spain, and are accessible via Internet (<http://www.bsc.es/projects/earthscience/DREAM/>). DREAM-maps give an image of the wind direction and magnitude of dust load in the atmosphere above North Africa and

Europe. An additional source of information about the origin of the aerosol layers is offered by the HYSPLIT model (Draxler R. R., 2010; Rolph G. D., 2011). It can be run interactively on the web through the READY system on the site of the Air Resource Laboratory of NOAA (National Oceanic and Atmospheric Administration), USA. The calculations of backward air mass trajectories yield a plot of the path that the air mass travelled for a chosen time period before arriving at the lidar station.

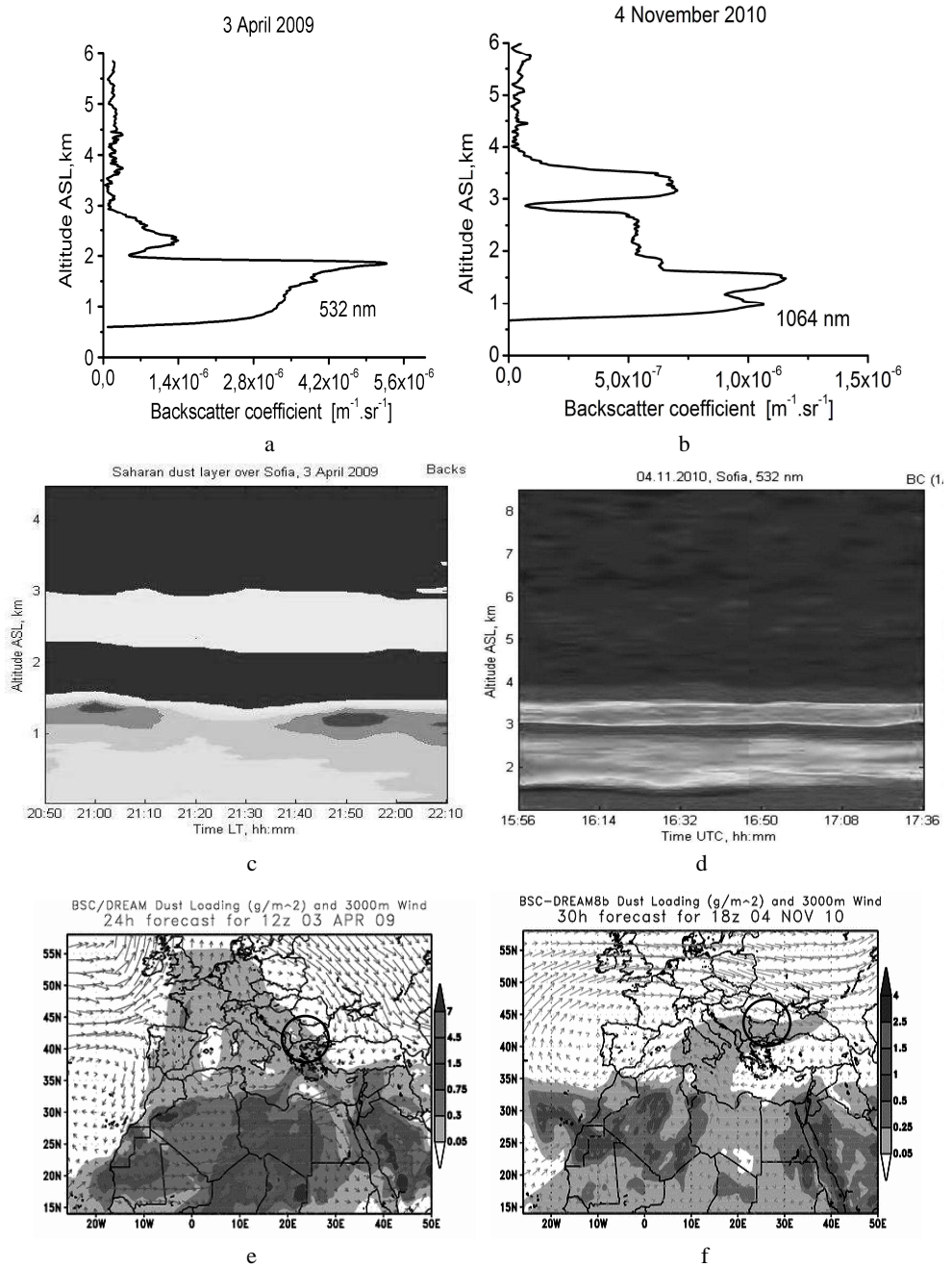
Experimental data and comments

Using the lidar described above, studies of the atmosphere over Sofia during Saharan dust incursions have been conducted for more than ten years. A large data base was acquired, systematized and analyzed. The results demonstrated that Saharan dust can be present within the entire troposphere, with the separate incursion events differing in the height of dust transport, the vertical mass distribution, as well as in the frequency of observation of events with similar spatial stratification. The following basic conclusions were drawn: 1). Saharan dust was most often detected over Sofia to a height of 5-6 km, with the dust aerosol being found either within a distinct layer above the atmospheric boundary layer (ABL), or having penetrated the ABL from the ground up to the height quoted. 2). Very seldom, Saharan dust was transported simultaneously in two separate layers above the ABL, or within the entire troposphere to the extreme heights of 12-14 km. These conclusions will be illustrated by the lidar experiments described below.

We present the results mainly in terms of vertical atmospheric backscatter coefficient profiles (the x -axis representing the value of the calculated atmospheric backscatter coefficient; the y -axis, the altitude. The measurement date and the sounding laser wavelength are cited over the respective lidar profile plot. Also, 2D-colormaps of the aerosol stratification time evolution are constructed for some separate measurements (the x -axis representing the time interval of the measurement; the y -axis, the altitude). For each of the experiments, a DREAM-map is enclosed demonstrating that the Barcelona Supercomputing Center has forecast a Saharan dust transport over Bulgaria, whose location is indicated by a black circle. It should be noted that the HYSPLIT model allows one to depict up to three trajectories on a single map. This is why, of all trajectories calculated for the time interval of a particular measurement, on the respective HYSPLIT map we include those three of them that end over Sofia at heights falling within characteristic sections of the recovered atmospheric backscatter coefficient profile. Such a choice assists one in explaining the results. As was mentioned above, the information provided by the DREAM and HYSPLIT is used to draw conclusions concerning the origin of the particles in the aerosol layers registered. However, when drawing such a conclusion, one should always bear in mind that, since aerosols are transported over long distances in the atmosphere, mixing between aerosol populations from different source regions and with different composition can take place (for example, mixing between desert dust, continental aerosols and maritime particles). Thus, the particles detected by the lidar are the final result of the mixture of Saharan dust with different types of aerosols, partially coated by water.

As examples of observing Saharan dust in a distinct layer above the ABL, we describe in more detail the experiments performed on April 3, 2009, and November 4, 2010

(Fig. 1). For these dates, the DREAM model has forecast dust transport over Bulgaria (Sofia) (Fig.1 e, f).



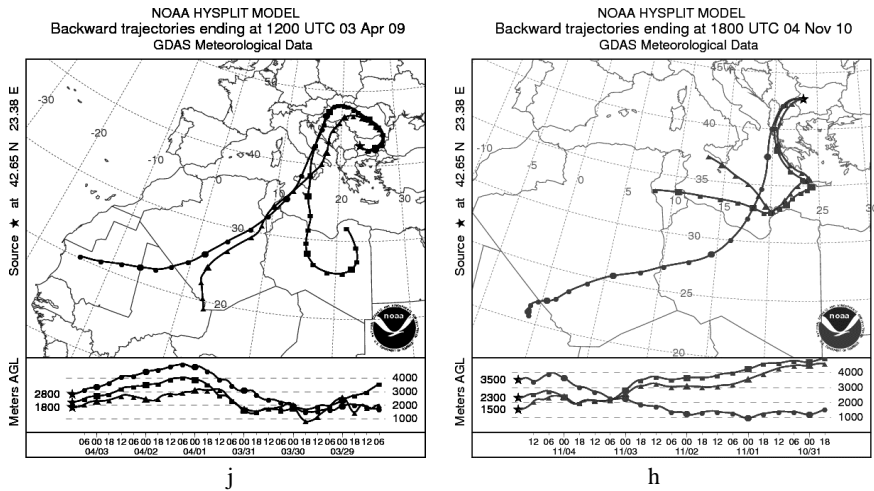


Fig.1. Lidar observations of Saharan dust above Sofia on April 3, 2009 and November 4, 2010: a, b). retrieved vertical atmospheric backscatter coefficient profiles; c, d). time evolution maps of the mass spatial distribution; e, f). DREAM forecast maps showing Saharan dust transport over Bulgaria; g, h). HYSPLIT model backward trajectories.

The lidar profile (Fig.1 a) and the 2D-map (Fig.1 c) show that the layer above the ABL, registered on April 3, 2009, was located within the height interval of 2-3 km with a mass center at about 2.5 km. Further, the profile curve reveals an atypical increase with the height of the aerosol concentration in the ABL, with a maximal value at a height of about 1.8 km. The HYSPLIT backward trajectories calculated for the height range of 1.5-3 km, three of which are presented in Fig.1.j, reveal that, before reaching Sofia, the air masses in this range have moved low above the surface of Sahara (North Africa) and passed through the heavily dusted space over the Mediterranean Sea, as seen in the DREAM map. Fig.1.j presents the trajectories terminating above Sofia at the heights of 1.8, 2.2 and 2.8 km. These were selected purposefully, since their ends coincide with characteristic regions in the curve of the retrieved lidar profile of the atmospheric backscatter coefficient. In this particular case, at the height of 1.8 km we determined the highest atmospheric backscatter coefficient value, while the heights of 2.2 and 2.8 km are the lower and the higher boundaries of the layer above the ABL. We thus concluded that the aerosol layer within the range 2-3 km contained mainly Saharan dust. We further assumed the presence of large amount of Saharan dust in the ABL is the cause of the anomalous increase with the height of the aerosol mass concentration, its largest value being at 1.8 km.

The lidar data acquired on November 4, 2010, are presented in Fig.1.b,d. One can see that a temporally stable layer was detected above the ABL, with the center of mass near a height 3.5 km and well delineated boundaries at 3 km and 4 km. One can also see that in the ABL the aerosol concentration was maximal at 1.5 km, while further up to about 3 km it varies negligibly. The calculated HYSPLIT trajectories, which during the measurements terminated in the 2.8-4.3 km range, have started much farther south over Sahara and passed through vast dusted spaces before reaching Sofia. Fig.1 h presents the one ending at 3.5 km, where the center of mass of the layer above the ABL was. The black-and-white image in

the HYSPLIT map necessitates the explanation that this is the trajectory beginning over Sahara and passing for a considerable distance at a height of about 1 km above the desert surface. The calculated HYSPLIT trajectories below 2.8 km originate and traverse a dusted space over the Mediterranean Sea. Of these, the map shows the ones that end above Sofia at the heights of 1.5 km and 2.3 km, thus falling in the above-mentioned specific sections of the lidar profile below 3 km. The main conclusion pointed to by the experimental data is that the aerosols detected in the 3–4 km range were trans-boundary transport of Saharan dust. The lower calculated trajectories give is reason to assume that desert dust was also present in the ABL, where it was mixed with anthropogenic aerosols generated in the city. Judging from the curve of the lidar profile shown, the aerosol pollution of the air above Sofia was the largest at heights of 1–1.5 km.

We will now briefly present another example of detection of a distinct Saharan dust layer above the ABL (Fig.2). The monitoring was carried out on June 28, 2012. On the time-height map (Fig.2 a), constructed from a series of 26 lidar profiles, one can see a dense thin aerosol layer with boundaries at about 4.5 and 5 km. These heights remained unchanged during the monitoring, so that the lack can be assumed of dynamic processes in the atmosphere during the experiment. The analysis of the calculated HYSPLIT trajectories strongly suggest that the aerosol layer registered is the result of a direct transfer of dust from Sahara. The trajectories in Fig.2 b show that the air masses above Sofia in the 4.3–6 km during the experiment originate from Sahara. Special attention should be paid to the trajectories that terminate over Sofia at 5 и 6 km, since five days before these have started immediately above the desert surface (the two trajectories on the right-hand side of the map).

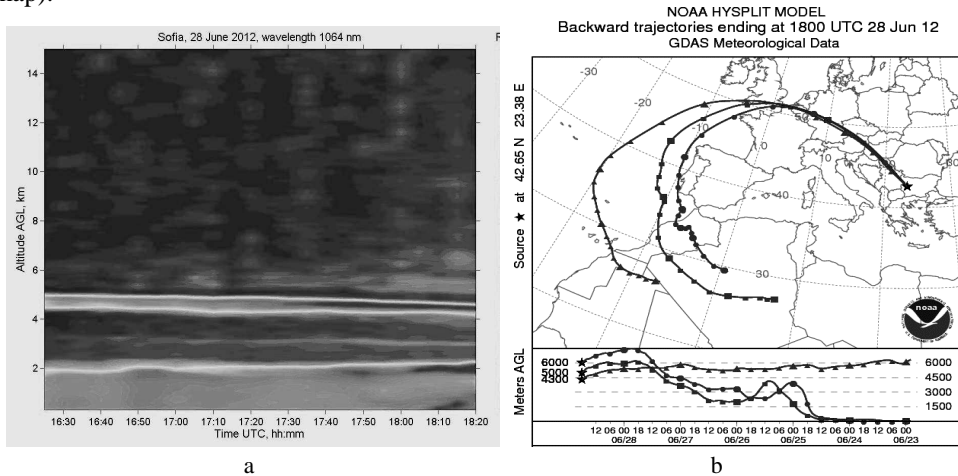
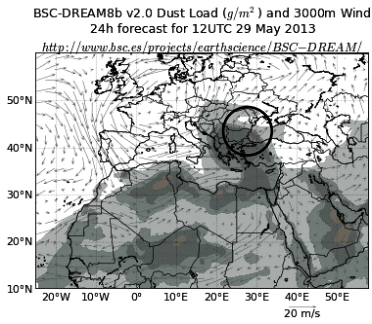


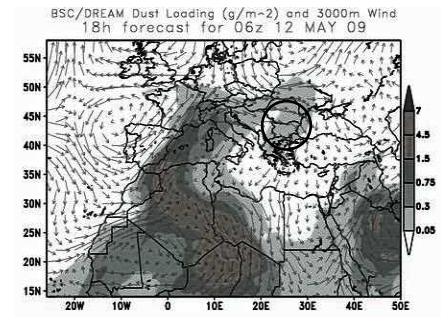
Fig.2. Lidar observations of Saharan dust above Sofia on June 28, 2012: a). time evolution maps of the mass spatial distribution; b). HYSPLIT model backward trajectories.

In contrast with the observations described above, the lidar data in Fig.3 and Fig.4 illustrate Saharan dust transport within a wider layer. The data further demonstrate that the separate transport events are characterized by individual specific vertical mass stratification. This is exemplified by the results obtained on May 29, 2013, and May 12, 2009, and presented below (Fig.3 a, b).



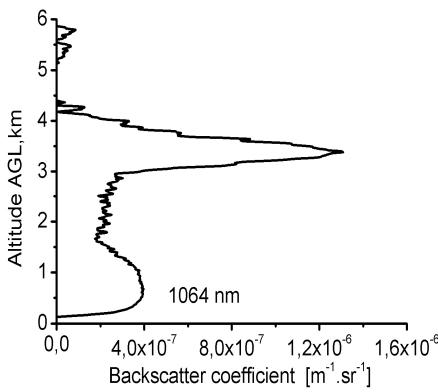
a

29 May 2013

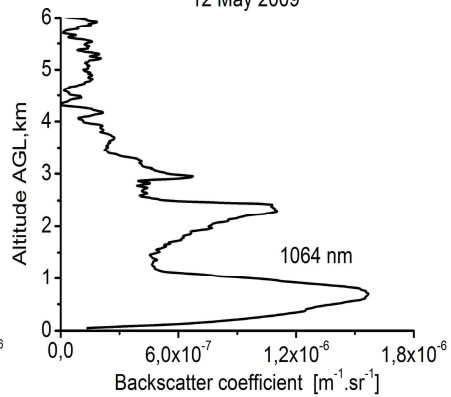


b

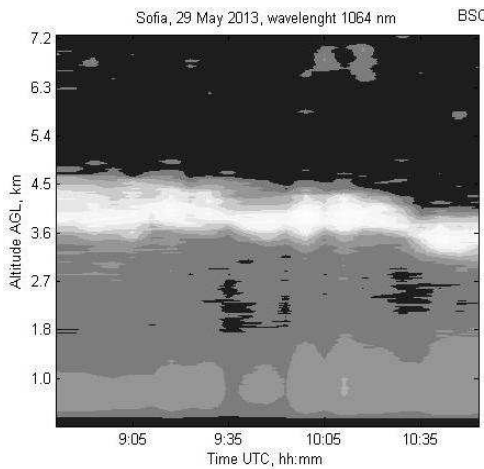
12 May 2009



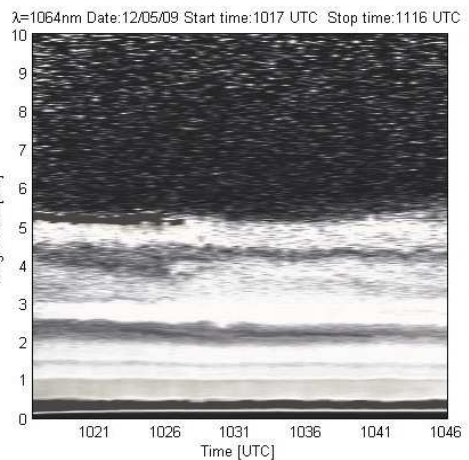
c



d



e



f

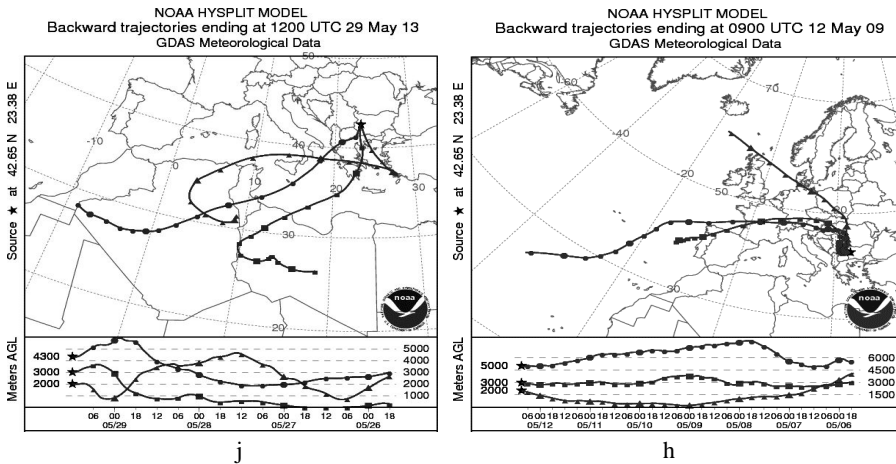


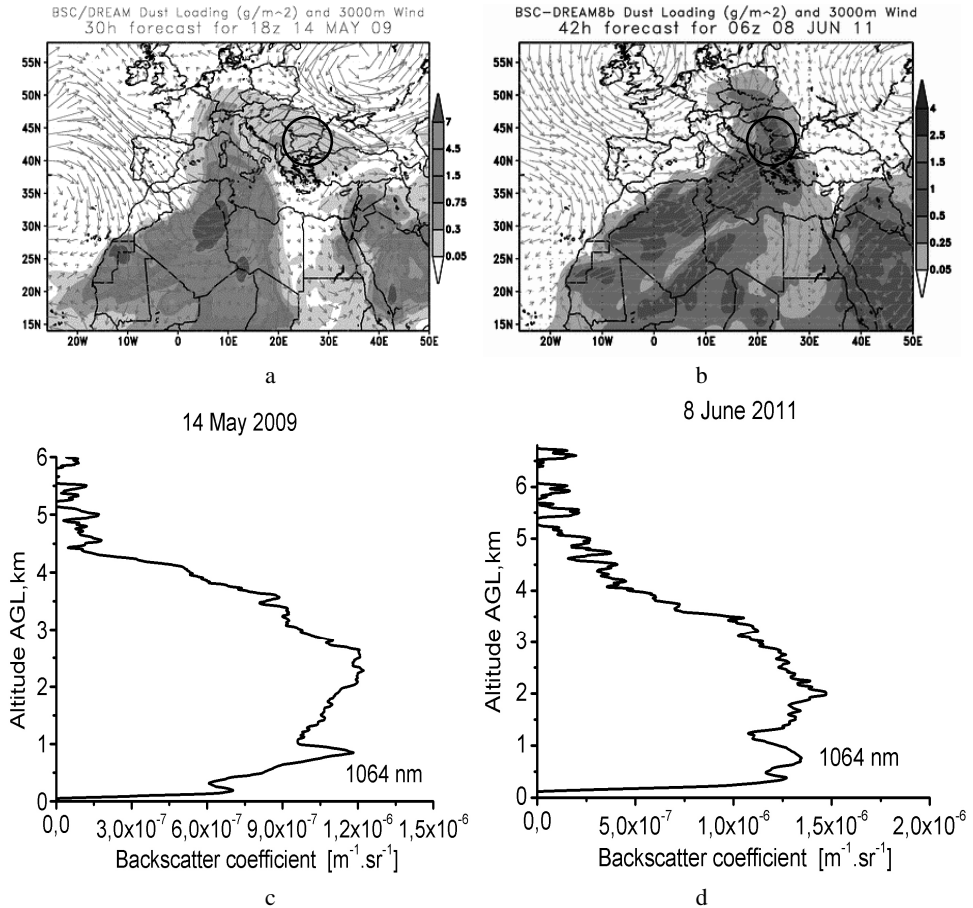
Fig.3. Lidar observations of Saharan dust above Sofia on May 12, 2009 and May 29, 2013: a, b). DREAM forecasts showing Saharan dust transport over Bulgaria; c, d). retrieved vertical atmospheric backscatter coefficient profiles; e, f). time evolution maps of the mass spatial distribution; j, h). HYSPLIT model backward trajectories.

The profile curves (Fig.3.c, d) and the time-height maps (Fig.3.e, f) show that in both cases aerosols were registered above the ABL, up to heights of 4.5 and 5.5 km, respectively. On May, 2013, a dense aerosol layer was present with boundaries at about 3 and 4.5 km and a well-expressed center of mass at 3.5 km. Below this layer, the aerosol concentration was smoothly decreasing down to 1.6 km, after which the lidar profile followed the typical aerosol distribution in the ABL. This mass stratification from the ground up to 4.5 km is revealed better by the profile, since the black-and-white image in the map (Fig.3.e) hinders strongly the presentation of the finer graphical details. The calculated HYSPLIT trajectories, which during the measurements ended in the 2-5 km range of heights, originated above Sahara surface. Fig.3.j presents those that terminated at heights of 2, 3 and 4.3 km above Sofia. The trajectory starting in western Sahara, whose path has passed a long distance immediately above the surface, presents the route of the air masses above the lidar station at about 3 km, where the layer's center of mass was determined. These facts led us to the conclusion that the aerosol detected in the 2-4.5 km range of heights was dust transferred directly from the space above Sahara desert, with the predominant part of its mass being concentrated in a layer with boundaries at 3 и 4.5 km.

An example for Saharan dust indirectly transported to Bulgaria is presented by the results obtained on May 12, 2009. The lidar profile (Fig.3.d) and the 2D map (Fig.3.f) show the existence of aerosols up to 5.5 km above Sofia. One can also see a well-expressed inhomogeneous vertical stratification of the particles concentration, namely, it was larger at heights of about 2, 3 and 5 km. In contrast with the case described above, none of the HYSPLIT trajectories calculated for May 12, 2009 started and passed over North Africa prior to this measurement (Fig.3.h). However, their paths cross a dense cloud of Saharan dust located above vast regions of Europe (Fig.3.b). Due to this complex aerosol condition of the atmosphere over Europe, one can assume that the lidar data included here (Fig.3.d

and Fig.3.f) represent aerosols of different origin, but among them there certainly was a considerable amount of Saharan dust particles.

Fig. 4 includes lidar results (Fig.4.c, d) acquired on May 14, 2009, and June 8, 2011, in order to visualize the events of Saharan dust transport most often detected, namely, when the transport takes place within the entire space from the ground up to a height of 5-6 km, while the aerosol concentration varies insignificantly with the height. The monitoring of May 14, 2009, was chosen because it was conducted just two days following the one of May 12, 2009, and described above. Undoubtedly, the difference between the lidar data (Fig.3.d and Fig.4.c) and the HYSPLIT trajectories included (Fig. 3.h and Fig.4.e) for the two days is due to the continuous dynamic changes of the atmosphere, this being its basic property.



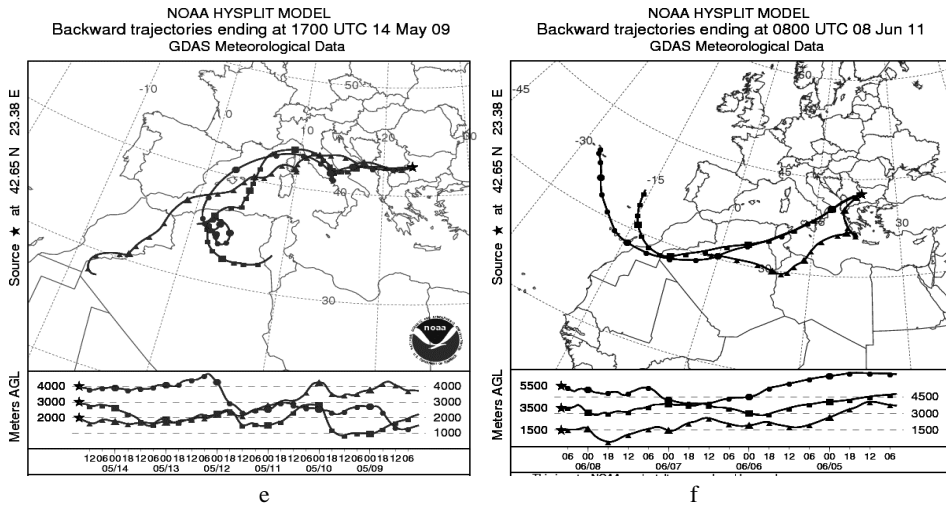


Fig.4. Lidar registrations of Saharan dust above Sofia on May 14, 2009 and June 8, 2011: a, b). DREAM forecasts showing Saharan dust transport over Bulgaria; c, d). retrieved vertical atmospheric backscatter coefficient profiles; e, f). HYSPLIT model backward trajectories.

The results of the lidar measurements performed on May 14, 2009, and on June 8, 2011, do not differ significantly. During these two days, the aerosol load had a higher boundary at about 5 km, the center of mass was roughly at 2-2.5 km, the concentration of particles above it gradually decreased with the height, and the border with the ABL was expressed weakly. The corresponding DREAM maps (Fig.4.a, b) show that dense Saharan dust covered Bulgaria's territory. For the days of measurement, the HYSPLIT backward trajectories were calculated in the height range of 1.5-5.5 km. It is not necessary to describe them in detail, because it is obvious that they pass over Northern Africa/Sahara desert and across the highly dusted space over Mediterranean Sea before the end point above Sofia (Fig.4.e, f). This is the reason why we assume to suppose that the air masses in the range 1.5-5.5 km during the measurements were desert aerosols transported to a long distance from North Africa.

The next results demonstrate that Saharan dust can be transported simultaneously in two separate layers located above the ABL (Fig.5), or through the entire troposphere up to the tropopause (Fig.6). As we already noted, such transport events are detected very rarely.

The data acquired on June 29, 2006 are presented in Fig.5. On this day, a dense dust cloud was located in the atmosphere over North Africa and Europe (Fig.5.c). The lidar data (Fig.5.a and Fig.5.b) indicate the existence of aerosols over Sofia up to a height of 4.5-5 km. The lidar profile shows that they were distributed mainly in the ABL up to 1 km, and in two layers above the ABL in the 1-2 km and 3-5 km ranges. In the first two ranges, the particles concentration was the highest at about 0.5 km and 1.5 km, while in the top layer the concentration was lower and did not vary significantly with the height.

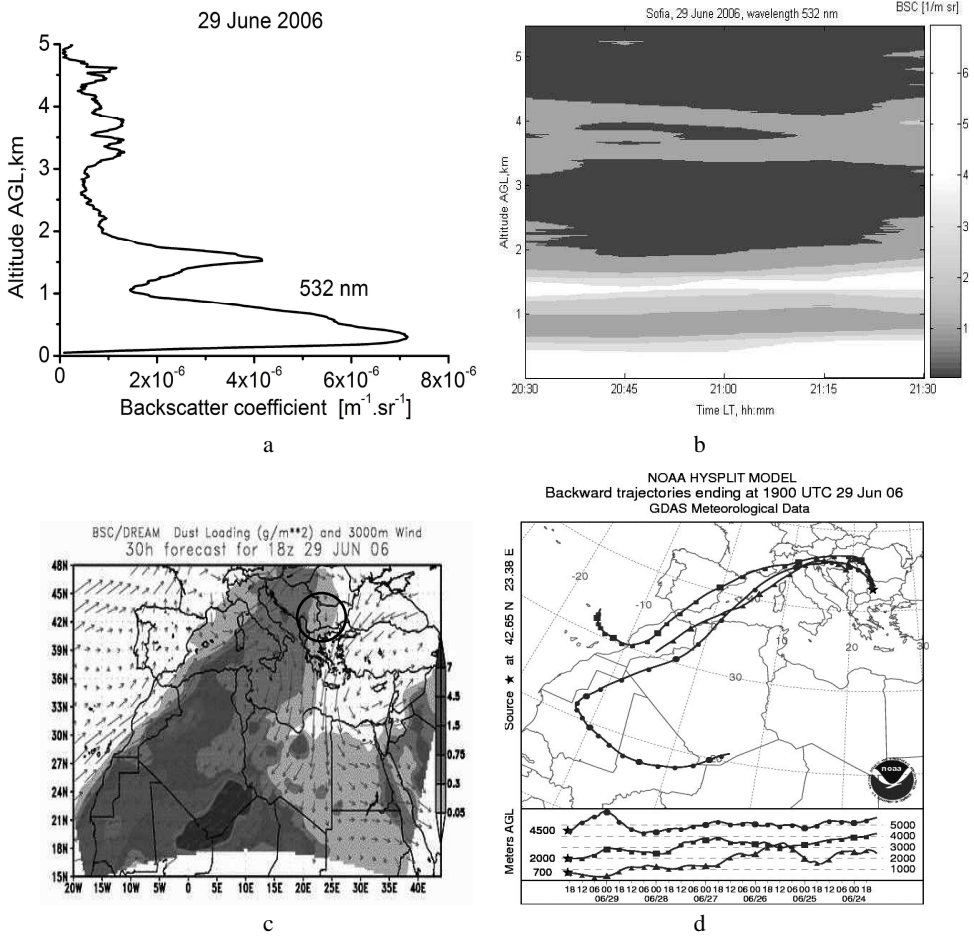


Fig.5. Lidar monitoring of Saharan dust above Sofia on June 29, 2006: a). retrieved vertical atmospheric backscatter coefficient profile; b). the time evolution map of the mass spatial distribution; c). DREAM map showing Saharan dust transport over Bulgaria; d). HYSPLIT backward trajectories.

The HYSPLIT trajectories calculated for the 0.5-5 range reveal that the air masses above Sofia up to 5 km have crossed dusted atmosphere over North Africa, the Mediterranean Sea and Europe. Fig.5.d. shows three of those, with end points above the city at 0.7, 2 and 4.5 km. The one originating the farthest in the southern part of Sahara ended during the measurements at 4.5 km above Sofia; the one starting further to the west, at 0.7 km; and the third one, at 2 km. Our analysis led us to believe that the aerosol loading of the air above Sofia from the ground to a height of 5 km was in this case the result of a direct transfer of desert dust from North Africa; in the free troposphere it was transported simultaneously in two separate layers.

We will finally describe the results obtained during the monitoring conducted on April 15, 2009, (Fig.6), when we observed a unique event of aerosol loading of the free

troposphere up to 12-14 km.

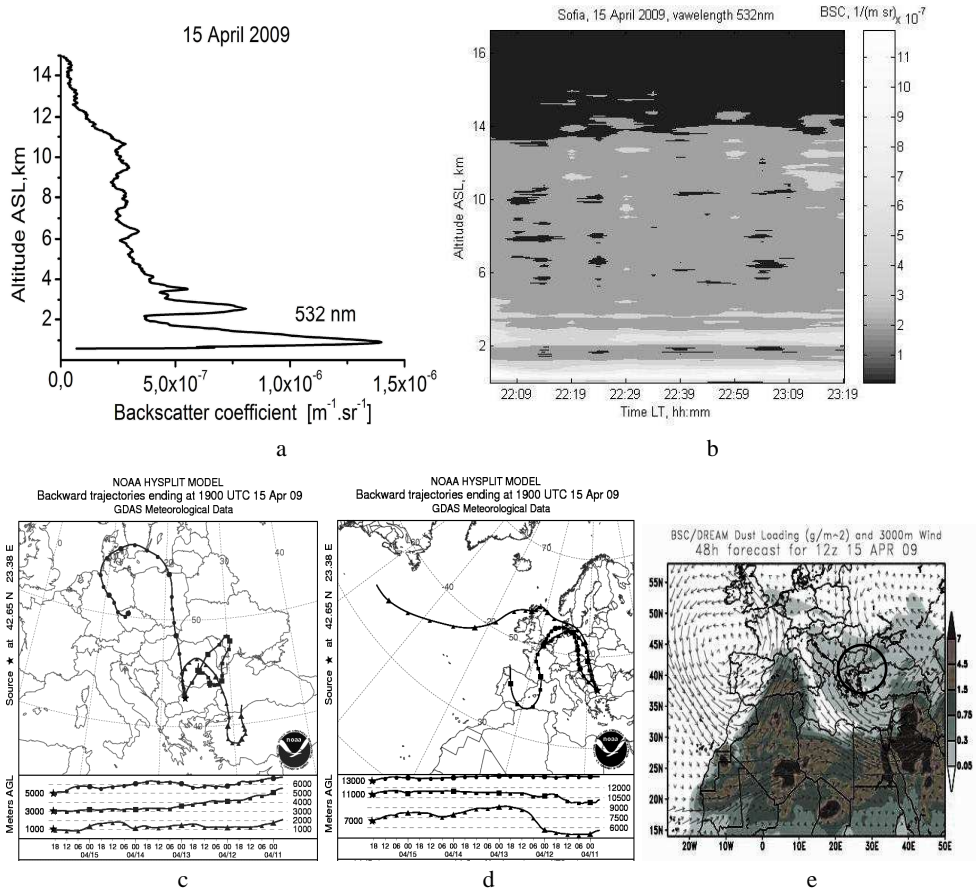


Fig.6. Lidar monitoring of Saharan dust above Sofia on April 15, 2009: a). retrieved vertical atmospheric backscatter coefficient profile; b). the time evolution map of the mass spatial distribution; c,d). HYSPLIT-backward trajectories; e). DREAM forecast map of Saharan dust transport.

Specific features of the mass stratification of the aerosol layer in the free troposphere (Fig.6.a, b) are its well-expressed lower boundary with the ABL at a height of 2 km, a higher particles concentration at heights 2.5-3 km (a well-expressed center of mass), after which the concentration falls smoothly up to about 6 km; it varies weakly further up to 11 km, after which it decreases again up to a height of 14 km. This extraordinary aerosol loading as a function of the height necessitated that we calculate and analyze HYSPLIT backward trajectories within the entire troposphere. Some of these, up to 5 km, are presented in Fig.6.c, while some in the range of 7-13 km, in Fig.6.d. The trajectories included demonstrate that no air masses have reached Sofia directly from the space above North Africa. However, all air masses have moved over regions where the atmosphere has been loaded with Saharan dust (Fig.6.e).

Among the trajectories presented in Fig.6.c, we should single out the one originating from the most heavily dusted south-western territories and having an almost horizontal path over the ground until reaching its end point above Sofia. It describes the motion of the air masses that during the measurements were present in the ABL at a height of 1 km, and where, according to the lidar profile curve, the aerosol concentration was the highest. Such a trajectory path gave us reason to assume that a considerable amount of Saharan dust, mixed with the usual aerosols generated in the city, was present in the ABL above Sofia. A brief clarification is needed here concerning the trajectories in Fig.6.d. The one starting low above the Atlantic Ocean ended over Sofia at a height of 7 km. The other ones originated from and passed through strongly dusted atmosphere above Europe, especially the one which at one point reaches South-West Africa. Thus, assisted by the information provided by the HYSPLIT and DREAM models, we believe that on April 15, 2009, we registered a unique in terms of its height (up to 12-14 km) aerosol loading of the atmosphere over Sofia, which was mainly due to Saharan dust transported to the Balkans from dusted regions over Europe.

Conclusions

We reported on several lidar investigations of atmospheric aerosol loading during Saharan dust intrusions over Sofia. These sounding examples were selected among data systematically acquired within the EARLINET projects. Aerosol layers related to desert dust were observed in the whole troposphere up to a height of 14 km. The lidar observations revealed a multilayering of the dust transport. The internal structure of the dust plumes registered varied from homogenous to well-stratified.

We should further emphasize that the results reported here not only illustrate the exceptional possibilities offered by lidars concerning remote sounding of the atmosphere, but also the good technical performance of our lidar system, which permits us to observe the whole troposphere with high spatial and temporal resolutions.

Acknowledgments. This work is supported by the project of EARLINET ACTRIS-2 (Aerosols, Clouds, and Trace Gases Research Infrastructure Network). The authors gratefully acknowledge the NOAA Air Resources Laboratory (ARL) for the provision of the HYSPLIT model for air mass transport and dispersion and/or READY website used in this publication. The authors would like also to express their gratitude to the Earth Sciences Division, Barcelona Supercomputing Center, Spain, for the provision of the DREAM model aerosol dust data.

References

- A. Papayanis, D. Balis, V. Amiridis, G. Chourdakis, et al., 2005. Measurements of Saharan dust aerosols over the Eastern Mediterranean using elastic backscatter-Raman lidar, spectrophotometric and satellite observations in the frame of the EARLINET project, *Atmospheric Chemistry and Physics*, **5**, 2065-2079.

- A. Papayanis, V. Amiridis, L. Mona, R. E. Mamouri et al., 2009. Coordinated lidar observations of Saharan dust over Europe in the frame of EARLINET_ASOS project during CALIPSO overpasses: a strong dust case study analysis with modelling support, *Proceedings of SPIE*, **7479**, doi: 10.1117/12.830842, 74790C-1 ÷ 74790C-10
- Albert Ansmann, Jens Bösenberg, Anatoli Chaykovsky, Adolfo Comerósabine Eckhardt, Ronaldo Eixmann, Volker Freudenthaler, and Paul Ginoux, 2003. Long-range transport of Saharan dust to northern Europe: The 11-16 October 2001 outbreak observed with EARLINET, *Journal of Geophysical Research*, **108**, AAC1-AAC12.
- Albert Ansmann, Holger Baars, Matthias Tesche, Detlef Müller, Dietrich Althausen et al., 2009. Dust and smoke transport from Africa to South America: Lidar profiling over Cape Verde and the Amazon rainforest, *Geophysical Research Letters*, **36**, L11802, doi: 10.29/2009GL037923
- A.S. Goudie and N.J. Middleton, 2001. Saharan dust storms: nature and consequences, *Earth-Science Reviews*, **56**, 179-204
- Alpert P. and Ganor E., 1993. A jet stream associated heavy dust storm in the eastern Mediterranean, *Journal of Geophysical Research*, **98**, 7339-7349
- A. Deleva, A. Slesar, and S. Denisov, 2010. Investigations of the aerosol fields and clouds in the troposphere with Raman-aerosol lidar, *Bulgarian Geophysical Journal*, **36**, 26-39
- Atanaska D. Deleva, Ivan V. Grigorov, Lachesar A. Avramov, Vladimir A. Mitev, Alexander S. Slesar, and Sergey Denisov, 2008. Raman-elastic-backscatter lidar for observations of tropospheric aerosol, *Proc. SPIE* **7027**, 70270Y-1 ÷ 70270Y-8
- Chiapello J., Bergametti G., Chatetnet B., Bosquet P., Dulac F., Santos Guares E., 1997. Origins of the African dust transported over the northeastern tropical Atlantic, *Journal of Geophysical Research*, **102**, 13701-13709
- Duce, R. 1995. Sources, distributions, and fluxes of mineral aerosols and their relationship to climate, In: *Aerosol Forcing of Climate* (R. J. Charlson and J. Heintzenberg, Eds.), John Wiley, Chichester, U. K., 43–72.
- De Tomasi F., Blanco A., Perrone MR., 2003. Raman monitoring of extinction and backscattering of African dust layers and dust characterization, *Applied Optics*, **42**, 1669-1709
- DREAM: <http://www.bsc.es/projects/earthscience/DREAM/>
- Draxler R. R., and Rolph G. D., 2011. HYSPLIT (HYbrid Single-Particle Lagrangian Integrated Trajectory) Model access via NOAA ARL READY Website (<http://ready.arl.noaa.gov/HYSPLIT.php>). NOAA Air Resources Laboratory, Silver Spring, MD.
- E. Hamonou, P. Chazette, D. Balis, F. Dulac, X. Schneider, E. Galani, G. Ancellet, and A. Papayannis, 1999. Characterization of the vertical structure of Saharan dust export to the Mediterranean basin, *Journal of Geophysical Research*, **104**, D18, 22257-22270
- EARLINET; <http://www.earlinet.org>
- F. Immler and O. Schrems, 2003. Vertical profiles, optical and microphysical properties of Saharan dust layers determined by a ship-borne lidar, *Atmospheric Chemistry and Physics*, **3**, 1353-1364
- F. G. Fernald, 1984. Analysis of atmospheric lidar observations: some comments, *Applied Optics*, **23**, 652-653
- Gian Paolo Gobbi, Francesca Barnaba, Riccardo Giorgi, and Alessandra Santacasa, 2000. Altitude-resolved properties of a Saharan dust event over the Mediterranean, *Atmospheric Environment*, **34**, 5119-5127.
- Ina Tegen, 2003. Modeling the mineral dust aerosol cycle in the climate system, *Quaternary Science Reviews*, **22**, 1821–1834.

- I. Mattis, D. Muller, A. Ansmann, U. Wandinger, J. Preibler, P. Seifert, and M. Tesche, 2008. Ten years of multiwavelength Raman lidar observations of free-tropospheric aerosol layers over central Europe: Geometrical properties and annual cycle, *Journal of Geophysical Research*, **113**, D20202, doi: 10.1029/2007/JD009636
- Joseph M. Prospero, 1999. Long-range transport of mineral dust in the global atmosphere: Impact of African dust on the environment of the southeastern United States, *Proceedings of the National Academy of Sciences of United States of America*, **96**, 3396-3403
- J. Barkan, P. Alpert, 2008. Synoptic patterns associated with dusty and non-dusty seasons in the Sahara, *Theoretical and Applied Climatology*, DOI 10.1007/s00704-007-0354-9
- J. D. Klett, 1981. Stable analytical inversion solution for processing lidar returns, *Applied Optics*, **20**, 211-220
- L. Mona, Z. Liu, D. Muller, A. Omar, A. Papayannis, G. Papalardo, N. Sugimoto, and M. Vaughan, 2012. Lidar measurements for desert dust characterization: An overview, *Advances in Meteorology*, ID 356265, 36 pages, doi: 10.1155/2012/356265
- Maria Raffaella Vuolo, Hélène Chepfer, Laurent Menut, and Gregory Cesana, 2009. Comparison of mineral dust layers vertical structures modeled with CHIMERE-DUST and observed with the CALIOP lidar, *Journal of Geophysical Research*, **114**, D09214, doi:10.1029/2008JD011219
- Mitsakou C., Kallos G., Papantoniou N., Spyrou C., Solomos S., Astitha M., and Housidas C., 2008. Saharan dust levels in Greece and received inhalation doses, *Atmospheric Chemistry and Physics*, **8**, 7181-7192.
- Natalie M. Mahowald, and Lisa M. Kiehl, 2003. Mineral aerosols and cloud interactions, *Geophysical Research Letters*, **30**, 1475, doi:10.1029/2002GL016762
- Perez L., Tobias A., Querol X., Pey J., Künzli N., Pey J., Alastuey A., Viana M., Valero N., González-Cabré M., and Sunyer J., 2008. Coarse particles from Saharan dust and daily mortality, *Epidemiology*, **96**, 800-807
- Papayannis A., Amiridis V., Mona L., Tsaknakis G., Balis D., Bösenberg J., Chaikovskiy A., et al., 2008. Systematic lidar observations of Saharan dust over Europe in the frame of EARLINET (2000-2002), *Journal of Geophysical Research*, **113**, D10204, 2007JD009028
- P. Kishcha, F. Barnaba, G. P. Gobbi, P. Alpert, A. Shtivelman, S. O. Krichak, and J. H. Joseph, 2005. Vertical distribution of Saharan dust over Rome (Italy): Comparison between 3-year predictions and lidar soundings, *Journal of Geophysical Research*, **110**, D06208, doi:10.1029/2004JD005480
- R. L. Miller and I. Tegen, 1998. Climate response to soil dust aerosols. *Journal of Climate*, **11**, 3247-3267
- Rolph G. D., 2011. Real-time Environmental Applications and Display sYstem (READY) Website (<http://ready.arl.noaa.gov>). NOAA Air Resources Laboratory, Silver Spring, MD
- U. Pöschl, 2005. Atmospheric Aerosols: Composition, Transformation, Climate and Health Effects, *Atmospheric chemistry*, **44**, 7522-7540
- Yoram J. Kaufman, Didier Tanré and Olivier Boucher, 2002. A satellite view of aerosols in the climate system, *Nature*, **419**, 215-223, www.nature.com/nature
- Yoram J. Kaufman, Ilan Koren, Lorraine A. Remer, Daniel Rosenfeld, and Yinon Rudich, 2005. The Effect of Smoke, Dust and Pollution Aerosol on Shallow Cloud Development Over the Atlantic Ocean, *Proceedings of the National Academy of Sciences of United States of America*, **102**, 11207-11212

Лидарна регистрация на вертикалната стратификация на Сахарски прах по време на транспорт над София

А. Делева

Резюме: Атмосферните частици (аерозолите) и главно минералният прах въздействат на живота на Земята чрез различни начини. Най-важните параметри за определяне на влиянието на аерозолите върху климата и екологичното състояние на околната среда са техните оптични параметри (коефициент на обратно разсейване и на екстинкция) както и тяхното разпределение в пространството. В тази работа са анализирани резултати, получени от вертикално дистанционно сондиране на атмосферата по време на няколко нахлувания на Сахарски прах над София. Изследванията са направени с аерозолен ЛИДАР (*LIght Detection And Ranging*), базиран на Nd:YAG лазер. Описаните експерименти илюстрират, че регистрираните с лидара аерозолни/прахови слоеве се различават по височина, плътност, дебелина и стратификация по височина. Някои от резултатите показват, че аерозолите могат да достигат и да присъстват в тропосферата до изключителната височина 14 km. В тази работа лидарните данни са представени като изчислени вертикални профили на атмосферния коефициент на обратно разсейване и цветни карти на височинно-временевата еволюция на регистрираните аерозолни полета в атмосферата. При анализа на експерименталните данни са използвани прогнозите на HYSPLIT (HYbrid Single-Particle Lagrangian Integrated Trajectory) и DREAM (Dust REgional Atmospheric Model) моделите за дните на измерванията, за да се направят изводи за произхода на регистрираните аерозоли във въздуха.

LITHOSPHERIC MAGNETIC ANOMALIES IN THE BALKAN REGION

D. Yu. Abramova¹, S.V. Filippov¹, L. M. Abramova², Iv. M. Varentsov²

¹Institute of Terrestrial Magnetism, Ionosphere, and Radio Wave Propagation, Russian Academy of Sciences, Moscow, 142190 Russia, e-mail: abramova@izmiran.ru

²Geoelectromagnetic Research Centre of the Institute of Physics of the Earth, Russian Academy of Sciences, Moscow, 142190 Russia, e-mail: labramova@igemi.troitsk.ru

Abstract. The position of lithospheric magnetic anomalies, detected in total magnetic intensity of the magnetic field, has been determined for Balkan based on the data from the CHAMP satellite and the Global Earth Magnetic Anomaly Grid (EMAG2). The paper describes the technique for the satellite data processing and the ways of separation of regional lithospheric magnetic anomalies from total satellite-measured values of the geomagnetic field. The maps of magnetic field anomalies for two different altitudes have been constructed for the region of Balkan. The possible geologic and physical nature of the magnetic anomalies and their relationship with deep-seated crustal structures are considered. Preliminary interpretation of the magnetic field maps shows that the anomalies are connected with the present day large geologic and geophysical elements of the basement. The features of the lithospheric magnetic field, as a parameter reflecting the present position of tectonic structures and their physical properties, can be used for their contouring in combination with other geological and geophysical methods.

Key words: satellite magnetic observations, long-wave lithospheric magnetic anomalies, Balkan region, Rhodope.

Introduction

According to a complex of geophysical sounding, the study of the deep structure and dynamics tectonosphere active regions is the most important problem of the modern geophysics

Currently, there is a unique opportunity to investigate the magnetic anomaly (MA) field of regional lithospheric anomalies and construct the magnetic maps using data from several sources of observations at different heights above the surface of the Earth. The first source was used is satellite data (Reigber et al., 2002), and the second one is the results of the Global Earth Magnetic Anomaly Grid (EMAG2) (Maus et al., 2009).

Magnetic anomaly maps provide insight into the subsurface structure and

composition of the Earth's crust and successfully used for reconstructing the geophysical and geological models of the Earth's crust, in order to study the crustal properties and structure (Vine and Matthews, 1963; Purucker and Whaler, 2007).

Recently there was an increase of the interest in the study of large-scale (or long-wave) anomalies that are covering an area of a few hundred km. The spatial pattern of these long-wave anomalies reflects the spatial distribution of the magnetic properties and thickness of deep magnetized layers.

The analysis of the spatial distribution of the MA field shows that the anomalous part of the field significantly is decreasing at the orbital heights of satellites: the high frequency anomalies are smoothed, and only the low frequency regional anomalies with spatial periods of 400–500 km and intensity of a few dozen nT are remained.

The investigations based on the satellite magnetic measurements show that large tectonic units, such as shields, cratons, and subduction zones, are marked by positive magnetic anomalies (due to the increased magnetic susceptibility), while basins and abyssal planes produce negative anomalies are caused by crustal thinning and an elevated Curie isotherm.

At the beginning of XXI century, the possibilities for analyzing the parameters of the geomagnetic field, previously determined by the Earth's satellite vehicles, have been significantly expanded, due to launch of the unique Earth orbiter, the CHAMP satellite, which provided almost real-time highly accurate data from 2000 up to 2010 (Reigber et al., 2002).

The authors of the present paper carried out successful studies of the lithospheric MA field using the geomagnetic data from CHAMP measurements above different territories (Abramova et al., 2011; 2014).

In 2009, a large group of authors (Maus et al., 2009) has created EMAG2: a 2–arc min resolution Earth Magnetic Anomaly Grid compiled from satellite, airborne, and marine magnetic measurements. Grid resolution is of 2-arc min, the altitude above the geoid - 4 km.

The objective of this paper is to study the morphology of the regional lithospheric magnetic anomalies and its relationship with other geophysical fields, derived from the CAMP satellite measurements and constructed, according to data EMAG2 over the Balkan Peninsula. This region is of the interest due to the presence of large tectonic units of the different origin.

The sources of the lithospheric anomalous magnetic field from physical and geological - tectonic standpoints

The MA field of the continental lithosphere is very diverse. The sources of the anomalies are concentrated within some area in the lithosphere, which is referred to as the magnetoactive layer. The upper boundary of this layer either coincides with the Earth's surface or is buried at a depth of about 10 km in the blind and folded regions. The bottom boundary of the magnetoactive layer is either the isothermal surface corresponding to the Curie point of magnetite or the Moho (Arkani-Hamed and Strangway, 1986; Tanaka et al., 1999).

The attempts of geological interpretation of the satellite magnetic anomalies lead to the conclusion that they are associated with a few different sources that is equally probable. Most of the interpreters (Arkani-Hamed and Strangway, 1986; Pashkevich et al., 1994) believe that the anomalies are appearing because of the variations in the average effective magnetization of large lithospheric segments or to the changes in the thickness of the lithospheric magnetoactive layer.

The anomalies can be generated by lateral variations in the temperature of the homogeneous lithospheric layer and, correspondingly, the variations in the depth of the isothermal Curie surface for magnetite.

The lateral variations in the composition of the magnetic minerals are another source of the satellite magnetic anomalies that is equally important. The key part is played by the degree of the magnetization of the bottom crust, which significant intensity and variability are now without doubt (Pashkevich et al., 1994).

To all appearances, most of the revealed anomalies are produced by the simultaneous action of the two mentioned factors.

Within the young tectonic regions, even with low deep temperatures, the overall Earth's crust is poorly magnetized, which is believed to be associated with its more acidic composition. There are significant differences between the Pre-Riphean formations, which are the main sources for the magnetic anomalies, and the younger structures such as the Phanerozoic crust, which are typically less magnetic. The Pre-Riphean platforms include the exposed shields (cratons) and Pre-Riphean basements buried under the younger deposits. The MA fields within different platforms have different origin (Goodwin, 1996).

The CHAMP satellite magnetic data

The data on the geomagnetic field measured on the satellite board should be collected, systematized, and converted into a suitable form for further processing. Among the huge data volumes obtained, the components, that most adequately characterize the lithospheric MF, should be identified, and the maps reflecting the distribution of MA field in the studied region should be constructed, and the geophysical and geological interpretation of the revealed magnetic anomalies should be carried out.

The near-polar circular orbit of the CHAMP satellite with an inclination angle of 87.3° permitted to take measurements at each point in space in different local times, and its low altitude ensured a better resolution of the measured parameters. Owing to this orbit configuration, the satellite ensured uniform coverage of the whole globe surface with high-quality high-precision measurements. The data have a 1-s resolution in time, which corresponds to ~7 km in space. The satellite made ~14 passes per day with uniform coverage of the whole local time interval (Reigber et al., 2002).

The satellite was equipped with two magnetometers: the Overhauser scalar magnetometer (OVM), which recorded the magnitude of the total magnetic field (T), and the fluxgate FGM magnetometer, which measured three orthogonal vector components (X, Y, Z).

About 5,000 measurements of the magnetic field were included in the mapping database.

To meet the objective in the present study, we selected the measurements of the geomagnetic-field components along ~200 sweeps of the satellite orbit taken in 2008, when the CHAMP altitude was at a minimum (310–320 km). These data cover the territory between 40° and 46° north latitude and between 18° and 30° east longitude.

Methods of data processing

The technique for detecting regional lithospheric magnetic anomalies from satellite measurements above different territories includes:

- collecting and summarizing measured data and bringing them into a convenient form;
- distinguishing components for the most adequate description of the lithospheric magnetic field from huge data arrays by specially developed techniques; and
- mapping the distribution of the components of the anomalous magnetic field.

Because of the measured at satellite altitudes field is a sum of contributions from several source (external and internal) with respect to the Earth's surface, the main problem of analysis consists in correct resolution of the total magnetic field into components originating from different physical sources.

The primary satellite geomagnetic field includes the following superposed components: (i) the main geomagnetic field, generated by magnetohydrodynamic sources in the liquid part of the Earth's core; (ii) outer fields, generated by magnetospheric and ionospheric current systems; (iii) induction fields, produced by currents in the conducting layers of the crust and upper mantle; and (iv) the anomalous field, related to the magnetization of lithospheric rocks.

The lithospheric magnetic field remains after successive removal of all "excess" components from the measured values, which makes the reliability of its detection dependent on the techniques selected for description of the removed parts. This, so-called physical approach of distinguishing lithospheric data, has become almost classical. It was improved by the authors in terms of subtraction of the main magnetic field, which is usually represented by the International Geomagnetic Reference Field (IGRF), based on the total magnetic field.

Observations of the world network of magnetic observatories, which are very nonuniformly distributed over the Earth's surface, are the basic array of experimental data for IGRF models. In areas with no observatories, the SHA grid is filled with additional data (from satellite, airborne magnetic and marine surveys). In this case, a considerable part of the data is lost, and the advantage (e.g., the homogeneity of satellite measurements in space and time) is artificially violated. The selection causes problems: the quantity of discarded data is different for different days, and their position in space is also very nonuniform. As a result, several competing models are constructed, and the best one is selected every five years; which must describe the main magnetic field at each point of the globe with minimum average error.

The preset parameters of the orbit of the CHAMP satellite permit daily measurements of the geomagnetic field at the nodes of an almost uniform grid above the entire Earth's surface. This permits expansion of 14 field components obtained during the day with a second-long resolution into spherical harmonics to power and to order of

magnitude in order to construct the average daily spherical harmonic model (ADSHM) for the main magnetic field for each day rather than carry out averaging for a long time interval (one year), as it is customary (Golovkov et al., 2007). We use ADSHM coefficients in a specially developed program to eliminate the main field from experimental values.

$$U(r, \theta, \lambda) = a \cdot \sum_{n=1}^N \sum_{m=0}^n \left(\frac{a}{r}\right)^{n+1} (g_n^m \cos m\lambda + h_n^m \sin m\lambda) \times P_n^m(\cos \theta)$$

$$X = -\frac{1}{r} \frac{dU}{d\theta}; \quad Y = \frac{-1}{r \sin \theta} \frac{dU}{d\lambda}; \quad Z = -\frac{dU}{dr},$$

where U is geomagnetic potential at a point with the geographical coordinates (r, θ, λ) ; X , Y , and Z are the northern, eastern, and vertical components of the measured field; a , the Earth's average radius; are associated Legendre functions of power n and order m ; g_n^m and h_n^m are the coefficients of the field model.

Magnetospheric current systems were approximated by the first zonal harmonic in spherical harmonic resolution, whereas ionospheric ones were approximated by linear or parabolic trends.

Geomagnetic data were selected only for the passes made by the satellite at night (LT from 22:00 to 6:00) and only on magnetically calm ($kp \leq 1$ and $Dst \leq 20$) days.

A specially developed program for detecting geomagnetic fields from the total quantity of the CHAMP records for Balkan was used to compile a base of experimental data on the modulus of the total vector and the components of the anomalous lithospheric magnetic field.

Mapping the anomalous lithosphere magnetic field above the Balkan territory

By applying the technique for the analysis of the CHAMP satellite data that was described above, we calculated the maps of spatial distribution of the modulus (Ta) and vertical component (Za) of the anomalous geomagnetic field at the satellite altitude of ~300 km above the Balkan territory. Maps were compiled with the use of the GMT software (Wessel and Smith, 2007) from the CHAMP data.

In order to increase the reliability of the mapping and to examine the reproducibility of the results, the authors of the article calculated the anomalous magnetic field using a few independent sets of the satellite data. A comparison of different versions of maps based on these input data showed that the spatial structure of the field is reproduced by hugely reliably.

The contour map of the modulus of the anomalous lithospheric (longwave) magnetic field Ta over the Balkan region at the altitude ~ 300 km is presented by Fig. 1. The map scale is 1: 5,000,000, the data is used in the median averaging 5×5 minutes.

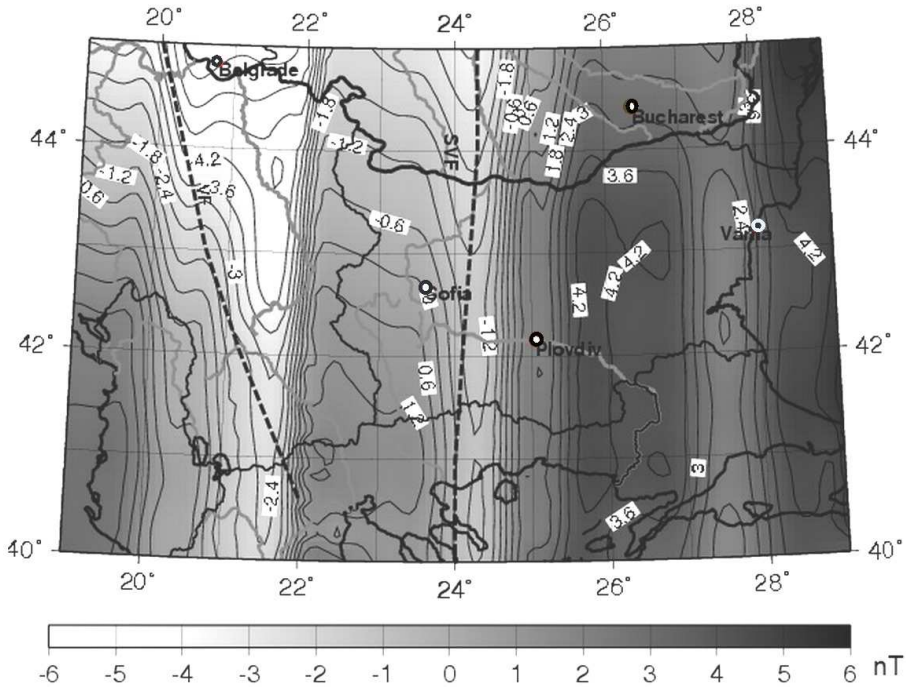


Fig. 1. Contour map of the lithospheric (longwave) anomalies of the magnetic field modulus (Ta) above the Balkan territory. The CHAMP satellite observations altitude is ~300 km. Faults: VF – fault zone Vardar; SVF - lineament Svalbard – Vardar.

Fig. 2 shows the map of the modulus T_a of the anomalous lithospheric field of the Balkan region, based on the data of Global Earth Magnetic Anomaly Grid (EMAG2) presented by (Maus et al., 2009). The altitude above the geoid is 4 km. The map scale is 1: 3,000,000, the data is used in the median averaging 5×5 minutes. Letters mean faults: IMF –Intra-Moesian, PBF – Predbalkan, STF –Struma, MARF Maritsa, CRF – Central Rhodopean.

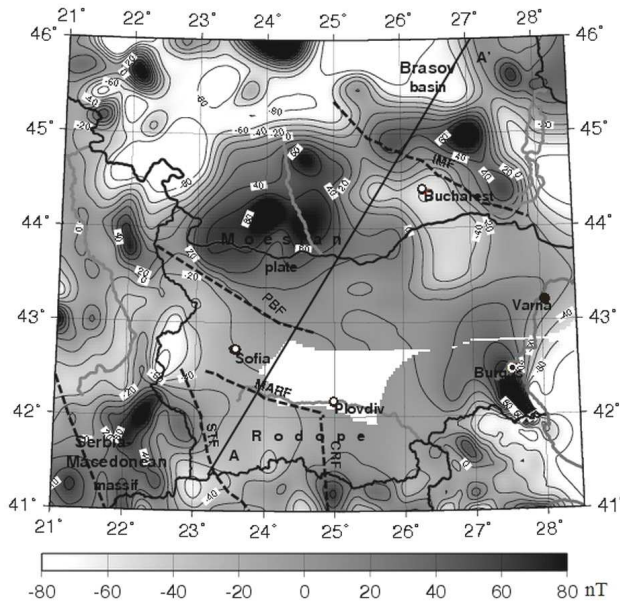


Fig. 2. Contour map of the magnetic anomalies field modulus (T_a) above the Balkan.

There are some «white spots» on the map (Fig. 2) due to the absence of airborne and marine magnetic data in the study of territory and Bulgarian shelf in the EMAG2 base. Nevertheless, there is data that allow to make the conclusions about magnetic qualities of deep immersed layers of crust of Bulgarian territory.

The map of the anomalous magnetic field at the observation altitude of 4 km (Fig. 2) differs considerably from the field distribution at the altitude of 300 km (Fig. 1).

At an altitude of 4 km, the reader could see the strong fragmentation of the positive and negative anomalies in comparison with the field on the satellite altitude. This fact makes a logical sense, since the measurements of the geomagnetic field at high altitudes works as a "low - pass filter"; in other words, it suppresses local anomalies and maintains regional anomalies in a little distorted form at the same time. Decrease of the anomalies amplitude with the altitude due to the sources parameters of lithospheric anomalies: the more the depth of the magnetized body and its horizontal dimensions, the slower decrease anomalies with the altitude. Therefore, high-altitude observations are stored anomalies caused by large-scale structures that lie at great depths.

Geologic - tectonically position and the geophysical characteristics of the Balkan area

The study of the Mediterranean – Carpathian zone, the part of which is Balkan region, is conducted by the variety of geophysical methods, including different methods of seismic tomography (Wortel & Spakman, 2000; Gvirtzman, 2002; Yanovskaya & Lyskova,

2013).

The south part of the Balkan zone was formed as a result of collision of continental lithosphere blocks of various sizes, detached from the northern fragments of Gondwana and displaced northward, through the Thetis ocean in Mesozoic and Cenozoic (Wortel and Spakman, 2000).

The region has an extremely complicated structure of the lithosphere composed groups of fold belts and crystalline arrays. The tectonic activity is continually lasting, its nature attributed interplate interaction and (or) the mantle processes. Intense folding which resulted from of tension processes, contributed to the rise of magma in the upper layers of the lithosphere and activation of the volcanism, which takes place so far (Haak et al., 1989; Galanopoulos, 1993; Spakman et al., 1988; Wortel and Spakman, 2000). At the depth of about 200 km found the low-speed area, produced, apparently, by melting of the upper mantle rocks. In the area of southern Bulgaria there is a continuation of this zone (Spakman et al., 1988). High heat flow values under the territory of the West and Central Rhodope testify of this.

On the northern edge of the Balkan velocity distribution of vertical sections on profiles crossing the South-Eastern Carpathian, suggest the presence of subduction of ancient oceanic slab from east to west under the Eastern Carpathian (Girbacea & Frisch, 1998; Wortel & Spakman, 2000; Gvirtzman, 2002; Yanovskaya & Lyskova, 2013).

For example, the results of surface-wave tomography, which were applied for the data collected at stations in Eastern and Western Europe, show that along the line passing through the zone of basin Brashov and the Vrancea area in the NE-SW direction, there is a significant change in the structure when passing through the vertical «fault», where the deep-focus earthquakes take place in the Vrancea area (Yanovskaya & Lyskova, 2013). This area, in the southeastern corner of the Carpathian Mountains, is a unique opportunity to study the final and short phase of the plate convergence, when the part of subducting lithosphere is, finally, detaches from the subducting plate and begins to sink into the mantle (Wortel and Spakman, 2000; Gvirtzman, 2002).

In the Balkan province observed almost all the features of seismogenic zones established for many seismically active regions of the Earth: (i) the increased thickness of the Earth's crust and its consolidated parts (Dachev, 1988); (ii) abnormal velocity differentiation of the section and anomalous absorption of seismic waves (Dachev & Volvovsky, 1985); (iii) regional decrease of seismic velocities in the upper part of the mantle (Dachev & Volvovsky, 1985); Yanovskaya & Lyskova, 2013); (iv) abnormal asthenosphere layer location (Dachev et al. 1985); (v) availability low- velocity layers (waveguides) (Dachev and Volvovsky, 1985); (vi) complex layered structure of the boundaries "crust - mantle" (Wortel & Spakman, 2000); (vii) the presence of layers with anomalously low conductivity in the crust and mantle (Abramova et al. 1994, 1997), (viii) the increased values of the heat flow, and so on.

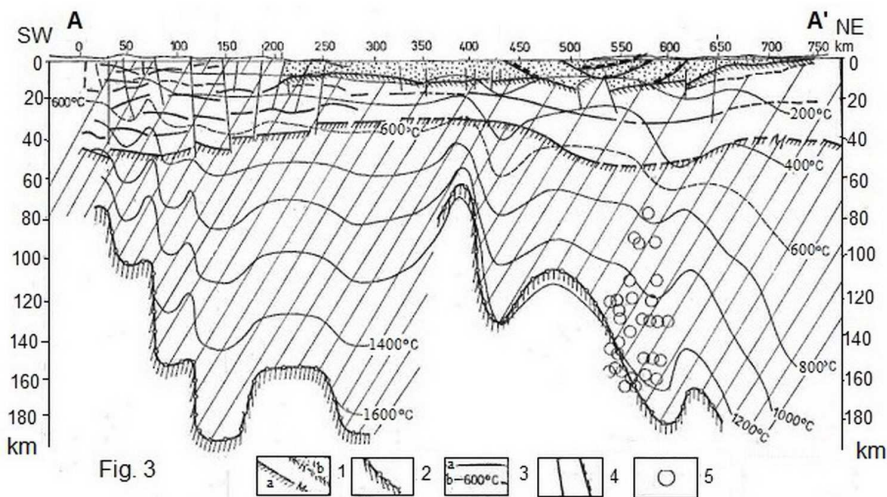


Fig. 3. The thermal model of the lithosphere along the profile Rhodope - Moesian platform - the South-Eastern Carpathians - Moldavian platform (Dachev, 1988).

1 – the lithosphere boundaries: Moho (a), sedimentary layer (b); 2 – the upper boundary of the asthenosphere layer; 3 - isotherms (a) and the Curie isotherm (b); 4 - faults (a) and thrusts (b); 5 - estimated channels of intense convection heat input.

Geothermal model of the lithosphere along with the profile AA' are shown in Fig. 3 (for the profile location, see Fig. 2). Profile crosses the Carpathian- Balkan region from South-Western Rhodope in Bulgaria to the Vrancea region in the Eastern Carpathians in Romania (Kutas, 1978; Demetrescu, 1982).

As shown in Fig. 3 the territory of the Southern Balkan and Eastern Carpathians is characterized by unsteady and heterogeneous thermal field, which is typical for activated alpine areas. The available experimental data for these areas is limited; however, it is known that in the southern part of the Rhodope the temperature at the Moho border rises up to 800-900° C. The lithospheric heating in this area is expressed as an abrupt increase in the asthenosphere temperature values 1200-1300 °C, which, in turn, causes a rise of the Curie isothermal surface of magnetite and a decrease in the magnetic-layer thickness.

The some factors discussed above are expected to be manifested in the AMF behavior.

The lithospheric magnetic field maps analysis

As the figures 1 and 2 illustrate, in general, the regional background of the map is characterized by the low values of the lithospheric anomalous magnetic field that is usually characterizing the tectonically active regions.

It should be noted that the anomalous field magnitude at altitudes of 300 km is relatively small in comparison with such significant anomalies like the Kursk anomaly observing in the Voronezh Crystal massif territory (Abramova L., 2012). In this case, we can discuss the qualitative image of the lithosphere magnetic field, which is characteristic for the crust bottom.

Nevertheless, it is seen that the lithospheric AMF (Fig. 1) is divided into two positive and negative parts. The separation takes place approximately along the 25° E. This line corresponds to the position of the transcontinental lineament Svalbard – Vardar (SVF) which observed in tectonic schemes decryption of satellite images the western part of the Alpine Mediterranean belt and also corresponds to the position of the Madan-Nedelino intraformational glide (M-N) and central Rhodope fault.

It is observed negative values of the anomalous magnetic field in the Vardar fault (VF) area, apparently indicating on the activation of tectonic processes in the deepest parts of the area.

On the map (Fig. 2) it is demonstrated the mosaical structure of alternating large areas of positive and negative anomalies.

In the research of faulting and block structures of the Balkan crust the idea that it is made up of separate megablocks has been argued, which are separated by deep discontinuity (Velchev et al., 1970; Ivanov, 1981; Wortel and Spakman, 2000; Zagorchev, 2001). Megablocks vary in thickness and composition of the crust and separated by the deep faults. The latter as shown in Fig. 2, are characterized by low values of the anomalous magnetic field, for example, such as Predbalkanianian (PBF), Struma (STF), Vardar (VF), Maritsa (MARF), Intra-Moesian (IMF) etc.

In the northern part of the map AMF seismically active zone Carpathian, as a rule, characterized by negative values of the magnetic field.

In the northeastern corner of the map the positive values of the field territorially match the part of subducting from the east oceanic plate, which is bounded by Intra-Moesian fault (IMF) on the south. A significant decrease in values of the AMF is observed in the Brashov basin and the Vrancea area regions.

The mechanism of subduction of the cold lithospheric slab from the east under the Carpathian, the spread of the tearing process and the transition from partial to complete of the detachment of the subducting plate are currently actively discussed in geophysics (Wortel and Spakman, 2000; Gvirtzman, 2002). These studies suggest that the area of strong bending of the Southeastern Carpathian and detachable part of the plate is limited to two crust faults: Trotus the north and Intra-Moesian the south.

In the area of Brasov basin the root of disconnection is viscously connected with the initial lithosphere and pulls it downward. Researches exactly under this area indicates low seismic velocity anomaly (Frish et al., 1998) possibly representing heat asthenospheric material. Magmatic processes occurring in this area were discussed by Girbacea & Frish (1998).

The current research is very logical and fully corresponds to the researches in the field of tectonic structures and geophysical fields under Brashov basin and on the border of Vrancea area.

It is clearly recorded in the anomalous magnetic field: (i) tectonic bending East Carpathian (Gvirtzman, 2002), fixed by the change of sign of AMF and its significant gradient; (ii) restriction of subducting slabs from the south Intra-Moesian fault a sharp change from positive to negative values of the field; (iii) significant reduced in the value of the field in Brasov basin, due to the rise of the Curie isothermal surface of magnetite and a decrease in the magnetic-layer thickness due to the high position of the hot asthenosphere.

In the central part of the map (23° – 25.5° E and 43° - 45° N) there is an amoeboid

isometric positive anomaly with amplitude about 100 nT, which is surrounded by zones of decreased field values. The position of this anomaly corresponds to the well-known Moesian positive regional anomaly, located in the western part of the Moesian platform and on the territory of the Carpathian depression (Dachev, 1988). The anomaly has isometric shape and somewhat elongated in the north-east direction. Its length is about 200 km.

Small amplitude positive magnetic anomaly occupies a large area on the territory of Serbia-Macedonian massif.

Rhodope zone

A reflection of the large-scale tectonics can be seen in the AMF for the Rhodope example. For this purpose we used the work of R. Ivanov (1981), in which was considered the hypothesis of the Central- Rhodope nappe existence.

On the more detailed map of the Rhodope magnetic field (Fig.4) the position of the fault structures and partial massifs, taken from (R. Ivanov, 1981), are marked.

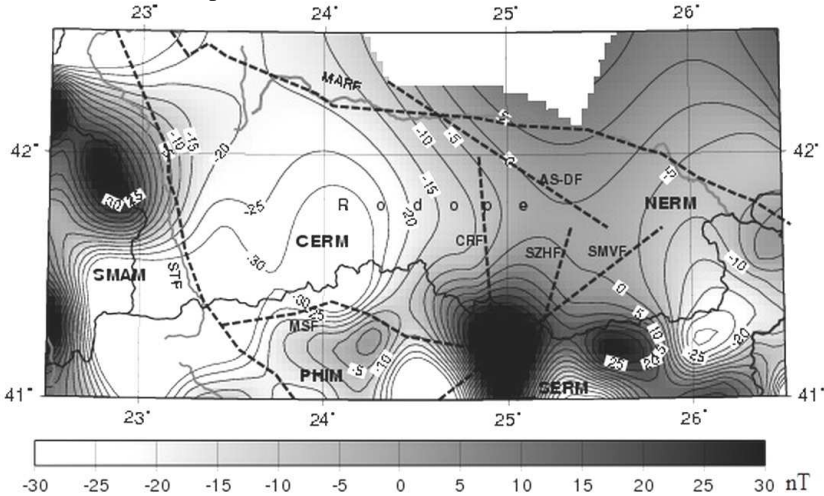


Fig. 4. Contour map of the magnetic anomalies field modulus (T_a) according to EMAG2 above the Rhodope territory. The altitude above the geoid is 4 km.

Great faults and sliding zones: SMV - Simvolon, SZH - Snezhin, MAR - Maritsa, AD - Asenovgrad-Diadovo, MSF - Mesta cryptofault, STF - Struma, RF - Rhodope fault. CERM - Central-Rhodope (partial) massif; NERM - North-East Rhodope (partial) massif; SMAM - Serbian -Macedonian (partial) massif; SERM - South-East Rhodope (partial) massif; PHIM - the autochthonous part of the CERM

According to the author, Rhodope massif (RM) is a territory of metamorphic rocks and granites of partially overlapped by Tertiary molasse and volcanics. Tertiary molasse depression and related faults divide the array into several «partial» massifs: North-East Rhodope (partial) massif (NERM), South-East Rhodope (partial) massif (SERM), Central-

Rhodope (partial) massif, including Rila and Pirin (CERM), and Serbian -Macedonian (partial) massif (SMAM), (Fig.4).

The author considers that the whole allochthonous slab, (CERM), which was built by Rhodopsin series, covers almost the entire region of Central Rhodope, Rila and Pirin.

The great linear gravimetric transition the light mass of CERM from considerable heavier mass of SERM is interpreted as evidence «Central – Rhodope deep fault» (CRF) (Dachev, 1980), whereas the structure on the surface do not support the existence of such fault.

The consideration of AMF map reveals an amazing coincidence of the most probable borders of the CERM allochthone and anomalous magnetic map contours. As it can be seen, in general, the entire CERM area is characterized by negative AMF values.

The western boundary of the magnetic anomaly is clearly limited Struma fault and corresponds well with the assumption, that the CERM western boundary is covered by the sediments Tertiary molasse depressions along the Struma river. Here the significant gradient of changes in the anomalous magnetic field and the change of field sign from negative to positive is fixed. The positive field values describe the field of the neighboring Serbian -Macedonian massif (see Fig.2).

The northern boundary of the nappe runs along the Sredna gora zone. To the East the SE-trending Asenovgrad– Diadovci (AS-DF) fault is the margin of the allochthone of the Central- Rhodope nappe. The boundary position of the magnetic anomaly also coincides with it.

The geological map (Birk et al., 1970) suggests the existence of one large E-W striking syncline along the southern slope of the Rhodope massif, Mesta fault, (MSF on the Fig.4). The magnetic anomaly boundary is consistent exactly with MSF.

On the eastern nappe border powerful thrust folding is marked, retrogressive metamorphism and mylonitization of NNE zones with powerful serpentine layers at the border between CERM and SERM (Snezhinskiy Synclinorium) are marked.

Negative anomaly is evidence of the raising of the Curie isothermal surface of magnetite and a decrease in the lower part of the crust magnetic-layer thickness in south part of the region, which is demonstrated by the AMF maps.

As it was mentioned above, seismic data discover the presence of zones of the waveguide and electromagnetic investigation fixed the crust conductivity anomaly in Central Rhodope. Unfortunately, these data were obtained from the only one profile. The using of magnetic anomaly data affords the possibility of the extrapolation and generalization of geophysical fields in the researched area.

Conclusions

Given materials show that satellite magnetic observations add the information to regional tectonic studies. The compiled maps and analysis of the lithospheric anomalous magnetic field in Balkan area show their consistency with geological ideas of the zoned block structure of the crust in this region. Furthermore, their localization coincides with other geophysical data, like the thermal field and the field of seismic velocities.

Through the example of Central Rhodope Massif is shown the possibility of confirmation of existence of the subsurface discontinuity hidden under the sediments.

As a parameter reflecting on the present-day position of tectonic structures and their physical properties, the lithospheric magnetic field might be used for their description in combination with other geological and geophysical methods.

Acknowledgments. We thank anonymous colleagues for serving as peer reviewers of manuscripts submitted for publication for their constructive and friendly comments. The figures are made by using GMT (Wessel and Smith, 2007).

References

- Abramova, D., L. Abramova, S. Filippov, A. Frunze, 2011. The prospects of using satellite measurements to analyze regional magnetic anomalies, *Izv. Atm. & Oceanic Phys.*, Engl. Transl., 6, 53–63.
- Abramova D., L. Abramova, 2014. Lithospheric magnetic anomalies in the territory of Siberia (from measurements by the CHAMP satellite), *Russian Geology and Geophysics*, Elsevier, 55, 854–863. Available online at www.sciencedirect.com
- Abramova L., Iv. Varentsov, A. Velev, R. Gavrillov, N. Golubev, M. Zhdanov, E. Martanus, E. Sokolova, V. Shneyer, 1994. Investigation of the deep geoelectrical structure of the Bulgaria territory. *Izvestia Phys. of the Solid Earth*, 11, 59-69.
- Abramova L., Yu. Abramov, V. Shneyer, 1997. Study of Electromagnetic Field along the Crete-Bulgaria Profile. *Izvestia Phys. of the Solid Earth*, 33, (2), 155-161.
- Abramova, D., L. Abramova, Iv. Varentsov, V. Kulikov, I. Lozovsky, the Working Group KIROVOGRAD, 2012. The correlation of magnetic field anomalies and geoelectric crustal structures on the Voronezh massif western slope. *Geophysical Journal*, 34, № 4, 62-69.
- Arkani-Hamed, J. and D.W.Strangway, 1986. Effective Magnetic Susceptibility Anomalies of the Oceanic Upper Mantle Derived from Magsat Data, *Geophys. Rev. Lett.*, **13**, 999–1002.
- Birk, F., de Boer, H., Kronberg, P., Meyer, P., Pilger, A., Shenk, P. 1970. Zur Geologie des Rhodopen-Kristallins in Gebiet zwishen Strimon und Nestos (Griechisch- Ostmacedonien). *Beih. Geol. Jb.* 88. 179 p., Hannover.
- Dachev Khr., 1988. Structure of the Earth crust in Bulgaria, (In Bulgarian), 334 pp., Technique, Sofia.
- Dachev, Khr. 1980. Geodynamic problems of the Balkan Peninsula from the standpoint of regional geophysical data. *Geodynamics of the Balkans*. (In Bulgarian), Technique, Sofia, 9-25.
- Dachev, Khr., I. Volvovsky, 1985. Deep structure of Bulgaria along the Petrich- Nikopol EMCM - DSS traverse, *Bollettino di Geofisika Teorica ed Applicata*, Vol. XXVII, N. 108, 263- 278.
- Dachev, Khr., I. Volvovsky, O., Popova, V. Babinets, F. Velev, V. Geiko, L. Natroshvili, 1985. The procedure and results of seismic investigations on the Bulgarian section (Petrich- Nicopol) of the geotraverse VII. *Geophysical Journal*, 7, 5 35-43.
- Demetrescu C., 1982. Thermal Structure of the crust and upper Mantle of Romania, *Tectonophysics*, **90**, 123-135.
- Galanopoulos D., 1993. Preliminary magnetotelluric studies along the Hellenic Volcanic Arc: implications for the collision between the African plate and the "Aegean" microplate, *Phys. of the Earth and Planetary Interiors*, **81**, 139-153.
- Girbacea, R., and Frisch,W., 1998. Slab in the wrong place: Lower lithospheric mantle delamination in the last stage of the Eastern Carpathian subduction retreat, *Geology*, 26, 611–614.

- Golovkov, V., T. Zvereva, T. Chernova, 2007. Space– Time Modeling of the Main Magnetic Field by Combined Methods of Spherical Harmonic Analysis and Natural Orthogonal Components, (In Russian), *Geomagn. & Aeron.*, 47, (2), 256–262.
- Goodwin, A.M., 1996. *Principles of Precambrian Geology*, 327 pp., Elsevier, New York.
- Gvirtzman Z., 2002. Partial detachment of a lithospheric root under the southeast Carpathians: toward a better definition of the detachment concept // *Geology*. V.30. P. 51-54.
- Haak V., Ritter O. and P. Ritter, 1989. Mapping the geothermal anomaly on the island of Milos by magnetotellurics, *Geothermics*, 18 (4), 533-546.
- Hemant, K. and S., Maus, 2005. Geological Modeling of the New CHAMP Magnetic Anomaly Maps Using a Geographical Information System Technique, *J. Geophys. Res.*, 110, 1–23.
- Ivanov R., 1981. The deep-seated Central-Rhodope Nappe and the interference tectonics of the Rhodope crystalline basement, *Geologica Balcanica*, 11 (3), 47-66.
- Kutas, R., 1978. Heat flow field and thermal model of the Earth's crust. (In Russian), 140 pp., Naukova dumka, Kiev.
- Maus S., U. Barckhausen, H. Berkenbosch, N. Bournas, J. Brozena, V. Childers, F. Dostaler, J. D. Fairhead, C. Finn, R. R. B. von Frese, C. Gaina, S. Golynsky, R. Kucks, H. Lu`hr, P. Milligan, S. Mogren, R. D. Mu`ller, O. Olesen, M. Pilkington, R. Saltus, B. Schreckenberger, E. The`bault, F. Caratori Tontini, 2009. EMAG2: A 2–arc min resolution Earth Magnetic Anomaly Grid compiled from satellite, airborne, and marine magnetic measurements, *Geochem. Geophys. Geosyst.*, 10, (8), Q08005, doi:10.1029/2009GC002471.
- Pashkevich, I.K., D., Pecherskii, 1994. *Petromagnetic Model of the Lithosphere*, (In Russian), 97 pp., Naukova dumka, Kiev.
- Purucker, M., and K. Whaler, 2007. Crustal magnetism, in *Treatise on Geophysics*, 5, *Geomagnetism*, chap. 6, 195–237, Elsevier, Amsterdam.
- Reigber C., Luhr H., P., Schwintzer, 2002. CHAMP mission status, *Adv. Space Res.*, 30, 129–134.
- Spakman W., Wortel M.J.R. and N. Vlaar, 1988. The Hellenic subduction zone: a tomographic image and its geodynamic implications, *Geophys. Res. Lett.*, 15 (1), 60-63.
- Tanaka A., Okubo Y., Matsubayashi, 1999. Curie point depth based on spectrum analysis of the magnetic anomaly data in East and Southeast Asia, *Tectonophysics*, 306, 461-470.
- Velchev Ts., Dachev, Ch., Petkov Iv., 1970. Geotectonic structure of Bulgaria in the light of the geophysical fields, (In Russian), *Rep. BAN*, 23 (6) 699-702.
- Vine, F. J., and D. H. Matthews, 1963. Magnetic anomalies over oceanic ridges, *Nature*, 199, 947–949.
- Volvovsky I, Dachev Khr., *O. Popova et al.* 1987 (In Russian). *Earth's crust of the Bulgaria*. Moscow.: Geophysical Committee. 110 c.
- Wessel, P., Smith, W.H.F., 2007. The generic mapping tools. Technical reference and cookbook version 4.2, <http://gmt.soest.hawaii.edu>.
- Wortel M.J.R., Spakman W., 2000. Subduction and slab detachment the Mediterranean - Carpathian region, *Science*, 290 (5498), 1910-1917.
- Yanovskaya T.B., Lyskova, 2013. Velocity structure of the upper mantle of Europe on the results of a noise surface - wave tomography, *Izvestia Phys. of the Solid Earth*. Engl. Transl, №5, c. 3-11.

Литосферни магнитни аномалии в Балканския регион

Д. Абрамова, С. Филиппов, Л. Абрамова, Ив. Варенцов

Резюме. Определена е позицията на литосферните аномалии на магнитното поле на територията на Балканския регион. Ние използвахме данните от изкуствен спътник на Земята CHAMP и данните на Global Earth Magnetic Anomaly Grid (EMAG2). Статията описва метод за обработката на сателитните данни и начините за разделянето на общите регионални литосферни магнитни аномалии от сателитни измерените. Картите на магнитното поле на аномалиите за две различните височини над геоида са построени за Балканския регион. Отчитат се геоложката и тектонска природа на магнитните аномалии и връзката им с дълбоките структури на земната кора. Предварителната интерпретация на магнитните карти показва, че аномалиите се корелират с големите геоложки и геофизични елементи на земната кора. Характеристиките на литосферното магнитно поле, като параметър, отразяващ настоящото положение на тектонските структури и техните физични свойства, могат да се използват в комбинация с другите геоложки и геофизични методи.

THE RELATIONSHIP BETWEEN THE ELECTROMAGNETIC PARAMETERS AND TECTONIC STRUCTURE OF THE TERRITORY OF BULGARIA

L. Abramova¹, Iv. Varensov¹, D. Abramova²

¹Geoelectromagnetic Research Centre of the Institute of Physics of the Earth, Russian Academy of Sciences, Moscow, 142190 Russia. ludabr50@mail.ru, ivan_varentsov@mail.ru

²Institute of Terrestrial Magnetism, Ionosphere, and Radio Wave Propagation, Moscow, 142190 Russia. abramova@izmiran.ru

Abstract. The results of magnetovariational sounding at the area of Rhodope Massif of the Republic of Bulgaria were examined. Magnetovariational response functions were calculated and the maps of - modulus and phases of the induction vectors were built based on the results. The comparison of these maps with the tectonic structure of the Rhodope was made. As a result it was shown that the MV parameters quite adequately reflect the tectonic features of the Rhodope region.

Key words magnetovariational sounding, induction vectors, conductivity anomalies, tectonic structures, Rhodope

Introduction

The present-day studies have shown that the Earth's tectonosphere consists of inhomogeneities of different ranks and structures, whose lateral position and position in the section do not always correlate with visible geologic structures. This necessitates mapping of deep-seated inhomogeneities in the crust and upper mantle in connection with the development of prognostic criteria for deep-seated oil, gas, and solid minerals and the compilation of new-generation maps for predicting concealed deposits (Shchukin, 2005).

The problem of the relationship between the crustal/mantle heterogeneities and surface structures is one of the key problems in the contemporary geology.

The electrical conductivity of the tectonosphere, which is studied by electromagnetic (EM) methods, is determined by a number of factors such as mineral and chemical composition of the rocks, porosity and pore connectivity, fluid or graphite content, and temperature. The conductivity at the crustal and upper mantle depths is predominantly determined by temperature and fluid content.

adjacent shelf. There were made more than 80 points of sounding in the wide interval of the variation periods: from 10 minutes to 24 hours.

During the land experiments were carried out synchronous measurements by a 5-component stations IZMIRAN-5. They measured the D (east), H (north) and Z (downward) magnetic field and Ex (north) and Ey (east) electrical field components.

A special magnetic instrument complex installed at the Panagyurishte observatory was in operation during the whole period of the observations. This station ensured the synchronization of the EM field measurements conducted during different years.

For the experimental data processing a software complex for the analysis of time series was applied (Ashirova et al., 1989). Regarding to the research, the spectral processing involved the calculation of the complex functions of the electrical conductivity, including the determination of the parameter R and the relationship of the coincident horizontal magnetic field components in a wide range of variations periods from 10 minutes up to 3 hours.

The qualitative interpretation of the data along the Petrich--Nikopol profile was carried out. The main result of the research was the discovery of the asthenosphere layer of the increased conductivity at the top of the mantle.

The chronology and preliminary results of the work described in (Abramova et al., 1994).

The further studies in this direction were broken by the known dramatic events that changed the political and social landscape of our countries.

In this paper we have tried to make the revision and additional processing of materials, the analysis of which has been postponed until better times, and may offer a new contribution to the problem of using sensing MV data.

Definitions and theoretical prerequisites

The variations of the magnetic field of the Earth which are generated by the electrical currents flowing in the near-Earth environment induce the secondary solenoidal currents in the conductive layers of the crust and upper mantle. These fields and currents are employed in the different EM sounding methods for estimating the conductive properties of the rocks composing the crust and asthenosphere.

The magnetovariational sounding (MVS) and magnetovariational profiling (MVP) methods are based on the amplitude ratio between the spatial harmonics of the vertical and horizontal components of the magnetic variations. These methods are used for searching for and exploring the large horizontal heterogeneities in the electrical conductivity of the Earth's crust and upper mantle through the separation and analysis of the anomalous part of the field of magnetic variations (Schmucker, 1970; Gough and Ingham, 1983).

In the MVS and MVP methods, all the procedures for processing the measurements at a separate observation point and on the profile employ the linear relationship that links the horizontal components of the EM field of magnetic variations $H_x(T)$ and $H_y(T)$ at period T with the vertical component H_z

$$H_z(T) = A H_x(T) + B H_y(T) \quad (1)$$

At each observation point, the induction vectors \mathbf{C} (Schmucker, 1970) are calculated (and then plotted as the maps) from the magnetic tensor components in the following way:

$$\mathbf{C} = A_i + B_j, \quad (2)$$

with i and j pointing North and East, respectively. The induction vectors are constructed separately from the real (\mathbf{C}_u) and imaginary (\mathbf{C}_v) parts of the coefficients A and B for the selected periods.

As a result of data processing at each observation point, the components of the magnetic tensors and complex induction vectors were calculated in the interval of the periods of the magnetic variations from 15 min to 3--4 h. For the section along the Petrich--Nikopol profile, the one-dimensional (1D) and two-dimensional (2D) geoelectrical models were calculated, and the comprehensive interpretation of the obtained results with the allowance for the additional geological and geophysical parameters was carried out (Abramova et al., 1994).

The overall structure of the EM field along the profile was characterized by the following features.

1. The amplitudes of the vertical magnetic component and, hence, the components of the induction vectors C_u and C_v , within the southern part of the profile are lower than in its northern part. This looked somewhat odd, considering the fact that the distance between the northern and southern segments of the profile was at most 150 km. Due to this, it was natural to hypothesize that the behavior of the EM field in Rhodope is largely contributed by the electrical conductivity of the underlying basement layers, which smoothed out the conductivity contrast.
2. The orientation of the EM field as characterized by the layout of the induction vectors did not always agreed with the *surface* structural plan of the key tectonic units and indicated a probable misalignment between the surface and deep boundaries of the geological crustal objects.
3. The total longitudinal conductance of sediments S_s estimated during the interpretation was ~1000--1700 S in the entire territory of the observations. The value of S_s in the Rhodope region was nearly identical to S_s within the Moesian platform covered by the thick sedimentary strata. This was noticeably different from the S_s -map for the territory of Bulgaria which was constructed by Iovka Borisova based on the geological and geophysical data available at that time (Fig. 1). On the first glance, this was surprising since the Rhodope in their subsurface portion are composed of the Precambrian or Early Paleozoic crystalline schists and granitoids with very high resistivities (Dachev, 1988).
4. The regional seismic studies along the Petrich--Nikopol profile VII revealed a waveguide in the upper crust at a depth of 5--10 km (Fig. 2) (Dachev et al., 1985).

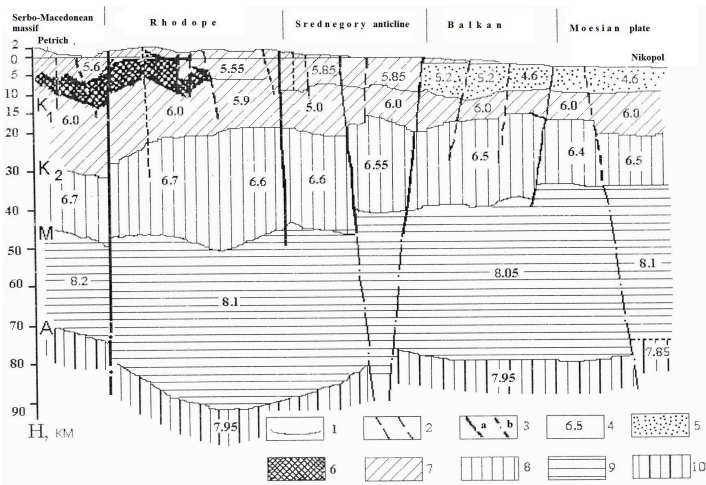


Fig.2 The Petrich-Nikopol section of the Earth crust. 1 – seismic boundaries; 2-3 faults: 2 – crustal, 3- mantle (a –certain, b –possible); 4 – leer velocity values, km/s; 5 – sedimentary layer; 6 – low velocity layer; 7 – “granite” layer; 8 – “basalt” layer; 9 – uppermost mantle; 10 – asthenosphere layer (?)

The thickness of the waveguide is 8--9 km beneath the Rhodope. The top surface of the waveguide deepens southwards, and its thickness diminishes to 5--6 km in this direction. North of the Rhodope, the top surface of the waveguide also deepens, and its thickness decreases to 6 km.

These features in the behavior of the EM and seismic fields suggested the existence of highly conductive layers in the crust and probably in the conductive asthenosphere.

In the present work, we analyze the example of Rhodope for exploring the relationship between the parameters of the EM field and the tectonic structure of the region. This segment of the Bulgarian territory is covered by the densest EM field observations along a number of the electromagnetic profiles.

The geological and geophysical settings

The Balkan territory pertains to the Alpine folded zone, a part of the Balkan--Asia Minor orogeny (Velchev et al., 1970; Dachev, 1988). This arc-shaped edifice is elongated in the NW--SE direction in its western part and in the EW direction in its eastern part. It continues up to the Pontides in the east and up to the southern portions of the Carpathians in the west.

The Moesian platform, Balkan folded system, and Rhodope zone are the main geological--tectonic elements of the region. The post-Cretaceous evolution of these territories was marked by the formation of the numerous thrusts of different ages, often with significant amplitudes of the displacement (Ivanov R., 1981, 1984; Ivanov Zh. et al.,

1984; Iosifov et al., 1994; Zagorchev, 2001).

The Rhodope massif which spreads over the territories of Bulgaria, Greece, and Serbia, is a unique geological object with a complicated tectonic structure and sharply anomalous behavior of the geophysical fields, a high hydrothermal and seismic activity, and a wide range of the ore and non-ore mineral deposits.

According to the modern understanding, the Rhodope region has undergone a profound Alpine rejuvenation including the formation of the Rhodope deep nappe and overthrusting of the Serbian--Macedonian massif over the Rhodope region (Ivanov R., 1981; Dachev, 1988; Zagorchev, 2001).

The existence of the Rhodope nappe is supported by the following body of evidence.

(i) The seismic and gravimetric data reveal the thick (45--55 km) crust beneath the Western Rhodope, which is the thickest among all the Balkan alpides; its thickness decreases northwards to 30 km in the region of the Moesian platform (Volvovsky et al., 1987; Dachev, 1988). This can probably be caused by the presence of the large thrust slices (thrust nappe) which augment the crust.

(ii) The anomalously high position of the top surface of the asthenosphere and clear traceability of the related seismic waves testify to the specific state of this region, which is caused by the redistribution of stresses in the hot thermodynamic conditions. The existence of the waveguide zone established from seismic data is associated with the thick sediments buried in this area (Volvovsky et al., 1987).

As a reference for analyzing the probable correlation between the tectonic structures and EM field, we used the study of R. Ivanov (1981) where the author explored the tectonic structure of the Rhodope region (Fig. 3, adopted from the cited paper).

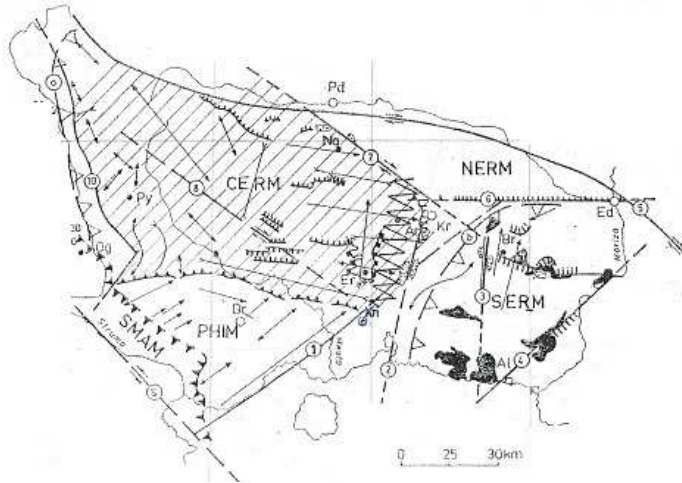


Fig. 3. Structure of a part of the Late-Alpine Rhodope massif (Ivanov R., 1981). Great faults and sliding zones: SMV - Simvolon, SZH - Snezhin, MAR - Maritsa, AD - Asenovgrad - Diadovo, STF - Struma, RF - Rhodope fault. M-N - the Madan-Nedelino intraformational glide. Towns: Pd - Plovdiv, Ed - Edrine (Odrin), Kr - Kardzali. Areas: Er - Erma-reka, Py - Pirin, Na - Norh-Rhodope Anticline.

The Rhodope massif is a territory of the metamorphic rocks and granites partially overlain by the Tertiary molasses and volcanics. The Tertiary molasse depressions and the related faults divide the massif into several “partial” submassifs: the North-East Rhodope Massif (NERM), South-East Rhodope Massif (SERM), Central Rhodope Massif (CERM), including the Rila and Pirin mountains, PHIM – the autochthonous part of the CERM, and Serbian--Macedonian Massif (SMAM), (Fig.3) (Ivanov R., 1981).

Just as the Aegean Sea and Western Turkey, the southern Bulgaria is characterized by the high heat flow ($> 2 \text{ mCal/cm}^2\text{s}$ against the average flux of $0.88 \text{ mCal/cm}^2\text{s}$ over the Eastern Mediterranean (Macris, 1977)). One of the probable explanations of this phenomenon conjectures that the Aegean region has a heated upper mantle due to the convective motion of the hot asthenospheric material which penetrates into the lithosphere. It is presumed that beneath the Aegean region there is a large lithothermal dome which originated from the asthenospheric trough. This hypothesis is supported by the works on seismic tomography (Spakman et al., 1988).

At a depth of about 200 km is the low-speed area, due, apparently, to melting zone upper mantle rocks. In the area of southern Bulgaria there is a continuation of this zone. High heat flow values under the territory of the Rhodope testify to this. Province of Southern Balkan is characterized typically unsteady and heterogeneous thermal field, which is typical for activated alpine (Kutas, 1978; Velinov, Boyadjieva, 1981).

Interpretation

For the purposes of the present study, we revisited the old data and carried out the partial processing of the EM field observations by the modern software system (Varensov, 2013). As a result of this work we built the curves of the magnetic parameters and estimated their accuracy. All the data are represented in the form of the maps showing the distributions of the key invariant complex parameters for the periods of magnetic variations ranging from 15 min to 3 h over the territory of Bulgaria.

According to the theory, the parameters of the amplitudes and directions of the induction vectors reflect the position and strike of the surface and buried deep structures. The example in Fig. 4 a, b shows the two panels of the parameters of the magnetovariational responses (induction vectors): the amplitude (modulus) of vector **C** (Fig.4a) and its direction Dir C (Fig.4b) in the southern segment of the Bulgarian territory. The maps are presented for three periods: 2200 s, 5400 s. and 8500 s. We chose these values of the periods as adequately reflect to the individual parts of the frequency characteristics.

The MV responses demonstrate the different behavior of the EM field at the different periods of the observations, which testifies to the vertical stratification of the geoelectrical section. The EM field at the relatively short periods reflects the properties of the geoelectrical section in the upper crustal layers, whereas with the growth of the period, the pattern of the field becomes increasingly dominated by the effects of the deeper structures.

The correlation between the tectonic structures and EM field is clearly observed in the case of the Central Rhodope Massif. The both panels in Fig. 4 show a zone that is

confined to the position of the allochthonous CERM (Ivanov, 1981; 1984).

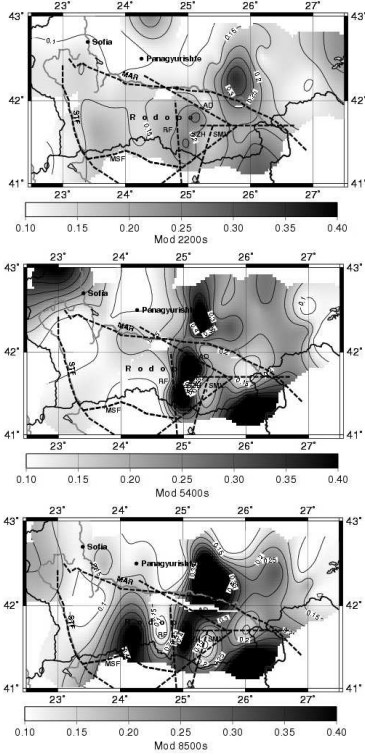


Fig. 4a. The maps of the of the magnetovariational response parameters: modulus of the induction vector C .

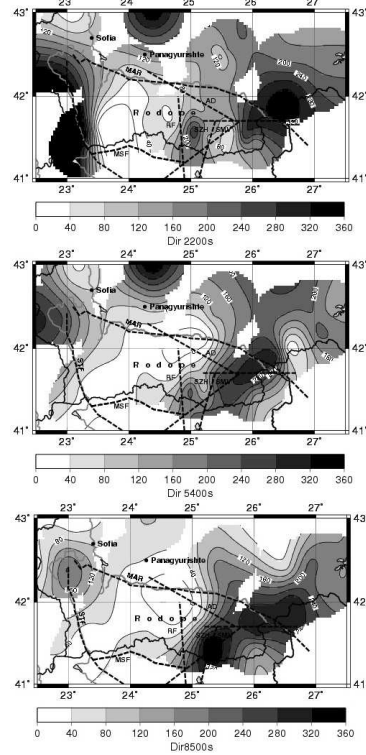


Fig. 4b. The maps of the of the magnetovariational response parameters: phases of the induction vector Dir .

As seen from panel *a* of Fig. 4, the amplitudes of the induction vectors within the Western Rhodope (CERM territory) are low at almost all the periods of magnetic variations. In contrast, the amplitudes of the induction vector in the Eastern Rhodope (NERM and SERM areas) are, on average, noticeably higher, except for the separate local anomalies.

The low amplitudes of the induction vectors indicate that the crustal conductive layer which we previously revealed when interpreting the geoelectrical section along the Petrich--Nikopol geotraverse stretches beneath the entire CERM region.

The similar delineation of CERM territory by the directional parameters of the induction vectors, which is shown in Fig. 4b, is even more distinct.

This behavior of the vectors is well consistent with the hypothesis that the integral (whole) allochthonous plate constructed of the Rhodope series overlies almost the entire CERM region (the central Rhodope, Rila, and Pirin mountains). It is composed of highly metamorphosed rocks (almandin-amphibolites, migmatites, etc.).

The *western boundary* of this conductive layer just as the bend of the SW boundary of the Struma fault are clearly outlined by the EM parameters (Fig. 4b).

It is presumed that the western CERM boundary is hidden beneath the sediments

of the Tertiary molasse depressions in the basins along the Struma River. West of this line, the rocks have the different properties and are described as the Serbian--Macedonian metamorphic series in Greece (Birk et al., 1970). The directions of the induction vectors fix this boundary by the sharp change in their directions.

The position of the *northern boundary* of the nappe is expected to occur in the zone of Sredna Gora. The southeasterly striking Asenovograd--Dyadovo (AD) fault is presumed to be the boundary band of the CERM allochthon. To a certain extent, this is reflected in the parameters of the EM field in Fig. 4.

The *eastern boundary* of the nappe is covered by the thick strata of the Paleogenic molasses. Its surface is masked by the thick (>500 m) zone of slickenside diaphthoretic rocks. (Ivanov R., 1981). The strikingly pronounced gravimetric transition from the light masses of the CERM allochthon to the significantly heavier SERM masses is interpreted as the geophysical "Central Rhodope Deep Fault" (RF), which is probably the geological boundary between the different rocks of the blocks of the Central Rhodope autochthon nappe. This region is marked by the profound folding, diaphthoresis, and milinitization of the NNE zone with the thick serpentite layers at the CERM and SERM boundary-- the Snezhin synclinorium.

The position of this fault spatially corresponds to the sharp changes in the parameters of the EM field at almost all the periods of the amplitudes and directions.

The nature of the conductive layer in the Rhodope

The high-conductivity anomaly revealed in the western part of the studied territory is likely to be induced by the fluids ascending from the lithospheric plates which subside towards the southern portions of the Serbian-Macedonian and Rhodope massif. This geoelectrical structure of fluid--thermal origin is correlated to the low-velocity seismic structure (Fig. 2).

As noted above, the waveguide which is identified from seismic data in the upper portions of the crust at a depth of 5--10 km is associated with the thick buried sedimentary rocks in this part of the region. In the opinion of the Bulgarian geologists (Ivanov, Stanev, 1982), the autochthon in this thrust is formed by the thick marble layer which is treated by the hydrogeologists as a large, deeply seated artesian basin with hydrothermal karst. The allochthon composed of the Rhodope granitoid series serves as the water-resistant confining plate.

These scientists suggested the paleohydrogeologic approach based on studying the hydrothermal systems in the active volcanic area and substantiated the thermo-elision model of polymetallic metallogeny in Rhodope. This model can explain the origin of the conductivity anomaly revealed beneath the Rhodope.

An important fact is that during the Tertiary period, the Rhodope aquifer was a carrier of hydrothermal brines which penetrated into the Rhodope confining plate and formed the metasomatic tin -- zinc ore mineralization (the Erma River deposit).

Interestingly, the region of the increased crustal conductivity also quite accurately coincides in plan with the negative lithospheric anomaly of the constant magnetic field established from the CHAMP satellite data, which suggests the elevation of the Curie

surface, and with the change in the sign of the lithospheric magnetic field in the region of the Central Rhodope deep thrust (see the paper: "Lithospheric magnetic anomalies in the Balkan region" in this Journal).

Conclusion

From the presented data it can be seen that the MV parameters quite adequately reflect the tectonic features of the Rhodope region.

The analysis of the EM data quite confidently suggests the presence of the buried crustal conductor beneath the western part of the Rhodope massif. The parameters of the EM field reflect the spatial distribution of the Central-Rhodope massif and the Central-Rhodope deep fault zone.

The Rhodope hydrothermal basin can be treated as the source and cause of the unique geoelectrical anomaly in the south Bulgaria.

The further interpretation of the revealed crustal geoelectrical anomalies with the allowance for the seismic velocity models, seismological data, geothermal reconstructions, potential field anomalies, geochemical and petrophysical notions, as well as the other geological and geophysical information will clarify the origin of these anomalies and elucidate their relationship with the geodynamical processes.

The modern interpretation technologies that have been developed in the world to date make it possible to build the volumetric geological models on different scales which could be of practical value for mineral prospecting, hydrogeological and hydrothermal resources evaluation, and seismicity assessment in the territory of Bulgaria.

References

- Abramova L., Iv. Varentsov, A. Velez, R. Gavrilov, N. Golubev, M. Zhdanov, E. Martanus, E. Sokolova, V. Shneyer, 1994. Study of deep geoelectrical structure in Bulgaria, (In Russian), *FIZIKA ZEMLI*, № 11, 59-69.
- Ashirova N.G., Berdichevski M.N., Dubrovski V.G., 1981. The stochastic model of the magnetotelluric process in the long-period variations range, (In Russian), *FIZIKA ZEMLI*, № 10, 69-76.
- Birk, F., 1970. Zur Geologie des Rhodopen-Kristallins in Gebiet zwischen Strimon und Nestos (Griechisch- Ostmazedonien), (in German), 179 pp., Beih.Geol.Jb., Hannover.
- Dachev Khr., 1988. Structure of the Earth crust in Bulgaria, (In Bulgarian), 334 pp., Technique, Sofia.
- Dachev, Khr., I. Volvovsky, 1985. Deep structure of Bulgaria along the Petrich- Nikopol EMCM - DSS traverse, *Bollettino di Geofisika Teorica ed Applicata*, XXVII, N. 108, 263- 278.
- Gough, D.I. and Ingham, M.R., 1983. Interpretation methods for magnetometric arrays. *Rev. Geophys. Space Phys.*, 21, 805-827.
- Iosifov D., Iv Zagorchev, Iv. Boyanov, 1994. The lithosphere of the Central and East Europe. Balkan, edited by A. V Chekunov, 161-173, Naukova dumka, Kiev, Ukraine.
- Iovka Borisova. The map of the total longitudinal conductance of sediments S₃ Private report.
- Ivanov R., 1981. The deep-seated Central-Rhodope Nappe and the interference tectonics of the Rhodope crystalline basement, *Geologica Balcanica*, 11, N 3, 47-66.

- Ivanov R., Iv. Stanev, 1982. Paleohydrogeologic relations between Genesis of polymetallic ore deposits and volcanism in Rhodope Mountains, Review of the Bulgarian geological society, 43, 61-74.
- Ivanov, R., 1984. Rhodope Deep Trust: Two Different Approaches to New Facts. *Geologica Balcanica*, 14, 89-91.
- Ivanov, Zh., 1984. Geological Structure of the Central Rhodope Range, *Geologica Balcanica*, 14, 3-43.
- Kutas, R., 1978. Heat flow field and thermal model of the Earth's crust. (In Russian), 140 pp., Naukova dumka, Kiev.
- Macris J. 1977. Geophysical Investigation of Hellenides. *Hamb.: Geophys. Einzelschriften*. Ser. A, V. 34. 123 p.
- Schmucker, U., 1970. Anomalies of geomagnetic variations in the southwestern United State, *Bull. Scripps Inst. Oceanogr.*, 13, 165 pp.
- Shchukin, Yu.K., 2005. Problems of deep-level geology in regional geophysical studies, (In Russian), in: Second All-Russ. Workshop on Electromagnetic Soundings of the Earth (Moscow, 28–30 November 2005), MAKS PRESS, Moscow, 21–30.
- Spakman W., Wortel M.R. and Vlaar N., 1988. The Hellenic subduction zone: a tomographic image and its geodynamic implications, *Geophys. Res. Lett.*, 15, № 1, 60-63.
- Varentsov Iv., 2013. The Software system PRC_MTMV for the synchronous soundings data processing, (In Russian), in: Materials of the VI All-Russ. Berdichevski and Vanyan Workshop on EM soundings of the Earth, INGG SO RAN, Novosibirsk, 1-4.
- Velchev Ts., Dachev, Khr., Petkov Iv., 1970. Geotectonic structure of Bulgaria in the light of the geophysical fields, (In Russian), *Rep. BAN*, 23, (6), 699-702.
- Velinov T., Boyadjieva K., 1981. Geothermal investigations in Bulgaria, (in Bulgarian), 154 pp., Sophia, Teknika,
- Volvovsky I, Dachev Khr., O. Popova et al., 1987. Earth's crust of the Bulgaria, (In Russian). 110 pp., Geophysical Committee, MMoscow.
- Zagorchev, I. 2001. Geology of SW Bulgaria: an overview. – *Geologica Balcanica*, 21, 1-2; 3-52.
- Zhdanov M., Abramova L., Iv. Varentsov, A. Velev, E. Martanus, 1990, Deep electromagnetic soundings on Bulgaria territory, *DAN SSR*, 312, 6, 1338-1343.

Връзката между електромагнитните параметри и тектонски структури на територията на България

Л. Абрамова, Ив. Варенцов, Д. Абрамова

Резултатите от магнитовариационните (MV) изследвания на територията на България са представени в статията. Изчислени са функциите на електропроводността и магнитните индукционните вектори. Построени са върху тях карти на модул и посоката на индукционните вектори. Сравнението на тези карти с тектонската структура на района на Родопския масив показва, че параметрите MV адекватно отразяват тектонските характеристики на региона на Родопите.

MODELLING OF DECLINATION'S SECULAR VARIATION FOR THE PURPOSES OF REGIONAL TOPOGRAPHIC MAPPING

M. Metodiev

Dept. of Geophysics, National Institute of Geophysics, Geodesy and Geography-BAS, Acad. G. Bonchev Str., Bl.3, 1113 Sofia, Bulgaria, m.i.metodiev@gmail.com

Abstract. The most significant of the Earth's magnetic field elements is the geomagnetic declination, which is widely used in geodesy, cartography and their associated navigational systems. The geomagnetic declination is incorporated in the naval navigation maps and is used in the navigation process. It is also a very important factor for aviation where declination data have major importance for every airport (civil or military).

As the geomagnetic field changes with time but maps of the geomagnetic declination are not published annually and are reduced to an epoch in the past (Buchvarov and Cholakov, 1985), it is necessary to define two additional parameters in the maps, needed to determine the value of the geomagnetic declination for a particular moment in the future: 1) estimated value of the annual declination variation and 2) a table with the average diurnal variation of the declination for a given month and hour.

Key words: PAG observatory, geomagnetic declination, geomagnetic secular variations, prediction models..

Introduction

The goal of this research is to analyze the annual mean values of geomagnetic declination on the territory of the Balkan Peninsula for obtaining a best fitting model of that parameter which can be used for prediction of the declination value for the next 10 years (Mandea, 2001).

The latest version of the GFZ Reference Internal Magnetic Model (GRIMM-3.0) was used to compare the magnetic field evolution predicted by that model between 2001 and 2010 to the data collected in five operating geomagnetic observatories in the Balkan region (PAG, SUA, PEG, IZN, GCK) over the same time interval.

In this study are tested different time-scale periods and different order polynomials to create the most appropriate prediction model and to estimate the obtained results. It is perceived that linear models which are used to determine the annual declination variation in

cartography provide enough accurate information for the declination map's users.

Datasets used in the research

1. Model derived from satellite data: The GFZ Reference Internal Magnetic Model (GRIMM) has been derived from nearly eight years of CHAMP satellite data and seven years of observatory hourly means. At high latitudes, full vector satellite data are used at all local times. By doing so, a separation is possible between, on one hand, the fields generated by the ionosphere and field aligned currents, and, on the other hand, the fields generated in the Earth's core and lithosphere. This selection technique leads to a data set where gaps are avoided during the polar summers allowing the modeling of the core field with an unprecedented time resolution.

2. Secular data from several INTERMAGNET observatories near to PAG observatory: The observatories used (Fig.1) for the second dataset are located on the Balkan Peninsula or in near vicinity (Iznik). Annual mean values of the declination are used from:

Grocka, Serbia and Montenegro (GCK) -	Latitude = 44° 38'	Longitude = 20° 46'
Surlari, Romania (SUA) -	Latitude = 44° 41'	Longitude = 26° 15'
Pedeli, Nea Makri, Greece (PEG) -	Latitude = 38° 5'	Longitude = 23° 56'
Iznik, Turkey (IZN) -	Latitude = 40° 30'	Longitude = 29° 44'
Panagyurishte, Bulgaria (PAG) -	Latitude = 42° 31'	Longitude = 24° 11'

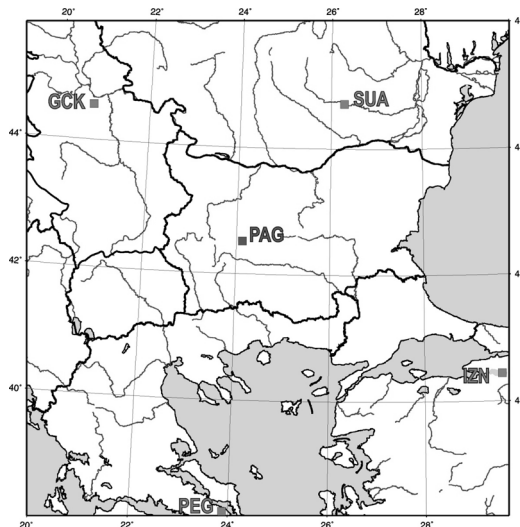


Fig.1. Locations of the observatories which data are used for modelling

3. Bulgarian repeat stations network data: The repeat stations measurements in Bulgaria started in 1934. The eight points selected then were supplemented with seven more in 1964.

All points were investigated, stabilized and later duplicated with spare ones and secured with lasting miras. Up to 1980 they were measured every three years and then because of the small secular variations – every five years. Isoporic maps for different periods are elaborated. The repeat stations are shown on the map in Fig.2. Last series of geomagnetic field measurements were performed during 2007 and 2012 using Di-Flux (theodolite Zeiss 020B and Mag-01H) and GSM-19 proton magnetometer.

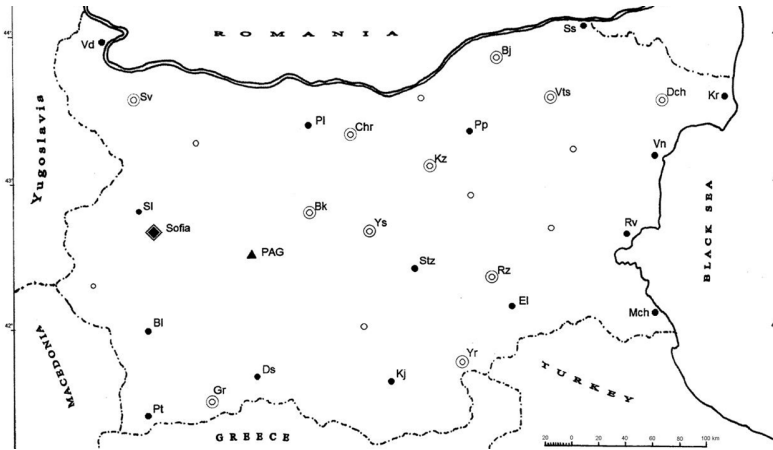


Fig.2. Location of the repeat stations in Bulgaria

▲ - Panagyurishte observatory; ● - repeat stations; ⊙ - first class points ; ○ - new points.

Model Derived From Satellite Data

The latest version of the GFZ Reference Internal Magnetic Model (GRIMM-3.0) is used to extract the magnetic field secular variations predicted by that model between 2007 and 2012 and to compare them to the data registered in the Balkan Peninsula observatories and the repeat station measurements on the Bulgarian territory. GRIMM-3.0 model is to provide a highly accurate description of the core field and its temporal evolution, the model contains some external field estimates as a by-product from the necessary separation of sources in the modeling approach (Korte and Lesur, 2012). Using linear interpolation we created model of the annual variation of the Declination in a window from Lat. 41,2°N to Lat. 44.2°N and form Long. 22°E to Long 28°E (Fig. 3)

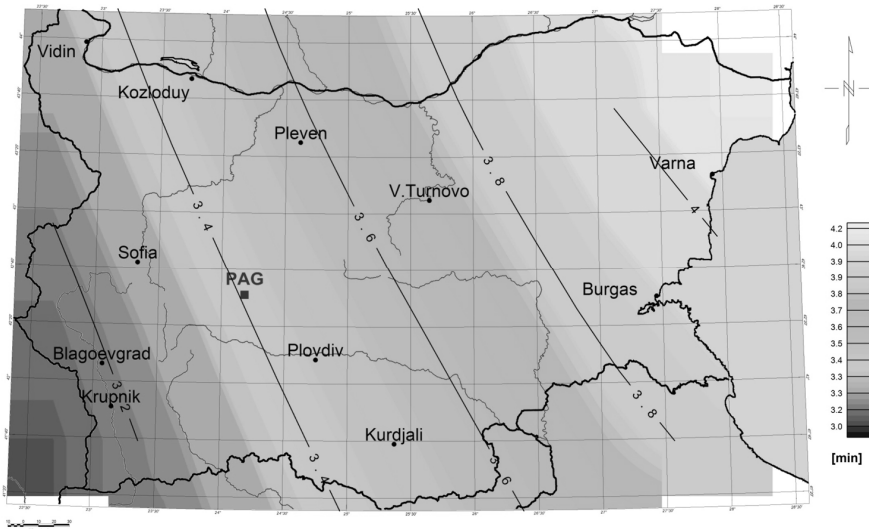


Fig.3. Model of the Declination annual variation for the territory of Bulgaria obtained from GRIMM-3.0 model for the period 2007-2012

Model Derived From Observatory Data

Published annual mean values of the Declination obtained in Panagyurishte observatory (PAG) (Butchvarov and Cholakov, 2006; Cholakov and Mihovski, 2010) and the four neighboring geomagnetic observatories (SUA, IZN, PEG and GCK) were used for the periods as follows:

PAG – 2000-2012
IZN – 2007-2012

SUA – 2000-2010
PEG – 2000-2012
GCK – 2000-2011

Model of the Declination annual variation is obtained by linear fit using least squares method. Obtained values are in the range 4.9 to 5.8 min per year (Fig. 4). Due to the fact that the observatories used for modeling are far away from Bulgarian territory, after the interpolation there are some features that cannot be explained with the expected main field characteristics presented in isoporic maps of previous researches.

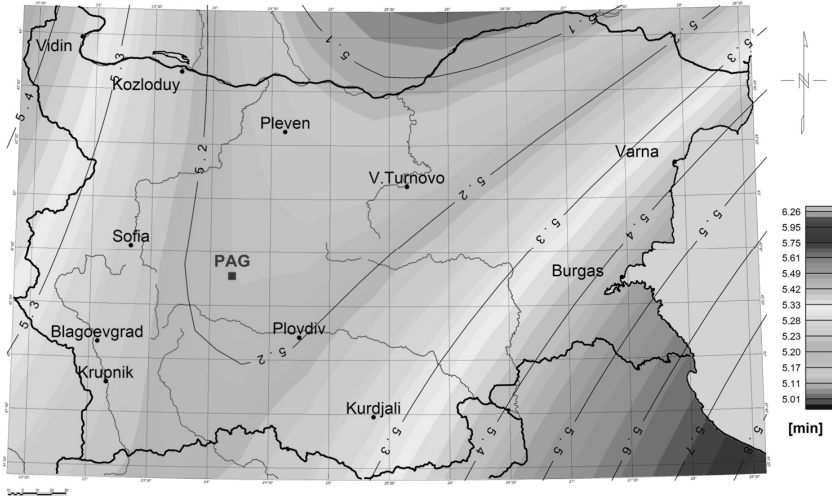


Fig.4. Model of the Declination annual variation for the territory of Bulgaria obtained from Declination annual mean values calculated in PAG, SUA, IZN, PEG and GCK observatories.

Model Derived from Repeat Station Measurement Data

The Geomagnetic Survey in the National Institute of Geophysics, Geodesy and Geography-BAS has reliable data for the declination registered in Geomagnetic Observatory Panagyurishte (PAG) since 1948 to now (Fig. 5). The existence of such a long row of data allows tests on secular variations of the magnetic field, to track dependencies related to various cycles of solar activity, as well as to make estimates of the annual change of declination for small periods in the future.

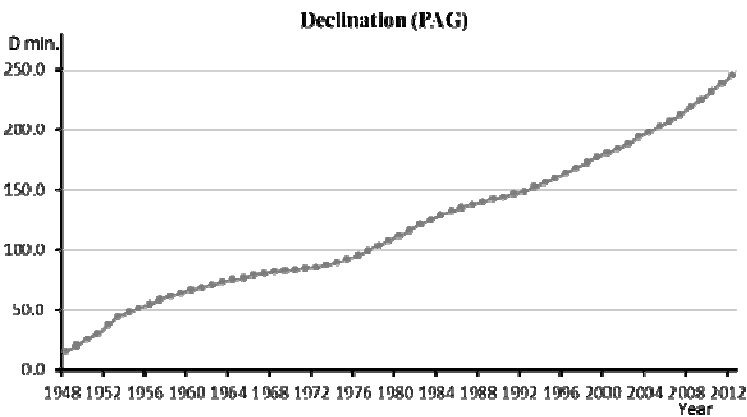


Fig.5. Annual Declination values obtained in PAG since 1948

Analysis of the Declination values, registered in the last 65 years in PAG indicates that the value of this element increases but with a different rate, thereby the annual variation is variable over time (Fig. 6). Several intervals of increase are observed, followed by a gradual decline in values, but in general from the plot of declination first derivative for the entire data a positive linear trend in the range of 1.5 min/year is calculated. Mathematical analysis of the behavior of geomagnetic declination and its first and second derivatives showed that for modeling the values of this parameter with extrapolation is appropriate to use data recorded after 2000.

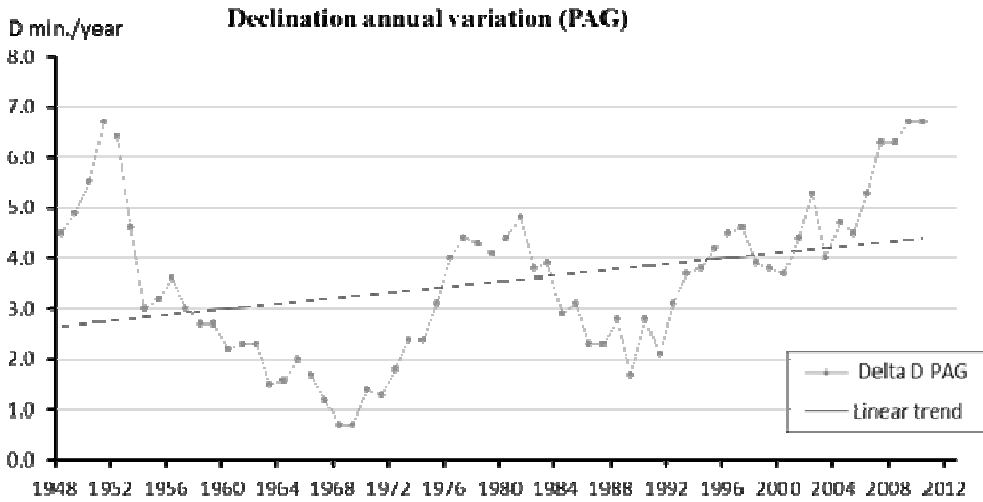


Fig.6. Declination Annual Variation in PAG observatory and calculated linear trend since 1948

For prediction of the Declination annual variation for the next 10 years data from PAG (Fig. 7), SUA, IZN, PEG, GCK and 6 repeat stations from Bulgarian territory are used. Regression analysis of each data series of the declination values is performed with a linear model using the least squares technique:

$$D(t)=D_0 + \Delta D.t$$

Where $D(t)$ is the Declination, D_0 is constant component of the equation, t is time in years and ΔD is the linear variation for the investigated period which is used as a prediction value of declination annual variation.

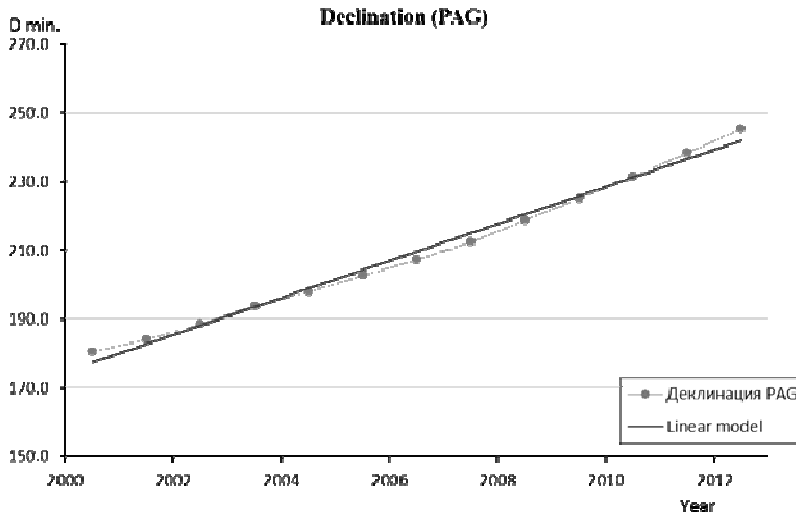


Fig.7. Linear model of the Annual Declination using least squares technique for the period 2000-2012

Calculated values are in the range between 5 and 5.5 min./year and a distinct W-E trend is observed on the map of Fig. 8.

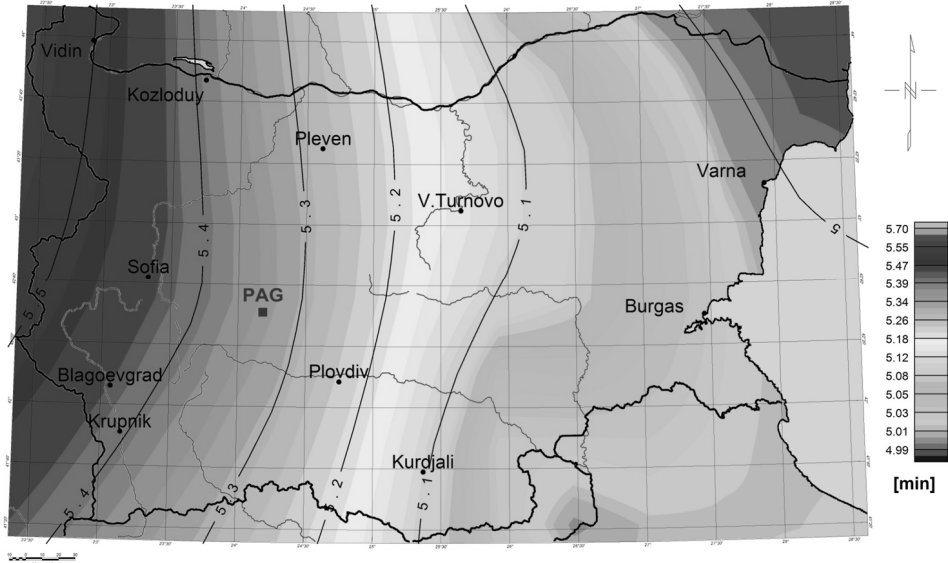


Fig. 8. Prediction model of the Annual Declination variation for the period 2013-2023 for the purposes of regional topographic mapping

The obtained results are comparable with the research done by Georgiev et al where the annual declination model has a similar configuration but the obtained values for the period 1960-1980 are in the range 1.4-2.7 min./year. Calculated in this way prognostic

values of the Annual Declination variation can be used in the topographic maps and for navigation.

Conclusions

Three different models are obtained aiming to predict the Annual Declination variation for the next ten years over the territory of Bulgaria. Satellite data from GRIMM 3.0 show only the long-wavelength components of the global geomagnetic changes which are not sufficient to present the local behaviour of the geomagnetic field secular variations with an accuracy which can be used for topographic mapping. Regional interpretations made by observatory data only provide more detailed representation of the investigated element. They have one main disadvantage which is the lack of data in long and equal time intervals. This was compensated by constraining the model using repeat station measurements in Bulgaria. As a result, a model of the Annual Declination variation is obtained having accuracy and resolution which is sufficient for the purposes of calculating the geomagnetic declination for a particular moment in the future and can be used in topography maps.

Acknowledgments I would like to thank Dr. Ivan Buchvarov for the archive materials from PAG observatory activities in the past and for the useful help for analyzing the obtained results.

References

- Buchvarov, I., Cholakov, I., (1985): Reducing the absolute measurements of the components of Earth's magnetic field to a common epoch using a basic point and a field magnetic variation station. *Bulgarian Geophysical Journal* Vol XI No 1.
- Butchvarov, I., Cholakov, I. (2006): Field and observatory geomagnetic measurements in Bulgaria, NATO, Geomagnetism for aeronautical safety, The Netherlands.
- Cholakov, I., Mihovski, S. (2010): Magnetic repeat station survey of Bulgaria in 2007 and 2008. *Bulgarian Geophysical Journal* Vol 36.
- Georgiev, Chr., Kostov, K., Cholakov, I. (1986): Isopors of Declination in Bulgaria for the Period 1940-1980, *Bulgarian Geophysical Journal* Vol XII No 3.
- Korte, M., Lesur, V. (2012): Repeat station data compared to a global geomagnetic field model. *Annals of Geophysics*, 55, 6, p. 1101-1111.
- Mandea, M. (2001): How well is the main-field secular variation known?, *Contributions to geophysics and geodesy*, Geophysical institute, Slovak Academy of Science, v. 31, № 1.

Моделиране на секуларната вариация на геомагнитната деклинация за целите на регионалното топографско картиране

М. Методиев

От елементите на земното магнитно поле, най-значимия е геомагнитната деклинация. Тя се използва в геодезията, картографията и свързаните с тях навигационни системи. Деклинацията е интегрирана в морските навигационни карти и се използва при процеса на навигация. Също така е много важен фактор за авиацията, където данните за деклинацията са от голямо значение за всяко летище.

Тъй като геомагнитното поле се променя във времето, но карти на геомагнитната деклинация не се публикуват ежегодно и биват редуцирани към епоха в миналото, е необходимо да се дефинират два допълнителни параметъра в картите, нужни за определянето на геомагнитната деклинация за даден момент в бъдещето: 1) изчислена стойност на годишната вариация на деклинацията и 2) таблица със средните денонощни вариации за даден месец и час.

POSSIBILITY FOR DROUGHT ASSESSMENT WITH GRIDDED DATA-SETS OF THE STANDARDIZED PRECIPITATION INDEX

H. Chervenkov, I. Tsonevsky, K. Slavov

National Institute of Meteorology and Hydrology, blvd Tsarigradsko Shose 66, Sofia 1784, Bulgaria,
e-mail: hr isto.tchervenkov@meteo.bg

Abstract. Drought Indices (DIs) have been commonly used to define drought conditions. In general, DI is a function of several hydro-meteorological variables and can be integrated in a decision support system as a drought management tool to trigger drought relief programs. Globally, droughts have been studied using many different indicators, but, among them, the Standardized Precipitation Index (SPI) has significant advantages. SPI has been selected by the World Meteorological Organization (WMO) as a key indicator for monitoring drought ('Lincoln declaration') and is one from the two most used in Europe. The obtained from the authors' four global gridded data-sets of the SPI are presented. They are computed from the UDEL/GEOG/CCR v3.02, GPCC v7.0, the NOAA-CIRES 20CR v2c and the ECMWF ERA20C monthly precipitation databases and each of them is with more than a century long time extent. The SPI is calculated for the most frequently used time scales of 1, 3, 6, and 12 months and, except ECMWF ERA20C, are in the highest available grid resolution, native for the precipitation database. The popularity of the SPI in the geophysical community and the strong conviction of the authors that the free exchange of data and software services are basis of effective scientific collaboration, are the main motivators to open the produced data-sets for free of charge download. The paper shows also in concise form some possible use of this information, revealing its suitability for various objective long-term drought studies at any geographical position.

Key words: Global Gridded Data-sets of SPI, Objective Drought Assessment, Free SPI-data Download

Introduction

Drought is a natural phenomenon and poses significant problems around the world. It places huge demands on rural and urban water resources, and enormous burdens on agricultural and energy production. In general, drought is defined as the water scarceness due to insufficient precipitation, high evapotranspiration and over-exploitation

of water resources or a combination of these parameters. Despite its complex nature, there is overall agreement that precipitation is the primary factor controlling the formation and persistence of drought conditions. Drought indices (DIs) have been commonly used to define drought events. In general, DI is a function of several hydro-meteorological variables (e.g., rainfall, temperature, streamflow, snowmelt, etc.). They can be integrated in a decision support system as a drought management tool to trigger drought relief programs. Moreover, it has been used to quantify deficits in water resources and as a drought monitoring tool. However, drought researchers are confronted with the ambiguity of drought definitions and DIs, which has never been resolved to the satisfaction of all drought researchers and professionals. In attempt to overcome this, an Inter-Regional Workshop on Indices and Early Warning Systems for Drought was held at the University of Nebraska-Lincoln in December, 2009. It was jointly sponsored by the School of Natural Resources of the University of Nebraska, the U.S. National Drought Mitigation Center, the World Meteorological Organization (WMO), the U.S. National Oceanic and Atmospheric Administration (NOAA), the U.S. Department of Agriculture (USDA), and the United Nations Convention to Combat Desertification (UNCCD). The workshop reviewed the drought indices currently in use in different regions of the world to explain meteorological, agricultural and hydrological droughts, assessed the capacity for collecting information on the impacts of drought, reviewed the current and emerging technologies for drought monitoring and discussed the need for consensus standard indices for describing different types of droughts. Manifestation of the results of the conference is the Lincoln declaration (Hayes et al. (2011)), which key point is that the workshop came to a consensus that the Standardized Precipitation Index (SPI) be used to characterize the meteorological droughts around the world. More specially, the National Meteorological and Hydrological Services (NMHSs) around the world are encouraged to use the SPI to characterize meteorological droughts and provide this information on their websites, in addition to the indices currently in use. The free availability in the recent decades of digital maps for the monthly precipitation sums, either from objective analysis or from reanalysis, has encouraged the authors to compute the SPI for the frequently used time scales of 1, 3, 6, and 12 months (noted traditionally as SPI-1, SPI-3, SPI-6 and SPI-12) from four sources for the full time length of each precipitation data-set. Consequently, following our strong conviction that the free exchange of data and software services are basis of effective scientific collaboration, we offer these results for free of charge download via Internet. Mean aim of this study is to present shortly these data-sets, rather than to perform any drought climatology. Thus, the listed examples have to be treated as small illustration of the variety of potential applications at any possible geographical position, depending of the particular interest of each end-user.

The paper is organized as follows: Section 2 provides a description its strengths, limitations and application of the SPI for objective drought assessment. The third section contains concise description of the used precipitation data-sets. The performed calculations, validation of the output are in the fourth section. The procedure for the free of charge download of the output data-sets is described in the fifth. In the sixth section are listed some illustrative examples and the short summary and conclusion are placed in the last, seventh section.

Theoretical aspects, strengths and limitations of the SPI

The SPI was developed by McKee et al. (1993) for monitoring drought conditions based on precipitation sums. It is computed by fitting a cumulative probability function (CPF) to the distribution of precipitation summed over the time scale of interest. This is performed separately for each month (or whatever the temporal basis (time window) is of the raw precipitation time series) and for each location in space.

The definition of the SPI is part of many publications, and thus will be not addressed here. The reader can find it, for example, in Lloyd-Hughes and Saunders (2002). Once standardized, the strength of the anomaly is classified as set out in Table 1. The table also contains the corresponding probabilities of occurrence of each severity, these arising naturally from the normal probability density function.

SPI value	Category	Probability %
2.00 or more	Extremely wet	2.3
1.50 to 1.99	Severely wet	4.4
1.00 to 1.49	Moderately wet	9.2
0 to 0.99	Mildly wet	34.1
0 to -0.99	Mild drought	34.1
-1.00 to -1.49	Moderate drought	9.2
-1.50 to -1.99	Severe drought	4.4
-2 or less	Extreme drought	2.3

Table 1. Values of SPI and corresponding categories and probabilities (after Lloyd-Hughes and Saunders (2002))

In the recent decade the SPI is widely used throughout the world in both a research and an operational mode (see Lloyd-Hughes and Saunders (2002) for details).

In many articles (see, for instance, Hayes et al. (1999)) the advantages and disadvantages of using the SPI for drought severity assessment are discussed. The SPI has three main advantages. The first and primary advantage is simplicity. The SPI is based solely on rainfall and requires only the computation of two parameters, compared with the 68 computational terms needed to describe the popular Palmer drought severity index (PDSI). By avoiding dependence on soil moisture conditions, the SPI can be used effectively in the whole year. The SPI is also not affected adversely by topography. The SPI's second advantage is its variable time scale, which allows it to describe drought conditions important for a range of meteorological, agricultural, and hydrological applications as in the cited articles above. This temporal versatility is also helpful for the analysis of drought dynamics, especially the determination of onset and cessation, which have always been difficult to track with other indices. The third advantage comes from its standardization, which ensures that the frequencies of extreme events at any location and on any time scale are consistent. Other strength, usually dismissed in the SPI description, is that this index is defined without any empiricism, in particular 'local parameterizations', which, more or less, are connected to the concrete position and/or data-set. This problem arises also in the attempts to generalize the SPI, including the evapotranspiration (see Vicente-Serrano

(2012)). The SPI has three potential disadvantages, the first being the assumption that a suitable theoretical probability distribution can be found to model the raw precipitation data prior to standardization. An associated problem is the quantity and reliability of the data used to fit the distribution. A second limitation of the SPI arises from the standardized nature of the index itself; namely that extreme droughts (or any other drought threshold) measured by the SPI, when considered over a long time period, will occur with the same frequency at all locations. Thus, the SPI is not capable of identifying regions that may be more 'drought prone' than others. A third problem may arise when applying the SPI at short time scales (1, 2, or 3 months) to regions of low seasonal precipitation. Strictly speaking, the SPI is not defined by zero precipitation. In these cases, misleadingly large positive or negative SPI values may result. On this problem partly is dedicated the work of Wu et al (2012). On the basis of the results identified within this study, the authors recommend that the SPI user be cautious when applying short-time-scale SPIs in arid climatic regimes, and interpret the SPI values appropriately.

Used data

In the recent decades objective analysis and reanalysis have been extensively developed in many institutions and, consequently, the produced data-sets used in many applications. In our study we have used two objective analysis data-sets, namely the version 3.02 of the "Terrestrial Precipitation: 1900-2010 Gridded Monthly Time Series" of the Department of Geography of the University of Delaware (Peterson et al (1998)), noted further as UDEL and the Global Precipitation Climatology Centre (GPCC) Full Data Reanalysis version 7.0 (Schneider et al (2015)), noted as GPCC. The both are global and the subsets with the highest resolution of $0.5^{\circ} \times 0.5^{\circ}$ for both are considered for the SPI-calculation. The time extent of UDEL is 1900-2010 and of GPCC - 1901-2013. The considered reanalysis data-sets are the version v2c of the NOAA-CIRES 20CR (Compo et al. (2011)) noted as CIRES and ERA20C of the European Centre for Medium-Range Weather Forecasts (ECMWF) noted further as ERA20C (Stickler et al (2014)). These data-sets are also global with time coverage 1851-2011 and 1900-2010 correspondingly. The raw data of CIRES are in Gaussian irregular grid and are interpolated with the tool "cdo" (<http://www.mpimet.mpg.de/cdo>) to the $1.5^{\circ} \times 1.5^{\circ}$ resolution with similar to the original grid cell size. So, one CIRES gridcell accommodate nine UDEL or GPCC ones. The ERA20C data-set is deliberately downloaded with $0.5^{\circ} \times 0.5^{\circ}$ resolution although the grid-cell centers are offset by 0.25 deg in comparison to UDEL and GPCC.

Performed calculations and validation

The values of SPI-1, SPI-3, SPI-6 and SPI-12 are computed using own programs, following the classical approach, proposed by McKee et al. (1993). The calculations are performed over the whole spatial and temporal extent of each input data-set, described in previous section.

The web site of the CARPATCLIM project (see JRC report (2010) and the references therein) contains data for monthly precipitation sums and the calculated with them SPI and thus are suitable for validation of our calculation procedures. The two computations were found to be in excellent agreement. The European Drought Observatory of the Joint Research Centre (EDO-JRC, <http://edo.jrc.ec.europa.eu/edov2/php/index.php?id=1000>) publishes also SPI maps of recent drought episodes. Although computed with SYNOP data and different reference period they are very close to our results.

The selection of the reference period for the calculation of the CPF parameters is usually not commented with necessary depth, but, this is very relevant. McKee et al. (1993) recommends to use time-series with at least 30 years length and thus the current WMO standard reference period 1961-1990 seems the most natural choice. Considering the results of an inventory of the reference periods used in various Member States, the specific needs for accurately representing extreme events, and possible changes in the rainfall regimes due to climate change, the Water Scarcity and Drought Expert Group strongly recommends using the period January 1971 to December 2010 as Reference Period for the calculation of the SPI.

Illustrative examples and qualitative comparisons

Main result from the presented work are the spatial and temporal arrays of the fourth SPIs, retaining the spatial and temporal extent/resolution of the corresponding input precipitation data-set. Such distribution facilitates the combined analysis of both in parallel. Hence each map, drawn after interpolation of unstructured data, for instance the point measurements in the SYNOP stations as in the work of Karavitis et al (2011), depends from the subjective choice of the interpolation procedure, the presented here in the 'native' regular grid data-sets are much more consistent.

As far as any drought climatology is beyond the scope of the presented work, only some illustrative examples, which reveals possible implementations of the data-sets, will be listed concisely.

Thus Figure 1 shows the world map of the SPI-12 for the second year of the NOAA-CIRES reanalysis.

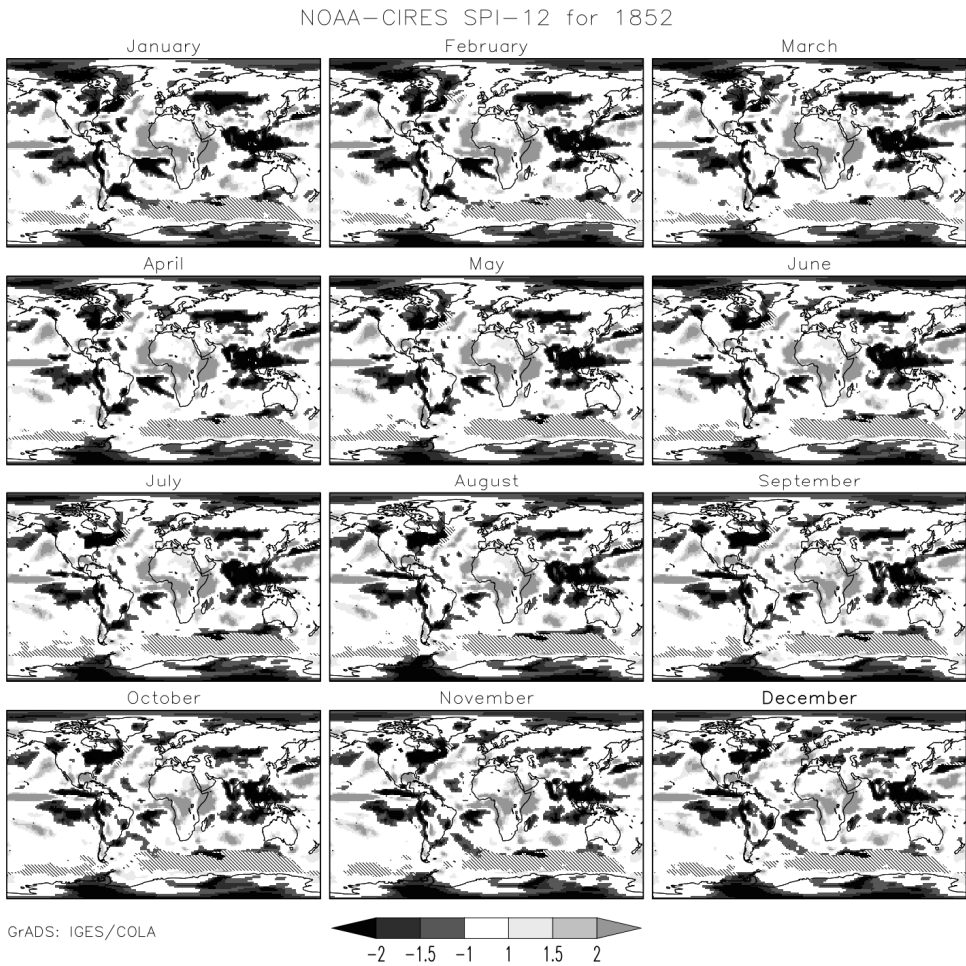


Fig. 1. World map of the SPI-12 for the second year of the NOAA-CIRES reanalysis

The drought in the USA during 1976 and 1977 was well expressed, especially in particular regions; California's statewide snowpack reached an all-time low in 1977. The spatial distribution of the SPI-6 for North America for this year is depicted on Figure 2.

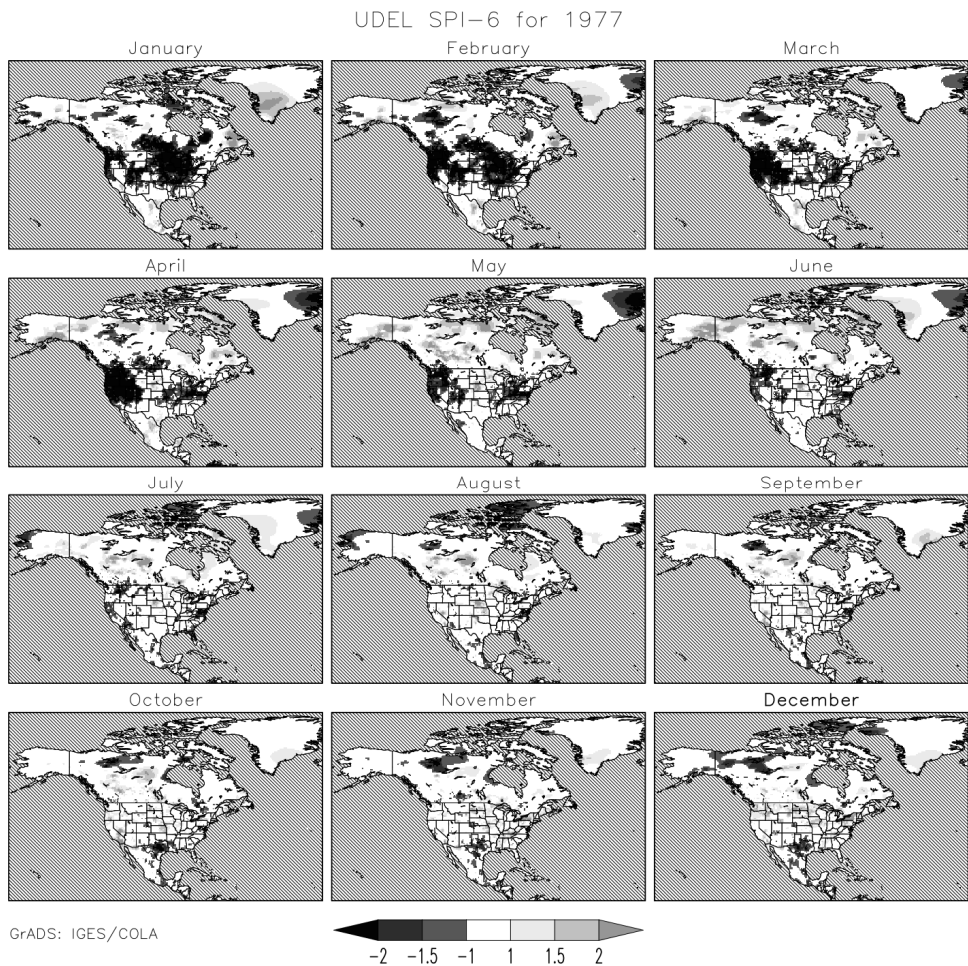


Fig. 2. Map of the SPI-6 for 1977 obtained from UDEL. Hence this dataset contains data for the land-surface only, the SPIs over the water bodies are undefined and shown hatched.

The extreme drought and heat wave that hit Europe in the summer of 2003 had enormous adverse social, economic and environmental effects, such as the death of thousands of vulnerable elderly people, the destruction of large areas of forests by fire, and effects on water ecosystems and glaciers. It caused power cuts and transport restrictions and a decreased agricultural production. According to the on-line document (http://www.unisdr.org/files/1145_ewheatwave.en.pdf) “Impacts of summer 2003 heat wave in Europe” of the United Nations Environment Programme (UNEP) the losses are estimated to exceed 13 billion euros. Map for SPI-3 for this episode is shown on Figure 3.

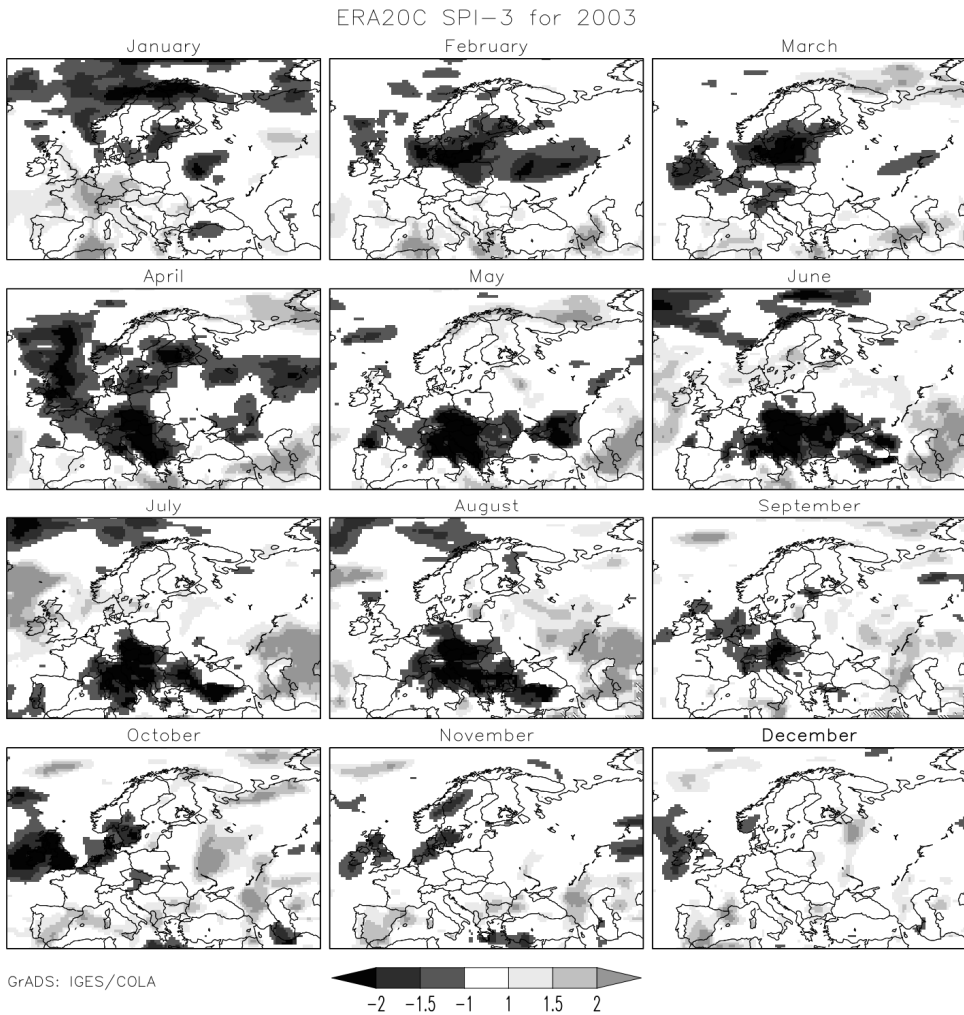


Fig. 3. Map of the SPI-3 for 2003 obtained from ERA20C

Typical issue of the long-term drought climatology is the analysis of historical drought events. So, for instance, the EDO-JRC maintains drought episodes site, which is updated periodically. Impressive is the case in 1989-1991 in Europe, which, according this source is in the list of 21 biggest droughts since 1950. Especially affected were Southern Europe and the Mediterranean. Figure 4 shows the spatial distribution of the SPI-1 in the middle year, 1990 for Southeast Europe.

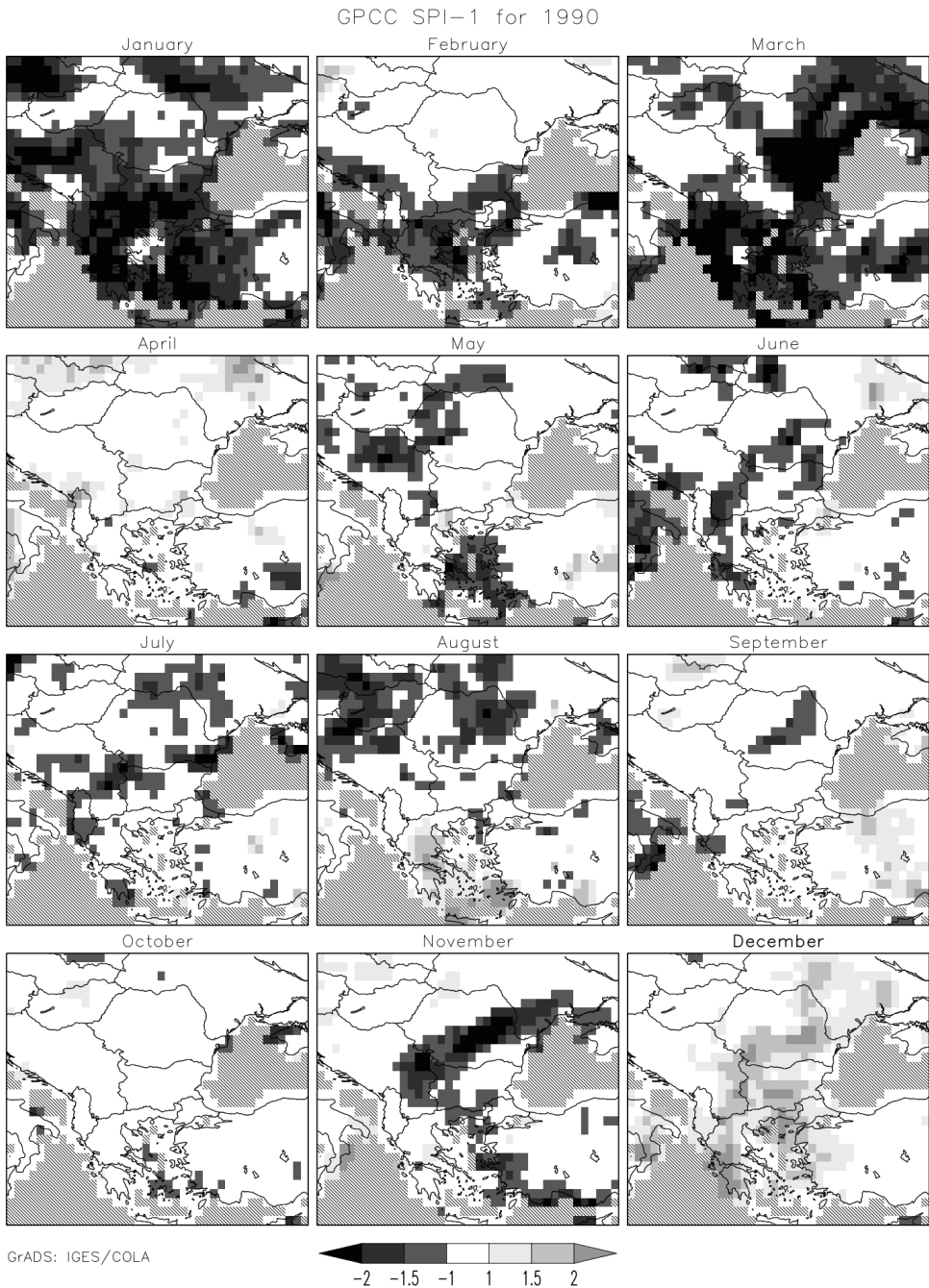


Fig. 4. Map of the SPI-3 for 2003 obtained from GPCC. This data-set contains data also for the land-surface only.

The obtained data-sets can be post-processed statistically in order to derive some secondary measures, which are suitable for climatological analysis. So, for instance, Lloyd-Hughes and Saunders (2002) shows, among other results, maps of the number of drought events, where the individual ones are defined by zero crossings that bound the exceedance. Finally, the presented data-sets offers the possibility to extract certain information in particular (grid) point of interest in form of time series, which is other traditional way for data analysis and visualization, as shown on Figure 5.

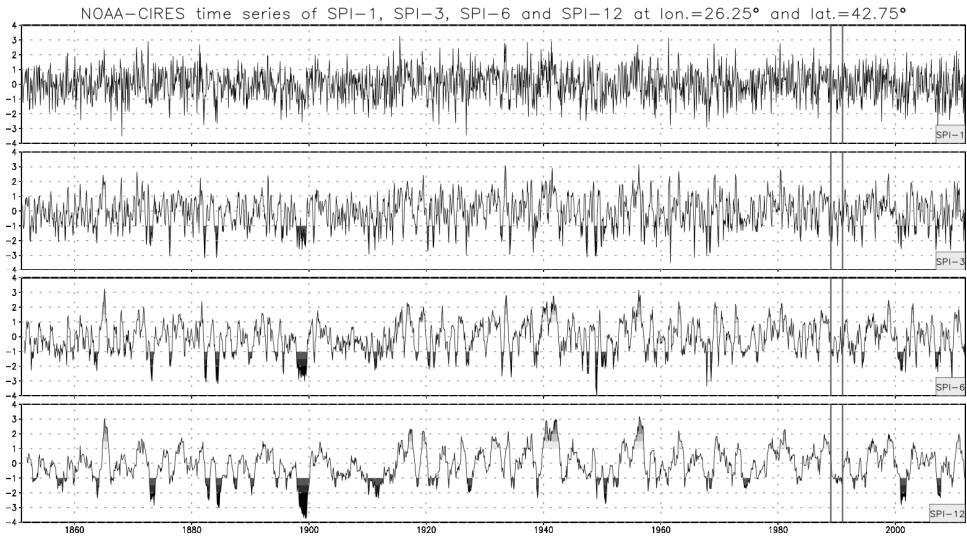


Fig. 5. Time series of SPI-1, SPI-3, SPI-6 and SPI-12 for grid point located in SE Bulgaria. The vertical grey lines brackets 1989-1991, which is drought period.

To save place, only the time series of the SPIs, of the data-set with the longest time-span, NOAA-CIRES are plotted. Such subsets can be also post-processed, especially applying techniques for trend analysis or for searching of periods of cyclic repetition of predefined anomalies.

Data-sets download

The output data-sets are written in the standard meteorological file format netCDF and are available for free of charge download at <ftp://xco.cfd.meteo.bg/SPI/>.

If you acquire these data, we ask that you acknowledge us in your use of the data. This may be done by including text such *the SPI data-set are prepared from Chervenkov et al. from the Bulgarian National Institute of Meteorology and Hydrology* in any documents or publications using these data. We would also appreciate receiving a copy of the relevant publications. Thank you in advance!

Summary and conclusion

Although many researchers argue that rainfall based DIs are not strong enough to define the wider drought conditions, their appropriateness was proven in numerous studies in most parts in the world. Despite their limitations, these indicators offer pragmatic approach for quantitative estimation of complex phenomena. This fact is strengthened since the rise of the digital era, when reliable data-sets of plenty of meteorological and hydrological parameters are freely available. This allows the calculation of such 'secondary' quantities as the SPI routinely for climatologically significant periods of time (in order of decades) practically all over the world.

Despite of the similarity in the precipitation sums for fixed time and location between the fourth input data-sets, they are generally not equivalent and, more or less, this reflects to the corresponding SPI-arrays. This specific have to be accounted in certain applications.

The presented data-sets and their availability a priori (i.e. before the start of any drought study) saves time and computational efforts of the potential user allowing him to focus his attention to the relevant analysis and interpretation. The data-sets can be used from wide circle of investigators and decision-makers solely or, as is our advice, in combination and/or addition with other methods achieving comprehensive drought assessment in every region of interest.

Acknowledgment. This study is entirely based on free available data and software. The authors wood like to express their deep gratitude to the organizations and institutes (University of Delaware, GPCC/DWD, ECMWF, NOAA, NCEP-NCAR, Unidata, MPI-M and all others), which provides free of charge software and data. Without their innovative data services and tools this study would be not possible. Thanks also to all third-party organizations for the funding: Support for the Twentieth Century Reanalysis Project version 2c dataset is provided by the U.S. Department of Energy, Office of Science Biological and Environmental Research (BER), and by the National Oceanic and Atmospheric Administration Climate Program Office. The authors are grateful to Dr. E. Dutra at ECMWF for the valuable suggestions.

References

- Compo, G.P., J.S. Whitaker, P.D. Sardeshmukh, N. Matsui, R.J. Allan, X. Yin, B.E. Gleason, R.S. Vose, G. Rutledge, P. Bessemoulin, S. Brönnimann, M. Brunet, R.I. Crouthamel, A.N. Grant, P.Y. Groisman, P.D. Jones, M. Kruk, A.C. Kruger, G.J. Marshall, M. Maugeri, H.Y. Mok, Ø. Nordli, T.F. Ross, R.M. Trigo, X.L. Wang, S.D. Woodruff, and S.J. Worley, (2011) The Twentieth Century Reanalysis Project. *Quarterly J. Roy. Meteorol. Soc.*, 137, 1-28. DOI: 10.1002/qj.776
- Hayes, M., Svoboda, M.D., Wilhite, D.A., Vanyarkho, O.V. (1999) Monitoring the 1996 drought using the standardized precipitation index. *Bulletin of the American Meteorological Society* 80: 429–438.
- Hayes, M., Svoboda, M., Wall, N., Widhalm, M., (2011) The Lincoln Declaration on Drought Indices: Universal Meteorological Drought Index Recommended. *Bull. Amer. Meteor. Soc.*, 92, 485–488, doi: <http://dx.doi.org/10.1175/2010BAMS3103.1>

- JRC, 2010: Climate of the Carpathian Region. Technical Specifications (Contract Notice OJEU 2010 /S 110-166082 dated 9 June 2010)
- Karavitis, C., Alexandris, S., Tsesmelis D., Athanasopoulos, G., Application of the Standardized Precipitation Index (SPI) in Greece, *Water* 2011, 3(3), 787-805; doi:10.3390/w3030787
- Lloyd-Hughes, B; Saunders, MA; (2002) A drought climatology for Europe. *INT J CLIMATOL* , 22 (13) 1571 - 1592. 10.1002/joc.846.
- McKee, TB., Doesken, NJ., Kliest, J. (1993) The relationship of drought frequency and duration to time scales. In Proceedings of the 8th Conference on Applied Climatology, 17–22 January, Anaheim, CA. American Meteorological Society: Boston, MA; 179–184.
- Peterson, T. C., R. S. Vose R. Schmoyer and V. Razuvayev (1998). Global Historical Climatology Network (GHCN) Quality Control of Monthly Temperature Data. *International Journal of Climatology*, 18, 1169-1179.
- Schneider, U., Becker, A., Finger, P., Meyer-Christoffer, A., Rudolf, B. Ziese, M. (2015) GPCP Full Data Reanalysis Version 7.0 at 0.5°: Monthly Land-Surface Precipitation from Rain-Gauges built on GTS-based and Historic Data. DOI: 10.5676/DWD_GPCP/FD_M_V7_050
- Stickler, A., S. Brönnimann, M. A. Valente, J. Bethke, A. Sterin, S. Jourdain, E. Roucaute, M. V. Vasquez, D. A. Reyes, R. Allan, and D. Dee, (2014) ERA-CLIM: Historical Surface and Upper-Air Data for Future Reanalyses. *Bull. Amer. Meteor. Soc.*, 95(9), 1419-1430 (DOI: 10.1175/BAMS-D-13-00147.1).
- Vicente-Serrano, SM., Beguería, S., Lorenzo-Lacruz, J., Camarero, JJ., López-Moreno, Ji., Azorin-Molina, C., Revuelto, J., Morán-Tejeda, E., Sanchez-Lorenzo, A., (2012) Performance of drought indices for ecological, agricultural, and hydrological applications. *Earth Interact.*, 16, 1–27. doi: <http://dx.doi.org/10.1175/2012EI000434.1>
- Wu, H., Svoboda, M. D., Hayes, M. J., Wilhite, D. A. and Wen, F. (2007), Appropriate application of the standardized precipitation index in arid locations and dry seasons. *Int. J. Climatol.*, 27: 65–79. doi:10.1002/joc.1371

Възможност за анализ на засушаване чрез набор данни в равномерна мрежа за стандартизираня валежен индекс

Хр. Червенков, Ив. Цоневски, К. Славов

Резюме: Използването на индекси за засушаване (ИЗ) е често прилаган метод за оценка на условията за засушаване. Като цяло, ИЗ са функция на различни хидро-метеорологични променливи и могат да бъдат интегрирани в комплексни системи за митигация на последствията. В световен мащаб се прилагат множество ИЗ, но Стандартизираният Валежен Индекс (SPI) има значителни преимущества пред останалите. SPI е избран от Световната метеорологична организация (СМО) като ключов индикатор за наблюдение на засушаването (вж. т. нар. «Декларация от Линкълн») и е един от двата най-често прилагани в Европа. Статията представя четирите получени от авторите глобални набори данни за SPI в равномерна мрежа. Те са изчислени съответно чрез UDEL/GEOG/CCR v3.02, GPCP/ v7.0, NOAA-CIRES

20CR v2c и ECMWF ERA20C бази данни за месечния валеж като всяка от тях е с времеви обхват повече от век. Индексът е изчислен за най-често използваните времеви мащаби от 1, 3, 6 и 12 месеца и, с изключение на ECMWF ERA20C, са в най-голямата резолюция, в която са налични данните за валежа. Популярността на SPI в експертната общност и силното убеждение на авторите, че свободния обмен на данни и програмни средства е основа за ползотворно научно сътрудничество, са главните мотиви за предоставянето на получените набори за свободен достъп. В конспективен стил е показана и приложимостта на резултатите за различни дългосрочни обективни изследвания в произволен географски район.

DATA AND ANALYSIS OF THE EVENTS RECORDED BY NOTSSI IN 2014

E.Botev, V.Protopopova, I.Aleksandrova, B.Babachkova, S.Velichkova, I.Popova, P.Raykova, M.Popova

Geophysical Institute, BAS, Akad. G. Bonchev, Str., bl.3, Sofia, Bulgaria, e-mail: ebotev@geophys.bas.bg

Abstract. A map of epicenters of 1602 earthquakes that occurred during 2014 in the Balkan Peninsula (sector outlined by latitude $\varphi = 37^{\circ} - 47^{\circ}\text{N}$ and longitude $\lambda = 19^{\circ} - 30^{\circ}\text{E}$) is presented. Expert generalized analysis of the seismicity over the territory of Bulgaria and its very adjacent lands (with more than 947 localized events) is proposed. Catalog of earthquakes with magnitude $M > 2.5$ is applied.

Key words: Balkan Peninsula, Bulgaria, seismicity

The present scientific communication contains generalized information on the results of collection, processing and analysis of the data about the seismic events recorded by the National Operative Telemetric System for Seismological Information (NOTSSI) in 2014. The expanded information about the realized seismicity is suggested as a natural generalization and supplementation of the monthly compilations of the preliminary seismological bulletin of NOTSSI. The analysis and evaluation of the space, time and energy distribution of the seismicity, periodically been made, open up possibilities for searching for time correlations with the parameters of different geophysical fields aiming to find out eventual precursor anomalies.

The recording and space localization of the seismic events in NOTSSI during 2014 is realized by means of the new digital network (Solakov et al., 2006). The routine processing and acquisition of the initial data is organized in a real time duty regime. The operations are fulfilled by the authors of this communication. In such a way the main goal of NOTSSI, namely the seismicity monitoring in order to help the authorities' and social reaction in case of earthquakes felt on the territory of the country, is realized. The computing procedure for determining the parameters of the seismic events is an adaptation of the widespread product HYPO71 (Solakov, 1993). The energy parameters of the events are presented mainly by the magnitude M calculated according to the records duration by the formula (Christoskov and Samardjieva, 1983).

$$M = 1.92 + 2.72 \log \tau - 0.026 \Delta$$

After bringing into use the new digital broadband seismometers of NOTSSI network, the magnitude determination for local and regional events is calculated by P wave amplitude ratio (Christoskov et al., 2011a, b).

The focal mechanism parameters are obtained by means of a program FOCMEC (Snoke, 2009). The high sensitivity of the seismographs allows recording and processing of a great number of long distance earthquakes. As a result of the achieved experience in the authors' interpretation work, different magnitude's lower threshold for successful determination of local, regional and long distance earthquakes is established: $M=1.5$ for the territory of Bulgaria, $M=3.0$ for the central part of the Balkans, $M=5.0$ for long distance events. The precision of the epicenter's determination is different; except on the distance it depends also on the specific position of the epicenter in relation to the recording network. The parameters of seismic events occurring at a distance more than 100-150 km outside the territory of Bulgaria should be accepted only informatively and cannot be used for responsible seismotectonic investigation.

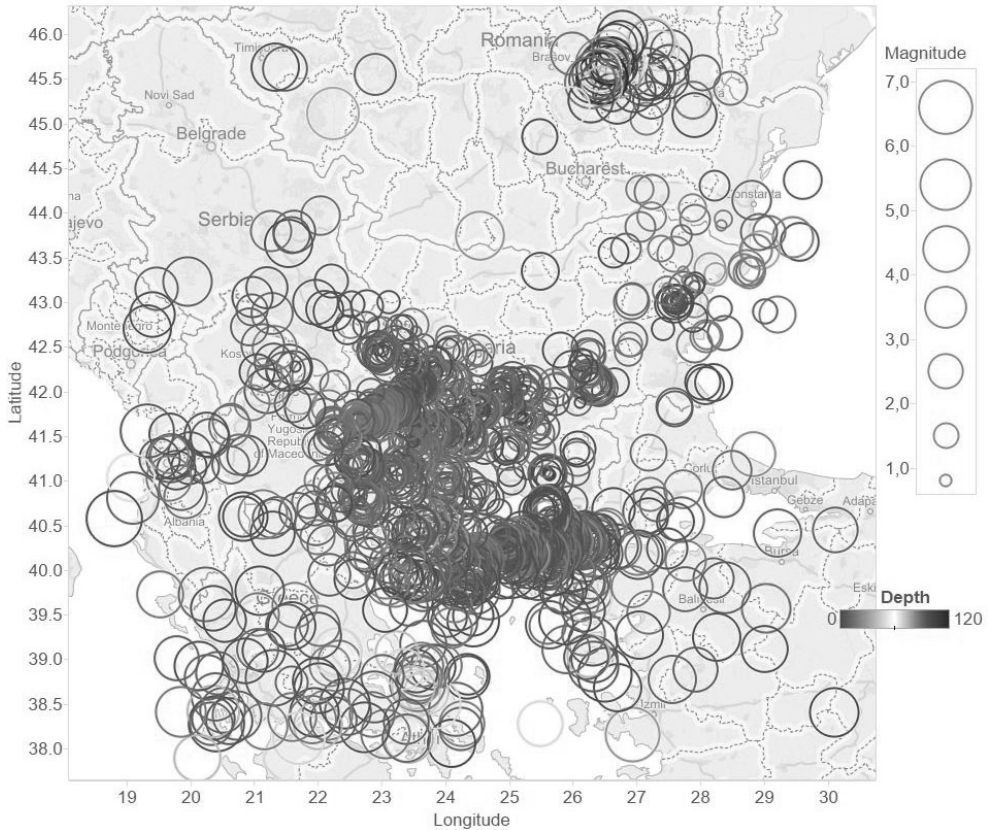


Fig.1. Map of epicenters in Central Balkans during 2014 (Open Street Map - Tableau Desktop 9.2.)

For the period of observations presented in this communication, the primary data about 2000 local, regional, distant earthquakes and industrial explosions on the territory of Bulgaria are recorded, classified and processed (as a work bulletin) in NOTSSI. After comprehensive analysis of the records and application of the above mentioned calculation procedures it is established that 1602 of all registered earthquakes are in the Balkan Peninsula region outlined by geographic latitude 37° - 47° N and longitude 19° - 30° E. The epicenters of the earthquakes differentiated by magnitude levels are plotted on Fig.1. The number of the events in the magnitude interval $M=0.5-1.9$ is 657, in $M=2-2.9$ - 630, in $M=3-3.9$ - 237, in $M=4-4.9$ - 66, in $M=5-5.9$ - 11 earthquakes. During this not so active period there is 1 event with magnitude $M=6.6$. All earthquakes with magnitude more than 4 are out of Bulgarian borders.

As a whole, the seismic situation in the studied part of the Balkans during 2014 is characterized as not so high activity - 1602 events, similar with previous year (2013) - 1622 events, against 1508 in 2012, 1829 in 2011, 2401 in 2010, 2744 in 2009, 1775 in 2008, and around 1100- 1400 for most of the previous years. The maximum realized earthquake is with magnitude $M_s=6.6$ in North Aegean sea, while this value for the previous years is lower than five, as a rule, except 2011 - $M=5.8$ and 2012 - $M=5.6$. It can be noted that the observed tendency of relatively high activity is partly due to the high level of earthquake activation in North Aegean sea, Romania, Central Greece, Serbia, and also due to increase of number of microearthquakes in the territory of Bulgaria.

The strongest event outside Bulgaria during the study period occurred in the region situated to the south of North Aegean Sea (Greece) with magnitude $M=6.6$. This event caused VI - VII degree of MSC scale on 24 May in Kardzhaly region and Haskovo town. Shakable effects because of outside attack (earthquake with magnitude $M=5.6$ in Vrancea source zone in Romania) during the study period occurred in north-eastern Bulgaria - intensity IV-V degree of MSC in town of Silistra on 22 November 2014.

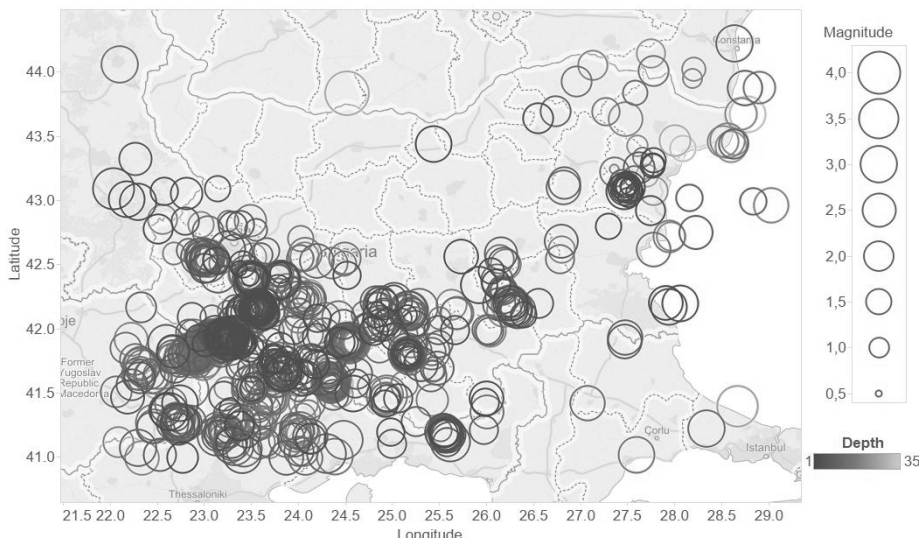


Fig.2. Map of epicenters in Bulgaria and adjacent lands during 2014 (Open Street Map - Tableau Desktop 9.2.)

As a whole, events with $M < 3.0$ which occur outside Bulgaria are difficult to be localized by the national seismological system; consequently, not all of them have been marked on the scheme in Fig.1.

Fig.2 illustrates the seismicity just in the territory of Bulgaria and nearby lands ($\varphi = 41^{\circ} - 44.3^{\circ}\text{N}$, $\lambda = 22^{\circ} - 29^{\circ}\text{E}$). The earthquakes are differentiated by magnitude intervals. The parameters of relatively stronger earthquakes are presented in Table 1.

Table 1. List of earthquakes with $M \geq 2.5$ in Bulgaria and adjacent lands during 2014

Date	Time	Latitude [N°]	Longitude [E°]	Depth [km]	Local magnitude
3.1.2014	11:33:33.6	41.28	22.74	5	3.2
5.1.2014	4:51:18.1	41.63	23.76	12	2.6
10.1.2014	7:22:21.5	41.64	24.00	20	2.7
12.1.2014	0:29:15.2	41.83	22.89	8	2.5
13.1.2014	3:34:17.2	41.55	22.86	15	2.6
14.1.2014	12: 5:48.5	41.92	24.54	18	3.2
14.1.2014	15:44: 1.5	41.91	24.53	17	3.1
16.1.2014	2: 1:10.1	42.22	26.24	20	3.0
19.1.2014	4:51:18.1	41.63	23.76	12	2.6
29.1.2014	10:40:17.1	41.93	24.55	18	2.7
29.1.2014	4:31: 4.7	41.92	24.52	12	2.5
29.1.2014	5: 5:10.8	41.92	24.54	20	3.4
29.1.2014	7:39:47.2	42.42	23.81	20	2.5
30.1.2014	7:39:47.3	42.42	23.81	18	2.5
30.1.2014	9:23:38.9	42.41	23.81	11	2.9
30.1.2014	9:32:29.4	42.41	23.81	3	2.8
2.2.2014	22:47:23.2	41.93	24.49	8	2.8
5.2.2014	1:56:44.4	41.42	28.64	26	3.4
5.2.2014	3:54:17.3	42.17	23.58	10	2.8
9.2.2014	22:31:11.0	41.92	24.53	20	2.7
17.2.2014	17:49:41.1	41.03	27.57	17	2.6
17.2.2014	21:55: 4.5	41.69	23.82	6	2.6
17.2.2014	9:26:30.2	41.68	23.84	2	2.5
18.2.2014	20:30:59.5	42.07	24.86	7	2.6
20.2.2014	15:12: 0.0	41.69	23.83	2	3.3
23.2.2014	16: 9:45.6	41.52	24.58	2	2.5
28.2.2014	15:35:14.5	41.14	25.60	8	3.2
28.2.2014	18:48:54.7	41.19	25.54	8	2.5
1.3.2014	20:24: 6.6	41.21	25.53	11	2.7
4.3.2014	0:49:11.7	42.41	23.82	9	2.9
6.3.2014	19:19:33.2	41.67	23.83	11	2.5
11.3.2014	18:50:48.1	43.12	22.04	4	3.5

Date	Time	Latitude [N°]	Longitude [E°]	Depth [km]	Local magnitude
13.3.2014	6:16:45.9	41.19	25.57	5	2.6
15.3.2014	13:44:27.9	42.59	22.95	8	2.7
16.3.2014	23:44:36.9	41.15	24.47	12	3.0
20.3.2014	23:47:46.6	41.64	24.05	2	2.6
22.3.2014	15:21:16.0	41.93	23.24	2	2.8
27.3.2014	18:20:12.7	41.24	28.31	13	2.7
28.3.2014	4:41:44.8	42.16	23.58	8	3.2
1.4.2014	16: 6:13.6	41.78	23.78	16	2.5
5.4.2014	3:36:47.9	41.82	22.83	11	3.1
14.4.2014	7:44: 4.7	41.29	22.47	17	2.5
15.4.2014	12:27:48.6	42.65	23.24	7	2.5
17.4.2014	15:58:55.0	42.21	23.57	5	2.6
19.4.2014	16: 2:50.9	42.17	25.15	8	3.1
19.4.2014	23:39:51.1	42.18	25.17	15	2.8
23.4.2014	23:26: 8.5	42.17	23.57	9	2.5
24.4.2014	1: 7:29.9	42.42	23.49	14	2.5
30.4.2014	12:18: 1.7	42.17	26.31	9	2.5
3.5.2014	1:55:55.9	42.42	23.49	14	2.5
6.5.2014	1:54:22.5	42.54	23.04	11	2.9
6.5.2014	6: 2:22.7	44.23	28.61	10	2.7
14.5.2014	12:20:45.8	43.69	28.75	33	2.6
22.5.2014	8:24:50.9	42.23	28.03	4	2.5
22.5.2014	8:24:50.9	42.23	28.03	4	2.5
24.5.2014	9:32:40.5	42.46	23.15	8	2.8
26.5.2014	20:39:12.5	41.50	24.93	17	3.4
7.6.2014	7:58:59.3	41.44	22.74	3	2.6
20.6.2014	5:19:11.9	42.17	23.56	20	2.5
24.6.2014	19:39:53.3	43.85	24.51	28	4.0
25.6.2014	19:17:47.6	42.37	25.91	2	2.7
8.7.2014	17: 4:27.9	41.18	23.13	9	3.0
11.7.2014	7:45: 9.8	42.20	27.91	4	2.5
16.7.2014	22:45:13.3	41.60	24.33	15	2.8
30.7.2014	13:11:52.1	41.60	24.35	13	2.6
30.7.2014	13:59:25.5	41.59	24.35	14	2.6
2.8.2014	3:57: 5.6	41.60	24.34	16	2.8
5.8.2014	17:59:45.5	41.02	24.38	17	2.6
7.8.2014	16:34:15.5	43.10	27.44	2	2.6
16.8.2014	22:42:54.1	42.25	24.08	13	2.8
20.8.2014	1:29:30.4	41.61	24.34	14	2.8
21.8.2014	4:28:15.9	41.68	24.23	6	3.9
22.8.2014	7:16:21.1	42.15	23.42	10	2.7

Date	Time	Latitude [N°]	Longitude [E°]	Depth [km]	Local magnitude
23.8.2014	5:11: 1.0	41.94	23.05	13	2.5
1.9.2014	7:46:48.8	41.79	23.00	20	2.5
2.9.2014	2:37:16.0	42.25	25.01	9	2.5
2.9.2014	4:54:24.5	42.58	23.05	20	2.8
8.9.2014	3:41:10.3	41.85	22.85	13	2.5
13.9.2014	14: 3:20.9	41.59	23.48	14	2.7
13.9.2014	14: 4:25.8	41.60	23.49	13	2.7
17.9.2014	9:25: 4.9	41.85	25.41	13	2.5
23.9.2014	19: 3: 3.4	41.13	23.30	13	2.5
25.9.2014	22:13: 5.1	43.04	22.18	2	2.5
25.9.2014	22:49:15.5	43.02	22.30	3	2.7
26.9.2014	3:52:56.6	43.46	25.43	2	2.5
1.10.2014	9:47:54.8	41.10	23.32	10	3.0
5.10.2014	9:45: 2.3	41.04	24.29	8	3.1
10.10.2014	20:21:39.5	42.20	25.27	13	2.8
13.10.2014	19:58:32.6	41.23	24.01	13	2.7
15.10.2014	20:27:37.9	44.07	22.11	15	2.7
25.10.2014	20: 6: 7.7	41.08	23.42	11	2.5
5.11.2014	1:58:21.3	41.97	23.21	12	2.6
5.11.2014	11: 0:43.6	41.84	25.15	11	3.0
5.11.2014	19:19:31.5	41.74	22.34	18	2.5
5.11.2014	3:40:48.2	41.98	23.24	5	2.5
7.11.2014	7: 1:40.9	42.59	22.99	13	2.8
7.11.2014	7:42: 8.8	41.04	23.40	6	3.0
11.11.2014	13:16:22.9	41.38	22.63	1	2.8
20.11.2014	11:50: 8.5	41.98	23.23	2	2.6
20.11.2014	12:13:24.7	41.96	23.17	14	3.2
21.11.2014	8:30:32.2	41.97	23.23	5	2.6
28.11.2014	11:23:47.1	41.28	22.78	9	2.7
5.12.2014	1:17:20.8	41.92	22.60	8	2.6
12.12.2014	17:33:29.1	41.09	22.30	10	2.7
12.12.2014	19:59:20.6	41.16	23.87	15	2.5

On the territory of Bulgaria relatively normal activity of earthquakes is observed during 2014 – 947 events are observed, against 1124 in 2013, 932 in 2012, 1205 in 2011, 1607 in 2010, 2017 in 2009 and 1079 in 2008. The earthquakes of a magnitude higher than 3.0 are in normal amount – 22 events compared with an averaged number of about 20-35 for most of the all previous years (exception is 2009 with 147 events because of the aftershocks of Valandovo M=5.2 earthquake).

The maximum realized magnitude on Bulgarian territory is Ms=3.9 (in the region of West Rhodopes), which is not the highest earthquake, in comparison with the maximum

magnitude in the course of previous years. The strongest event (with magnitude $M=4.0$) occurs on 24th of June 2014, close to Bulgarian border (on Romanian territory) and caused macroseismic effects with intensity of IV degree of MSC scale in the town of Belene.

As usual, the largest concentration of the epicenters in the other regions of Bulgarian territory during 2014 is marked in the southwestern part of the investigated region (presented in Fig.2). The Kroupnik seismic source is known with the strongest crustal earthquakes in Europe ($M=7.8, 7.1$) for the last 160 years. In 2014 only 3 events of $M \geq 3.0$ occurred in this region. The strongest felt earthquake for the south-western part of Bulgarian territory is with magnitude $M=3.3$, it is felt on 20th of February in Gotse Delchev region (western slopes of Rhodope mountain) by intensity of III - IV degree of MSC scale.

The other Bulgarian seismic sources in 2014 are relatively not so active than during the previous years. They produced not more than 15 earthquakes affecting different localities in this country by intensity of up to III - IV degrees of MSC scale. The maximum number of felt earthquakes is occurred around the Monastery uplift. Two cases of magnitudes about 3.0 aroused shocks of intensity up to IV degrees of MSC scale are felt in Monastery Highland territories. A relatively not so significant seismic impact is associated with the Pernik earthquake source zone in the central parts of West Bulgaria.

Strike 130 Dip 85 Slip -2

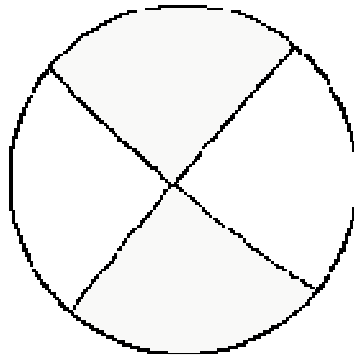


Fig.3. Focal plane solution of earthquake close to the Bulgarian NPP Kozloduy (24.06.2014, 19:39 GMT, $M=4.0$, $H=28$ km)

For the determination of the earthquake mechanism the program FOCMEC is used. Input data are the polarities of the P wave. Twenty five first motion polarities data from seismological stations in Bulgaria and surrounding area, taken from NOTSSI and Orfeus database (<ftp://www.orfeus-eu.org/pub/data/continuous/2014/>) are included in the double - couple focal mechanism - Fig.3. The solution is displayed on lower hemisphere. The polarities from Orfeus are checked as waveform. The strike, dip and rake are determined in accuracy up to 5 degree. The earthquake is characterized as a strike-slip faulting, with very small dip-slip component. The fault plane solutions of the some other events are with very bad quality because of a low number of polarities.

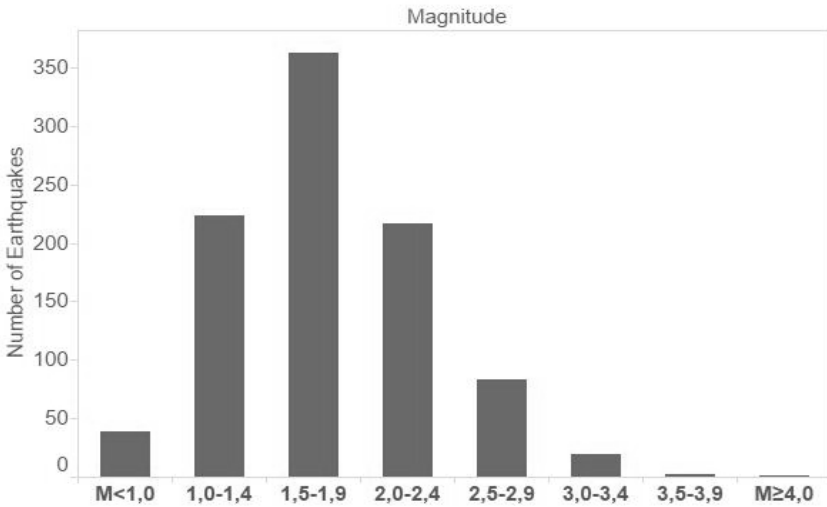


Fig.4. Magnitude - frequency distribution of the earthquakes

A detailed analysis of seismicity in the individual seismic zones is hard to be fulfilled because of the insufficient quantity of events and the narrow magnitude range of the earthquakes. The joint statistics of all the events in Fig.2 characterize predominantly the seismicity parameters of the southwestern part of the territory under investigation.

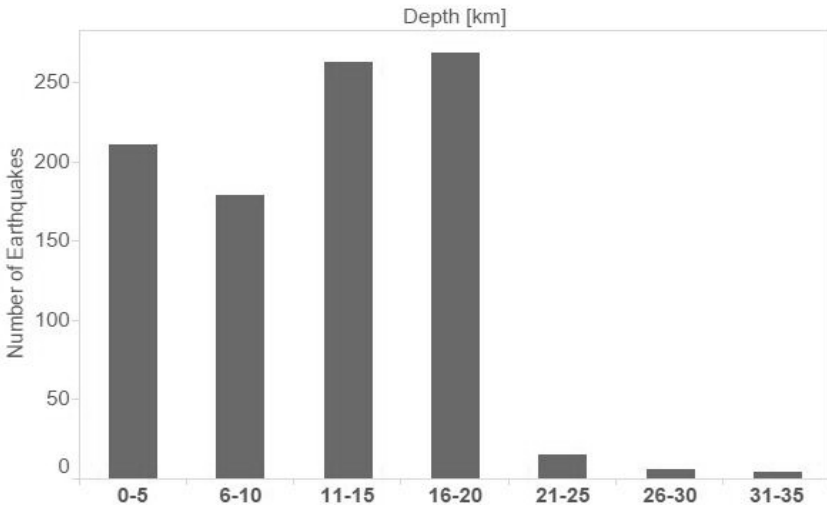


Fig.5. Depth - frequency distribution of the earthquakes

The magnitude-frequency distribution for the entire data set is presented in Fig.4. The number of localized events increases with the magnitude decreasing: for $M=4.0$ is 1 event, $M=3.5-3.9$ is 2 events, for $M=3.0-3.4$ is 19 events, for $M=2.5-2.9$ - 83, for $M=2.0-2.4$ - 217 and so on. The abrupt diminishing of the number of earthquakes in the first two intervals ($M < 1.5$) in Fig.4 determines also the registration power of the seismic stations network. Taking the latter into account, it can be supposed that the magnitude sample for

levels with $M > 1.5$ is comparatively closer to the reality for the bigger part of the Bulgarian territory.

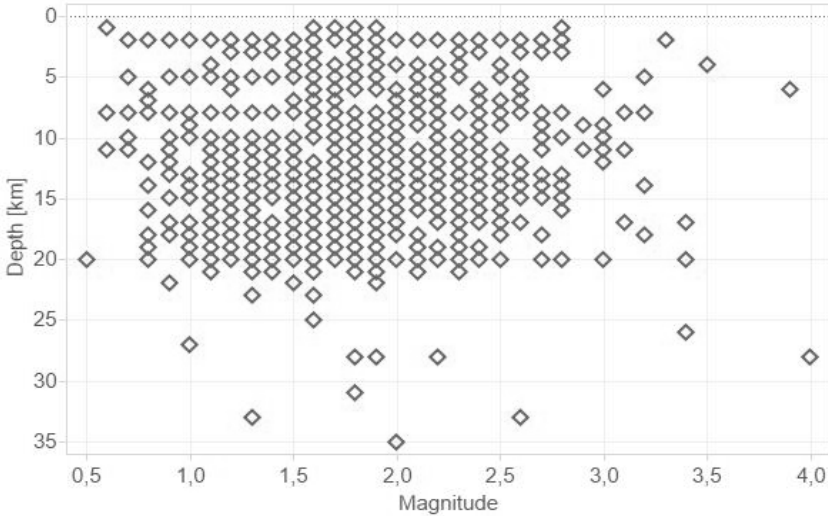


Fig.6. Magnitude - depth dependence

The picture of the depth distribution in Fig.5 shows that the majority of events occur in range 11-20 km depth. The number of events does not decrease smoothly with increase of the depth. It is possible the established predominating depth (from 11 to 20 km) to be also due to the presence of small number of unidentified industrial explosions. In the same time the number of events in the interval 11-15 km is bigger. The magnitude distribution of the events in depth (Fig.6) permits to note some differentiation of depth "floors" with the increase of magnitude - the maximums can be traced out for the depth interval from 4 to 28 km. It is remarkable that the strongest events are relatively uniformly deep situated.

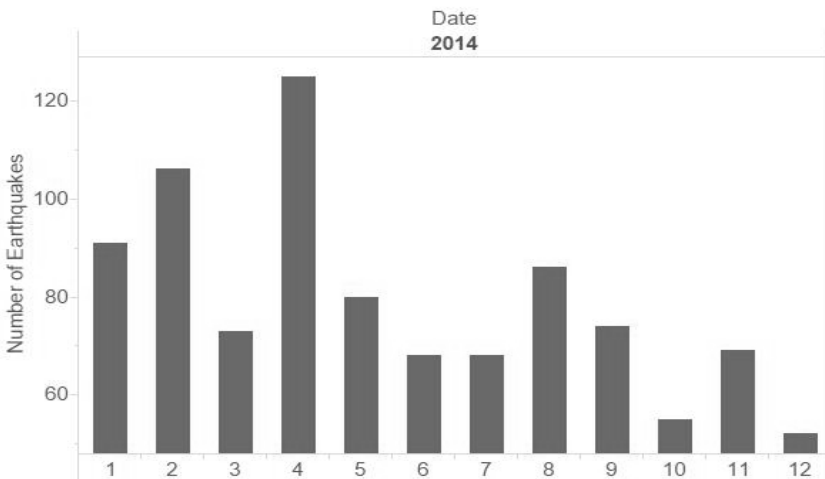


Fig.7. Time distribution of the earthquakes.

Fig.7 illustrates the distribution of seismicity in time according to the number of events per months. The biggest earthquake's amount is displayed in April, when more than 120 earthquakes occurred, and it is associated with seismic activity in Central Bulgaria – Monastery Uplifts region and Parvomay town region. The lowest earthquake quantity is in October and December, less than 30 events per month. The maximum energy release during the period May - August does not corresponded to the maximum number of events during the first half of the year.

Additionally, about 1100 distant earthquakes have been recorded in the period under study, as well as more than 900 industrial explosions, processed and classified in the preliminary monthly bulletins. In order to identify the artificial seismic sources the methodical approach described by Deneva et al. (1988) and some information about the quarry sites in Bulgaria have been used.

Acknowledgements: The authors owe their gratitude to the engineering staff for the perfect software and hardware ensuring of NOTSSI and to Team Vision Bulgaria Ltd. for the kind grant of the Tableau Desktop software.

References

- Barrier, E., N.Chamot-Rooke, G.Giordano, 2004. Geodynamic map of the Mediterranean, Sheet 1- Tectonics and Kinematics, CGMW, France.
- Christoskov L. and E. Grigorova, 1968. Energetic and space characteristics of the destructive earthquakes in Bulgaria since 1900. *Izv.BAS*, vol XII .
- Christoskov L. and E. Samardjieva, 1983. Investigation on the duration of the seismic signals like a energetic characteristic of the earthquakes. *BGJ*, vol.IX, N1.
- Christoskov L. et al., 1987. Real time and background data processing in the Bulgarian seismological network. *Proc. Xx gen. Assembly 1986*, Kiel. , Zurich.
- Christoskov L., L. Dimitrova, D. Solakov, 2011a. Magnitude determinations of P wave by digital broadband seismometers of NOTSSI network for local and regional events. *Comptes rendus de l'Academie bulgare des Sciences*, Vol 65, No5, pp.653-660
- Christoskov L., L. Dimitrova, D. Solakov, 2011b. Digital broadband seismometers of NOTSSI for practical magnitude determinations of P waves. *BGS. v.XXXVIII, N1-4/2011, ISSN 1311-753X*, 62-72.
- Deneva D. et al., 1988. On the discrimination between industrial explosions and weak earthquakes using records of local seismics networks. *Proc. of conference in Liblice, 1988, Praha*.
- Georgiev, I. D.Dimitrov, T.Belijashki, L.Pashova, S.Shanov, G.Nikolov, 2007. Geodetic constraints on kinematics of southwestern Bulgaria from GPS and leveling data, *Geological Society, London, Special Publications*, 2007; 291: 143-157.
- Snoke J.A, 2009. FOCMEC: FOCal MECanism Determinations. VirginiaTech, Blacksburg, VA, USA, 2009, Manual.
- Solakov, D., 1993. An algorithm for hypocenter determination of near earthquakes. *Bulg. Geophys. J.* 19 (1), 56-69
- Solakov, D. et all., 2006. National Seismological Network – state and development. *Proceedings of Scientific-practical conference on management in extraordinary situations and people protection, BAS, Sofia, 2005*, 265-272.

Данни и анализ на сеизмичните събития регистрирани от НОТССИ през 2014

Е.Ботев, В.Протопопова, И.Александрова, Бл.Бабачкова, С.Величкова, И.Попова,
Пл.Райкова, М.Попова

Резюме. Предлаганото научно съобщение съдържа обобщена информация за резултатите от събирането, обработката и анализа на първичните данни за сеизмичните събития, регистрирани от Националната Оперативна Телеметрична Система за Сеизмологична Информация (НОТССИ) през 2014 г. Представена е карта на епицентрите на общо 1602 земетресения в частта от Балканския полуостров, ограничена от географска ширина 37° - 47° N и дължина 19° - 30° E. По-подробно се анализира сеизмичността за територията на България и прилежащите ѝ земи (повече от 947 сеизмични събития в район с координати $\lambda = 22^{\circ}$ - 29° E и $\varphi = 41^{\circ}$ - 44.3° N). Предлага се и каталог на земетресенията с магнитуд $M > 2,5$. Сеизмогенните прояви се обсъждат по зони, сравнени със съседни периоди време.



IN MEMORIAM

CORESPONDING MEMBER OF BAS DIMITER LUBENOV YORDANOV (31.10.1933 – 26.04.2015)

Dimiter Lubenov Yordanov is born on October 31 1933 in Sofia. In 1956 he graduates from the Faculty of Physics of the “St. Kliment Ohridski” University of Sofia. In years 1956-1960 he works as a research specialist in the Aerology department of the National Hydro-meteorological Service. From 1960 to 1964 he is a research fellow in the Department of Atmospheric Physics of the Geophysical Institute of the Bulgarian Academy of Sciences. In 1968 Dimiter Yordanov defended his thesis “Turbulent diffusion in the atmospheric surface layer” and became Doctor of Sciences. Since 1990 D. Yordanov is a professor at the Geophysical Institute of the Bulgarian Academy of Sciences. In the period 1995–2004 he was the Head of the Department of Atmospheric Physics. In 2004 Dimiter Yordanov was elected corresponding member of the Bulgarian Academy of Sciences.

The range of the scientific interests of Dimiter Yordanov is broad. His work in geophysical hydrodynamics, atmospheric boundary layer physics, pollution transport modeling and air quality studies has sound contribution to these fields of knowledge and is recognized world wide. He is an author of more than 250 scientific papers, co-author of 4 books and 1 textbook. His publications are always original and of very high professional level.

The teaching activity of D. Yordanov is also impressive. He had been a lecturer at the Faculty of Physics of the “St. Kliment Ohridski” University of Sofia, The Technical University of Darmstadt and the Humboldt University in Berlin. He had been a supervisor of more than 20 Master and 6 PhD studies.

Dimiter Yordanov was the pioneer who set the fundamentals of the theoretical studies of the atmospheric boundary layer and the atmospheric composition modeling in Bulgaria. He gave the direction and led the professional career of many younger scientists,

including 1 corresponding member of the Bulgarian Academy of Sciences, 2 professors, several Doctors of Sciences and PhDs, 4 associated professors.

Dimiter Yordanov passed away on April 26 2015. With this the National Institute of Geophysics Geodesy and Geography of the Bulgarian Academy of Sciences lost one of his most respected scientists and the world atmospheric studying community lost a really outstanding researcher.



IN MEMORIAM

ACADEMICIAN STOYCHO PANCHEV VALCHEV

(06.03.1933 - 30.08.2014)

Academician Stoycho Panchev was born in 1933 in the village Lisets, Lovech. He graduated from Sofia University, Faculty of Physics and Mathematics, specialty physics, meteorology specialization in 1956. In 1959 he defended his PhD thesis and was appointed as an assistant at the Department of Meteorology and Geophysics. In 1963 he was appointed as an associate professor, from 1965 is a doctor of physical and mathematical sciences, from 1970 - professor, 1984 - corresponding member of the Bulgarian Academy of Sciences, 1997 - academician. During the periods 1974 to 1994 he was Head of the Department, 1979-1983 years - Dean of the Faculty of Physics, 1988-1991 years - Vice Chairman of the Bulgarian Academy of Sciences, 1994-1997 years - Vice Chairman of the Higher Attestation Commission. After his retirement from the University, he worked at the Institute of Solar-Terrestrial Influences of Bulgarian Academy of Sciences (2002-2008).

Acad. Panchev is one of the most famous Bulgarian scientists in the field of meteorology. The scientific work of acad. Panchev was focused in the following scientific fields: physics and dynamics of clouds and precipitation; semi empirical and statistical theory of turbulence; atmospheric macroturbulence; dynamic of the equatorial atmosphere and the wave motions; chaos theory; non-linear dynamic of natural and social phenomena; history of physics and so on. He is an author of above 150 scientific papers and 10 books and textbooks in Bulgarian and other languages: "Random Functions and Turbulence" (1965, 1967, 1971, 1976), "Dynamic meteorology" (1981, 1985), "Theory of chaos" (1996), "Fundamentals of atmospheric physics" (2003). He is a co-author of the textbook "General Meteorology" (1978) and the books "Population dynamics and national security" (2005) and "Social dynamics without formulas" (2008). He led dozens of graduate students

and 15 PhD students with completed dissertations.

The proof of high appreciation of the scientific achievements of acad. Panchev is his memberships at the Royal Meteorological Society of United Kingdom, the American Meteorological Society, the International Association of Mathematical Physics, and his participation in editorial staffs of our and foreigner journals. Acad. Panchev is a laureate of the “Dimitrov Prize” for science (1972), medal “St. Kliment Ohridski” of blue ribbon for contributions to the Sofia University (2002), medal “Marin Drinov on ribbon” for contributions to the Bulgarian Academy of Sciences (2003).

With the death of academician Stoycho Panchev, Sofia University “St. Kliment Ohridski” and the scientific community lost a most respected lecturer and outstanding researcher.



100 YEARS SINCE THE BIRTH OF PROF. IVAN-ASSEN PETKOV

Prof. Ivan-Asen Petkov (1915 – 2005) is one of the founders of the geophysics in Bulgaria. His contributions cover almost all topics in geophysics – gravimetry, seismic prospection, seismology, geothermal research, geomagnetism, geotectonics, geomorphology, seismic engineering, geoelectricity and geolithology. Geoscientists face the same challenges: indirect observations, unique events, restricted experiments and intuition. Significant part of the scientific knowledge on the structure of the Earth's crust on the Bulgarian territory is gained by the pioneering studies of Prof. Petkov. In 1938 he graduated in "Physics" and "Mathematics" at Sofia University. His scientific career started in 1941 at the State Institute of Geography, where he performed his first gravimetric measurements together with Vl. Hristov. In 1946 he moved at the Direction for geologic prospection. Afterwards, in 1947 – 1948 I. Petkov went to the former USSR for a specialization. At the end of 1948 he led the first regional geomagnetic and gravimetric investigations, and at 1949 he started the first seismic prospection in Bulgaria. As a lecturer at Sofia University, I. Petkov gave his first lectures in gravimetry and seismometry in 1953 – 1954 and in 1957 he launched the first course in General Geophysics. The latter became a two-semester course in 1964. I. Petkov made the first measurement of the absolute value of the gravity field in Bulgaria. In 1961 he got his habilitation and became an Associate Professor at Sofia University, founded section "Geophysics" at the Dept. "Meteorology and Geophysics". During the same year he was appointed as a senior researcher at the Geological Institute of the Bulgarian Academy of Sciences, where he founded section "Geophysics"- the first research unit in applied geophysics in Bulgaria. In 1968 I. Petkov became Full Professor at Sofia University. He did a number of theoretical studies on the seismic wave propagation in non-homogeneous media. For the first time he determined the depth to Mohorovicic boundary using gravimetric data and applied the methodology of deep seismic sounding for revealing the structure of Earth's crust. Prof. Petkov studied the seismicity of Bulgaria in relation to anti-seismic construction and seismic micro division. He is a co-author of the first gravimetric, geomagnetic, tectonic, geothermal and seismic

forecast maps of Bulgaria. He also published a number of scientific publications, textbooks and monographs.

Prof. Petkov lived and worked during the times of monarchy, socialism and capitalism, but this did not decline him from science and did not change his character. He stayed moderate, calm and delicate, withstanding the talk of the town and following his aims in geophysics.

Information for Contributors

Submission of a paper implies that it has not been published previously and is not under consideration for publication elsewhere.

Typescript. All parts of the paper must be typed double-spaced on good quality white paper A4 (210 x 297mm) with at least 2.5 cm margins at top, bottom, and sides. Each page of the typescript should be numbered on the bottom in the right corner.

Authors are expected to supply 2 clean copies in English or Bulgarian. Please use correct English or Bulgarian spelling, punctuation, grammar, and syntax. The metric system must be used throughout; use of appropriate SI units is encouraged.

Paper length. Paper should be written in the most concise form. Occasionally long papers (over 15p.) are accepted, particularly those of a review nature.

The typescript should be arranged as follows:

1. Title page including authors' names and affiliations
2. Abstract and key words
3. Text (including tables and figures)
4. Reference list

Abstract. The abstract should be in a single paragraph (250 words or fewer). State the nature of the investigation and summarize its important conclusions. References must not be cited in the abstract. The abstract should be suitable for separate publication in a Web site.

Mathematics. All characters available on a standard typewriter must be typewritten in the equations as well as in text. Special attention should be paid to single couples of the kind: vv, pp, μ , η . Distinction should be made between the letter O and the numeral 0; between the letter I and the numeral 1; between k and kappa.

Alignment of symbols must be unambiguous. Superscripts and subscripts should clearly be in superior or inferior position. Fraction bars should extend under the entire numerator. Displayed equations should be numbered consecutively throughout the paper; the number (in parentheses) should be to the right of the equation.

References. A complete and accurate reference list is of major importance. Only works cited in the text should be included in the reference list. References are cited in the text by the last name of the author and the year: (Jones, 1990). If the author's name is part of the sentence, only the year is bracketed. References are arranged alphabetically by the last names of authors. Multiple entries for a single author are arranged chronologically. Two or more publications by the same author in the same year are distinguished by a, b, c after the year.

Tables. Tables should be typed as authors expect them to look in print. Every table must have a title. Column headings must be arranged so that their relation to the data is clear. Each table must be cited in the text.

Illustrations. All illustrations should be inserted in the text, suitable for the camera-ready reproduction (which may include reduction). Each figure must be cited in numerical order in text and must have figure legend. Please do not draw with hairlines. The minimum line width is 0.2 mm (i.e. 0.567pt).

Electronic submission. Authors must submit an electronic copy of their paper with the final version of the manuscript. The electronic copy should match the hardcopy exactly.

Authors will receive more detailed information when the article is accepted for publication so that requirements for the camera-ready presentation are fulfilled.